2016

A Study of Crystallization Behavior in Phase Separated Chalcogenide Glasses

Andrew Buff
University of Central Florida

A STUDY OF CRYSTALLIZATION BEHAVIOR IN PHASE SEPARATED CHALCOGENIDE GLASSES

by

ANDREW K. BUFF
B.S. Clemson University, 2013

A thesis submitted in partial fulfillment of the requirements
for the degree of Master of Science
in the Department of Materials Science and Engineering
in the College of Engineering and Computer Science
at the University of Central Florida
Orlando, Florida

Summer Term
2016

Major Professor: Kathleen Richardson

ABSTRACT

Chalcogenide glasses (ChG) are known for their wide transmission ranges in the infrared and for their high refractive indices. However, applications for ChG are often limited by their poor thermal/mechanical properties. Precipitating a secondary crystalline phase in the glass matrix can improve these properties, but too much crystallization and/or large or multiple phase crystallites can lead to a loss in infrared (IR) transmission. Controlled crystallization can be used to tune the properties of these glasses. This work examines the crystallization behavior in phase separated chalcogenide glasses in the $GeSe_2$-As_2Se_3-PbSe glass system.

Specifically, the research presented in this thesis work has investigated the crystallization behavior in the $20GeSe_2$-$60As_2Se_3$-20PbSe (20 PbSe) and $15GeSe_2$-$45As_2Se_3$-40PbSe (40 PbSe) glasses for an IR optical system operating in the 3 to 5 μm range. While both of these glasses were found to have droplet-matrix phase separation, the morphology differed from each other in two key ways. First, the droplets seen in the 20 PbSe glass (100-130 nm) are roughly twice as big as those in the 40 PbSe glass (35-45 nm). The droplet sizes seen in the base glass directly affect the short wavelength cutoff of the two glasses where the 20 PbSe glass (1.993 μm) has a longer wavelength cutoff than the 40 PbSe (1.319 μm). Secondly, the 20 PbSe glass has Pb-rich droplets and the 40 PbSe glass has a Pb-rich matrix, impacting where the initial stages of crystallization are initiated. Crystallization occurs in the Pb-rich phase and affects the glass-ceramic properties differently depending on whether the Pb-rich phase is the minority phase (20 PbSe) or the majority phase (40 PbSe). When the crystallization occurs in the majority phase, it greatly affects the hardness, density, and refractive index. When the crystallization occurs in the minority phase, the hardness

and density change negligibly while the refractive index still shows significant change. While both glasses show an effective index change and 3-5 μm transmission in their base form, only the 40 PbSe maintains the transmission window after the heat-treatments used in this study.

The work reported in this thesis has shown how the crystallization process can be used to develop a gradient refractive index (GRIN) component in an IR optical system. While the composition and crystallization protocols are not optimized for further transfer of the technology to commercial products, the basis of this work shows the process of developing a glass-ceramic for the application.

ACKNOWLEDGMENTS

I would first like to thank my thesis advisor Dr. Kathleen Richardson at the University of Central Florida. She was instrumental in guiding through the course of my research. She was always supportive of my work and provided me with feedback when needed.

I would also like to thank the current and former member of the Glass Processing and Characterization Laboratory who were always there to give me advice on my research. I would especially like to thank Dr. Charmayne Smith whose hard work provided a foundation for this research and whose joyful attitude always made coming to the lab enjoyable.

This work was supported by AFRL Contract Number FA8650-12-C-7225. [PI: T. Mayer, Virginia Tech University; formerly Penn State University (PSU), K. Richardson (UCF), D. Werner (PSU), and C. Rivero-Baleine (Lockheed Martin Corporation)].

I would like to acknowledge the help and support that I received throughout my research from the Penn State team and Clara Rivero-Baleine at Lockheed Martin. I would especially like to thank Dr. Myungkoo Kang at PSU for his tireless work provided needed answers from TEM on morphology and composition.

Finally, I must express my very profound gratitude to my parents and to my friends for providing me with their unfailing support and continuous encouragement throughout my years in graduate school.

TABLE OF CONTENTS

LIST OF FIGURES

LIST OF TABLES

LIST OF ACRONYMS

AFRL	Air Force Research Laboratory
AMI	Amorphous Materials Inc.
ChG	Chalcogenide Glass
CTE	Coefficient of Thermal Expansion
DARPA	Defense Advanced Research Projects Agency
DI Water	Deionized Water
E_c	Activation Energy for Crystallization
FIB	Focused Ion Beam
FTIR	Fourier Transform Infrared Spectroscopy
GRIN	Gradient Refractive Index
HV	Vickers Hardness
IR	Infrared
LWIR	Long-Wave Infrared
MWIR	Mid-Wave Infrared
n	Refractive index
NIR	Near Infrared
PSU	Pennsylvania State University
Q	Heating Rate
R	Gas Constant
SEM	Scanning Electron Microscopy
SWaP	Size, Weight, and Power
T_g	Glass Transition Temperature
T_p	Peak Crystallization Temperature
T_Q	Quench Temperature
T_x	Onset of Crystallization Temperature
TEM	Transmission Electron Microscopy
UCF	University of Central Florida
UofR	University of Rochester
UV	Ultraviolet
V_x	Volume Fraction of Crystals
Vis	Visible Spectrum
XEDS	Energy-dispersive X-ray spectroscopy
XRD	X-ray Diffraction

CHAPTER ONE: MOTIVATION AND OBJECTIVE

Motivation

Chalcogenide glasses are well known for their mid-IR transparency and their high refractive index, but are often limited by their weak thermal/mechanical properties. Controlled crystallization of the base glass can improve these properties as observed in oxide glasses.[1-3] Additionally, introducing crystals may introduce other effects such as change in refractive index and nonlinear optical properties.[4-6] Recent activities by researchers have been focused on developing "manufacturable" gradient refractive index (GRIN) materials.[7] This thesis work supports a larger effort by the Glass Processing and Characterization Laboratory (GPCL) at UCF with collaborators at Penn State University (PSU) and Lockheed Martin (LMCO) which is examining how to create a gradient refractive index profile through selective crystallization in bulk chalcogenide glass (ChG) materials.[8] The effort by GPCL, PSU, and LMCO has resulted in a patent issued in 2016.[9] This work specifically examines key attributes of an important ChG system, its properties as related to the processing route used to prepare the glass, and the corresponding aspects of introducing a spatially controlled, secondary crystalline phase to realize an optical glass-ceramic nanocomposite.

In certain imaging applications, it has become increasingly important that systems exhibit fast optical designs (compact in footprint) and wide fields of view which requires many lenses using classic optical designs. The many optical components in these systems make it difficult to reduce size, weight, and power (SWaP) while maintaining optical function. Hence, reducing the total number of components by improving the optical functionality of individual elements can significantly reduce SWaP in the system.

Current materials used for GRIN profiles are not sufficient for advanced optical designs because they are limited by the maximum refractive index changes that are achievable. In order to attain these large refractive index changes, a new materials approach is necessary. In our team's nanocomposite (glass-ceramic) approach, precipitation (nucleation) and growth of high refractive index crystals in a (lower refractive index) chalcogenide glass matrix results in a change in the effective refractive index, n_{eff}, of the composite. If the formation of the secondary crystalline phase can be spatially varied in a controlled way (e.g. via a laser), a GRIN profile can be realized which yields a gradient in optical and physical properties. This modification is directly correlated to the volume fraction of the secondary phase in a specific location. As current GRIN technology is typically limited to axial or radial profiles, the selective crystallization process based on a spatially varying nanocomposite, would allow a fully three dimensional (3D) GRIN profile with excellent optical performance in the mid-infrared. While the creation of this GRIN profile is the ultimate goal of the main project, this is outside the scope of this thesis work.

Glasses from the $GeSe_2$-As_2Se_3-PbSe ternary have been chosen as the focus of this effort. In research by Yang et al.[10], this glass system was shown to produce glasses with good transparency in the mid-infrared and exhibited a narrow size distribution of crystallized phase.[10] These attributes suggested that further optimization of heat-treatment protocols to form the high index phase could result in a low scatter loss composite, if a small crystallite size could be maintained. Compositions in this system have been shown to nucleate PbSe crystals. PbSe crystals are well known for their high refractive index[11, 12] and for their luminescent properties as quantum dots.[11, 12] The high index

crystals and narrow size distribution seen in this glass system make it desirable to be used in the proposed chalcogenide GRIN system.

Objective

The overall aim of this thesis is to study the process of crystallization in phase-separated glass compositions in the $GeSe_2$-As_2Se_3-PbSe ternary. While crystallization in homogeneous, non-phase separated oxide and non-oxide glass materials has been well studied, examination of the role of the low crystallization resistant phase in a droplet-matrix phase separated morphology material on various aspects of glass-ceramic formation, has not been widely examined. It is necessary to understand how the nucleation and growth rates change with temperature and composition of the base glass, as well as the impact of the parent glass' morphology on the post-heat-treated physical properties of the resulting glass-ceramic. Since this system has shown the presence of nanoscale phase separation which is difficult to eliminate, it is critical to understand the effects of phase separation on the crystallization behavior in these glasses.

In order to study the effects of composition and phase separation on crystallization, two compositions spanning both sides of an immiscibility dome were investigated where the less stable, crystallization-initiating glass phase changes from droplet form to matrix form. While parallel work beyond this study is examining other methods (i.e. laser irradiation) to address the spatial control of nuclei formation, this study has exclusively examined a 'thermal' approach only, using a two-step heat-treatment protocol to both nucleate and grow, the resulting crystallites in the glass. The motivation is to understand how the thermally induced crystallization changes key

glass-ceramic optical and physical properties such that the crystallization process can be exploited for fabricating GRIN optical elements suitable for use in an IR optical system requiring 3 to 5 μm transmission.

CHAPTER TWO: INTRODUCTION

Glasses have been used for thousands of years for their desirable properties including optical transparency, isotropy, and moldability. The main aspects of a glass are its amorphous structure and time-dependent glass transformation behavior. Since the formation of a glass is a kinetic process, the cooling rate when forming the glass affects the properties of the glass such as its density, refractive index, glass transition temperature.[1] As seen in Figure 1, faster cooling leads to a larger specific volume and a higher glass transition temperature, T_g (T_g is approximately T_f).

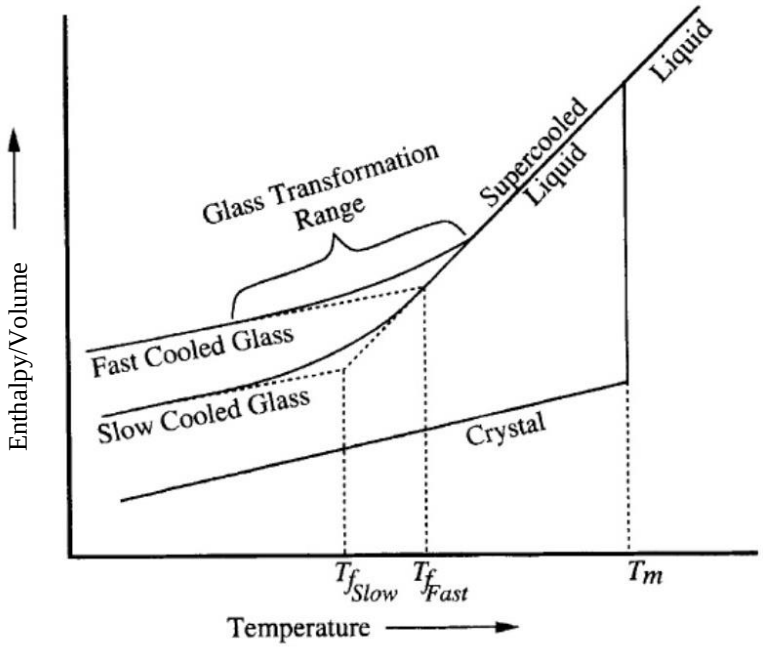

Figure 1- Effect of temperature on enthalpy/volume of a glass forming melt.[1]

The glasses under study were chalcogenide glasses (ChG). Chalcogenides are glasses whose primary network former is a chalcogen (group VI in the periodic table), excluding oxygen. These

glasses are well known for their transparency in the infrared (IR) and their high refractive index. Chalcogenide glasses are commonly used in rewritable memory applications,[13] chemical sensors,[14] and other IR optical systems.[15] The research presented in this thesis supports an effort to improve chalcogenide glasses through controlled crystallization, creating a glass-ceramic.

Glass-Ceramics

Glasses are widely used in many applications, but are sometimes limited by mechanical strength or thermal properties. Ceramming of the base glass to produce crystals can improve mechanical strength, coefficient of thermal expansion (CTE), and create zero porosity materials;[16] these properties are improved while maintaining some of the advantages of glass (isotropy, moldability, etc.).[1, 17] Some of the more famous glass-ceramics applications utilize an improved CTE over the parent glass through introduction of a secondary, crystalline phase. Examples of this include Corningware® cookware (lithium aluminosilicate glass-ceramic) and SCHOTT's Zerodur® space mirrors.[1, 3] Corningware® cookware's low CTE provides a good resistance to thermal shock and is a product of a low CTE glass phase and a low CTE crystal phase.[1] The Zerodur® glass-ceramic mirrors have a low CTE glass phase and negative CTE crystal phase producing a CTE that is very close to zero.[3] The key to an optical glass-ceramic is extremely small crystals with a refractive index that closely matches the parent glass.[1] The size of the crystals typically needs to be less than $\lambda/10$, where λ is the wavelength used in the application to reduce scattering (Mie) and thus maintain high transmission.[18]

Glass-ceramics can also be used in optical applications such as photo-thermo-refractive glass (PTR) and photochromic lenses.[4, 19] PTRs are glass-ceramics that undergo large refractive index changes after UV-exposure and thermal treatments due to the precipitation of nanoscale crystals in the areas exposed to UV radiation.[4] Photochromic glasses are similar in composition and processing approach and use light-induced bulk crystallization of silver halide particles to induce color change (for art applications) or to protect eyes from sunlight by creating a tinting effect of the glasses.[17, 19, 20]

The applications for chalcogenide glasses can often be limited by the weak mechanical properties and poor resistance to thermal shock of the glass which results from the weaker covalent bonding of large, group VI chalcogen ions which are often blended with similar heavy elements found in group IV or V. It is this same detriment to mechanical properties which enables infrared transparency. It is well known that controlled crystallization in chalcogenides can be quite difficult.[21] The low thermal conductivity of chalcogenide glasses can lead to a temperature gradient during heat-treatment which causes different crystallization rates across the sample. Chalcogenide glass-ceramics are being studied for applications in cars to aid drivers in low-light conditions and for applications in the photoelectric field due to their non-linear optical properties.[22, 23]

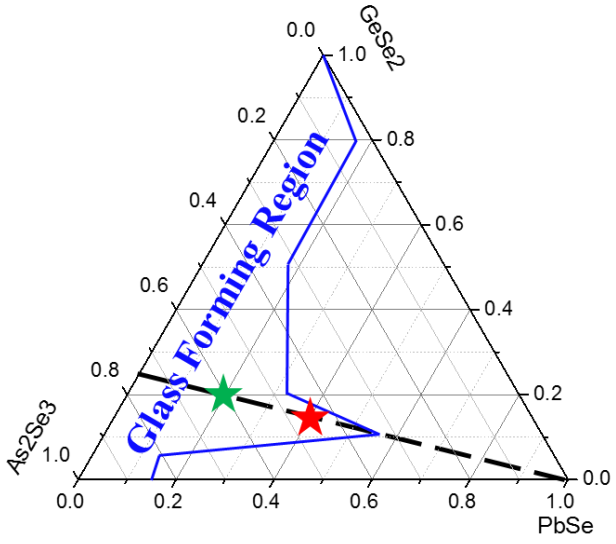

Figure 2- Glass forming region of $GeSe_2$-As_2Se_3-PbSe glass system.[10]

A study of glass formation and properties of $GeSe_2$-As_2Se_3-PbSe system was reported by Yang et al. from groups at the University of Rennes and East China University of Science and Technology.[10] In their work, they sought a suitable glass composition space for development of IR-transmitting chalcogenide glass-ceramic. In previous work by these groups,[24, 25] they demonstrated that a glass composition that is semi-stable to crystallization is key to producing IR-transmitting chalcogenide glass-ceramics. Compared to the similar previously reported GeS_2-Sb_2S_3-PbS system [24], the $GeSe_2$-based glasses have better rigidity, chemical stability, and transmit further into the IR.[10] Additionally, As_2Se_3 favors thermal stability which helps control the crystallite size during heat-treatment.[10, 25] Controlled crystallization of these glasses are important because uncontrolled crystal size leads to glass-ceramics which cannot transmit in the IR.[26, 27] Yang et al. mapped the glass forming region of this system (Figure 2).[10] In this system, the

relatively low Pb content is expected to fill the role of a nucleation agent with further heat-treatment,[10] as similarly reported for an analogous sulfide system.[24]

As introduced above, through strict control of the relative volume fraction of each phase (glass and crystallite) in the composite, two-phase material, effective properties can be estimated based on the lever-rule. The refractive index can increase if the crystal increases the local density or if the crystallizing species has a higher refractive index than the base glass. The effective refractive index, n_{eff}, is approximately given by Equation (1) where V and n are the volume fraction and refractive index of the indicated phase.

$$n_{eff} = \left(V_{glass}\right)\left(n_{glass}\right) + \left(V_{crystal}\right)\left(n_{crystal}\right) \qquad (1)$$

In this thesis work, crystallization was investigated as a mechanism for increasing the refractive index of the glass. The desired application needs this increase in refractive index, but it also needs to maintain the transmission from 3 to 5 μm. Small crystallites can increase the refractive index of the glass, but large crystals result in scattering which ruins the transmission. In order to take advantage of the refractive index increase, without losing transmission, the glass has to be crystallized in a controlled manner. To control the crystallization process, the nucleation and growth behavior has to be well understood.

Crystal Nucleation and Growth in Glass

The characterization of crystal nucleation and growth in glasses can be quite difficult due to the small sizes of the crystal and the necessary iterative nature of the experiments. Sometimes this characterization is measured directly through microscopy techniques, but if the crystallization rates are too high, the rates cannot be measured this way.[28] For a quantitative study of crystallization in glasses, differential scanning calorimetry (DSC) is an extremely valuable tool.[28] DSC studies of glass crystallization can be used to identify activation energy for crystallization [29, 30], nucleation curves (temperature vs. rate)[31], and growth curves (temperature vs. rate).[32]

Massera et al. performed an extensive study on nucleation and growth rates in TeO_2-Bi_2O_3-ZnO glasses.[28] They determined nucleation-like and growth-like curves, activation energy for crystallization, the Johnson-Mehl-Avrami exponent, and nucleation/growth rates as a function of composition using microscopy techniques and thermal analysis techniques developed by Marotta et al.[31] and Ray et al.[32] While this study was on tellurites, the same theory and techniques have been applied to chalcogenides as well to characterize the nucleation and growth behavior.[33-35] These studies were used as a basis for the development of nucleation and growth curves in the $GeSe_2$-As_2Se_3- PbSe system.

Crystallization is a two-step process involving an initial nucleation of the crystal followed by a growth of the nuclei by the addition of more atoms. There are two types of nucleation: homogeneous nucleation and heterogeneous nucleation. Homogeneous nucleation occurs when nuclei form spontaneously in the melt/matrix. Heterogeneous nucleation occurs when a nuclei

forms on a pre-existing surface or interface.[1] There are two barriers to the formation of nuclei in glasses: the thermodynamic barrier and the kinetic barrier. For the thermodynamic barrier, the formation of the nucleus must reduce the free energy of the system. At a given temperature, there is a critical radius at which a nucleus that spontaneously forms will reduce the free energy and the nucleus will be stable. As the temperature decreases, the size of the critical radius decreases making it more likely for nuclei to form and remain stable.[1, 36] For homogeneous nucleation in glass the change in free energy is represented by:

$$\Delta G = V\Delta G_V + A_S\gamma \qquad (2)$$

where V is the volume of the crystal embryo (nucleus), ΔG_V is the bulk free energy change, A_S is the surface area of the particle, and γ is the surface energy of unit area. When the crystals are small, the positive surface energy term dominates making them unfavorable causing them to redissolve into the matrix. When the crystals are larger than the critical nucleus size, the bulk free energy term dominates and the nuclei are stable and grow to larger sizes. In homogeneous nucleation, the interface that is being created is between the melt/matrix and the crystal. In the case of heterogeneous nucleation, the crystal is forming on an existing surface or interface. In this scenario, a smaller interface is formed between for the surface-crystal and crystal-matrix/melt. While the formation of these interfaces work against the creation of the nuclei, there is also the elimination of the interface between the surface and the melt/matrix which reduces the free energy of the system. The overall combination of the creation and elimination of interfaces leads to an overall reduction in activation energy needed for crystallization.[1, 36] Because of this, heterogeneous

nucleation is many orders of magnitude faster than homogeneous nucleation. It also follows that a system with more pre-existing interfaces (crystals, phase separation, voids) will have a higher nucleation rate compared to a system without such interfaces.

For controlled crystallization of a specific crystal phase, the ideal DSC thermogram will have distinct crystal peaks that do not overlap in temperature space. As seen in Figure 3, 15$GeSe_2$-45As_2Se_3-40PbSe (henceforth referred to as 40 PbSe) has two crystallization peaks at approximately 253°C and 313°C. This data shows that both peaks are distinct and isolated so their features are easy to characterize before and after heat-treatments. The two characteristics of crystallization peaks needed to create nucleation and growth curves are the peak crystallization temperature, T_P, and the peak area, A, respectively. The second crystallization peak seems to change very little with any heat-treatment while the first crystallization peak does. Because the first peak changes with heat-treatment and it is the lower temperature crystal phase it is possible to create nucleation-like and growth-like curves for the first crystal species using the methods described in Massera et al.[28]

The nucleation and growth DSC experiments referred to above were developed for homogeneous glasses. As noted previously, earlier work has shown the presence of an immiscibility dome in the $GeSe_2$-As_2Se_3-PbSe glass system.[37] While the nucleation and growth experiments have previously been developed for and applied to homogeneous glasses, they are still applicable to these phase separated glasses when using the same assumptions: uniform samples with no initial crystal nuclei. The DSC experiments will show the combined effects of the multiple phases. By isolating single

crystal peaks, the energetics of the specific phase's crystallization behavior can be evaluated regardless of the presence of the phase separation. The location of the crystallization must be evaluated by other techniques including electron microscopy.

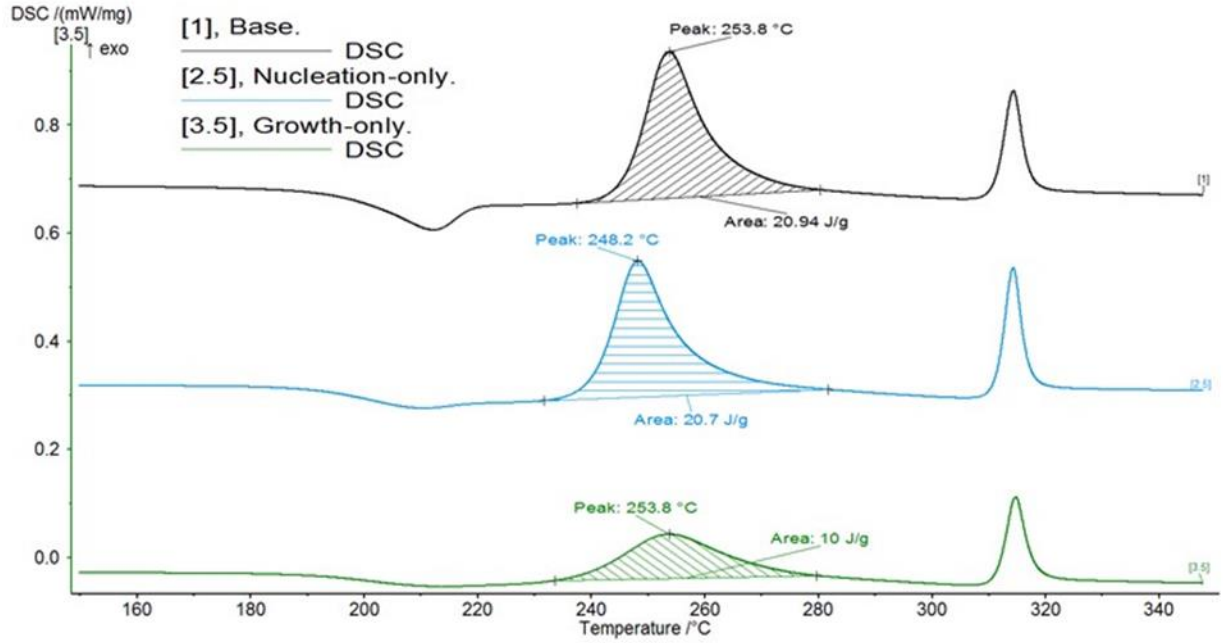

Figure 3 - $15GeSe_2$-$45As_2Se_3$-40PbSe DSC curves of base, nucleation-only, and growth-only heat-treatment

Phase Separation of Glass

Theoretically, there are two mechanisms for phase separation in glasses: nucleation/growth of droplets in a matrix and spinodal decomposition. In a diagram representing the change in free energy of mixing, ΔG_m, as a function of composition, the second derivative of the curve determines the mechanism by which the glass phase separates. In the immiscibility dome (region between *a* and *b* in (Figure 4)), the areas with positive second derivatives will phase separate through

nucleation and growth of droplets while negative second derivatives areas go through spinodal decomposition.

Systematic mapping of the phase separation regions in glasses is typically done by quenching glasses of the same composition from different temperatures. The resulting quenched samples are then evaluated via microscopic techniques to determine if phase separation is present. The immiscibility boundary for that composition can be defined as the temperature between sample showing phase separation and showing no phase separation. By repeating these experiments at various compositions along a tie line, the immiscibility dome can be mapped for the binary/pseudo-binary.[1]

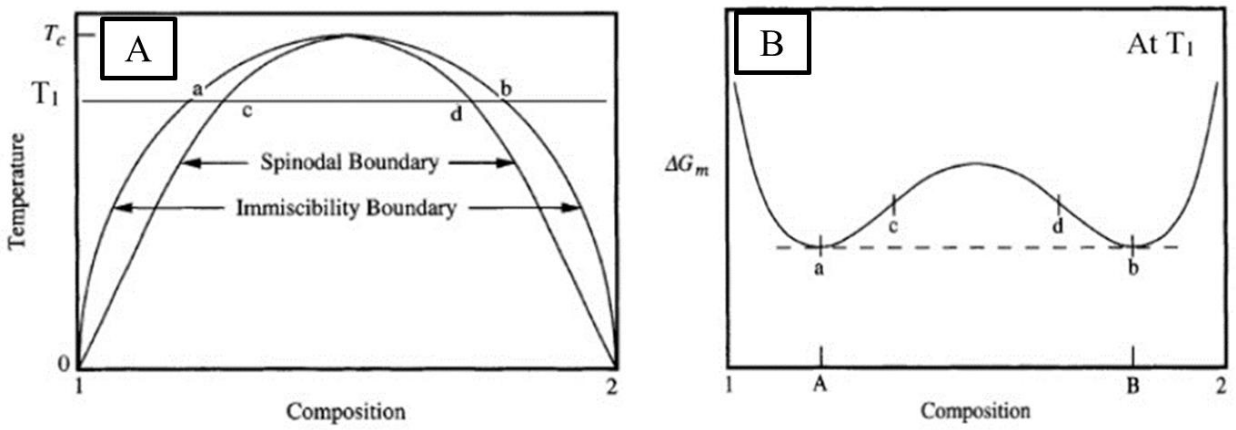

Figure 4 - (A) Theoretical idealized immiscibility dome in a binary system. (B) Free energy of a binary immiscible system at a temperature, T_1.Adapted from Shelby[1]

The techniques for detecting phase separation can be quite varied and the most appropriate one depends on the glass system. At its simplest, phase separation can be visually detected by looking for the presence of opalescence in a phase separated glass. This technique is not practical in a lot of studies because the observation of opalescence may only be present in cases of large phase

separation, where there is a large difference in refractive index between the separating liquid phases. This measurement can be aided by the use of a laser and a detector that measures scattering loss. This allows the detection of phase separation in a quantitative measurement as opposed to a qualitative measurement by measuring the scattering loss of the various samples.[1] Phase separation can be seen by other methods as well including x-ray small angle scattering (SAXS)[1, 38, 39] or electron microscopy[40, 41]. These techniques can be very instrument-intensive and expensive, but they are very accurate in measuring size and detecting phase separation.[1]

Chenu et al. studied the use of phase separation to create nanocrystalline microstructures in zinc gallogermanate glasses and glass-ceramics.[42] In their work, they melted and quenched glasses with nanometer scale droplet-matrix phase morphology. This system displays two crystallization features in the DSC upon heating, a low temperature and a high temperature peak. The low temperature peak corresponded with crystallization within the droplets while the high temperature peak corresponded with crystallization in the matrix. Because of this separation, a low temperature heat-treatment was found to nucleate and grow crystals in the droplets without any crystallization in the matrix. This treatment resulted in a final glass-ceramic composite with nanocrystals uniformly distributed in a glass matrix where the droplets were located.

Prior work by our group has shown that the $GeSe_2$-As_2Se_3-PbSe glass system has an immiscibility dome along the 100-X($GeSe_2$: 3 As_2Se_3)-X PbSe pseudobinary line.[37] Figure 5 shows the proposed immiscibility dome along this composition line generated by optical and physical property measurements on identical small melt samples (40g) subjected to the same melt/quench protocol.

This composition space showed droplet-matrix phase separation morphology across the entire immiscibility dome as determined by transmission electron microscopy (TEM). The outer limits of the immiscibility dome were found to extend from near 10 mol% PbSe to approximately 45 mol% PbSe. The precise position of these end points are dependent on cooling rate and quench temperature. Energy-dispersive X-ray spectroscopy (XEDS) mapping showed that the phase separation showed one Pb-rich phase and one Pb-deficient phase. Within the dome, there were two types of droplet-matrix morphologies. As depicted in Figure 5, one side of the dome showed Pb-rich droplets within a Pb-deficient matrix while the other side showed a Pb-rich matrix with Pb-deficient droplets.

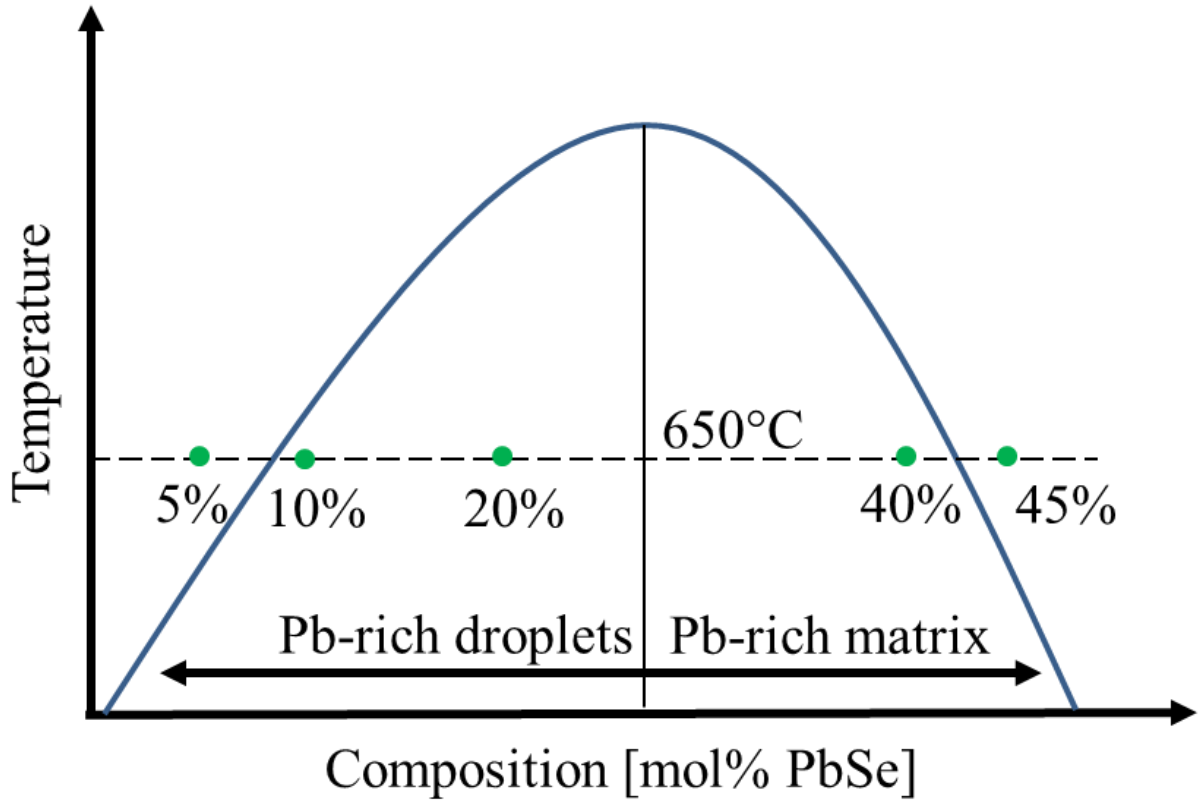

Figure 5 – Proposed immiscibility dome in $GeSe_2$-As_2Se_3-PbSe glass system along the 100-X ($GeSe_2$: 3 As_2Se_3)-X PbSe pseudo binary line at 650°C.

Scale-Up

For these materials to be considered suitable for further use in optical systems, the behavior of crystalline formation in the starting glass must be understood in melts created at a much larger scale than the lab-scale (melt sizes < 500g at UCF). Scale-up of the glass melt beyond the lab-scale sizes is desired to show that these compositions can be commercialized. As the size of melts increase, it becomes more difficult to extract the heat from the glass melt and thus decreasing the cooling rate. The cooling rate of a glass melt can have significant impact on the properties of the glass like T_g, density, and refractive index, as seen in Figure 1. Additionally, slow cooling rates may lead to the nucleation of crystallites or phase separated droplets.[1] While the slow cooling rates may have negative effects on the glass by producing these inhomogeneities, the slow cooling is required for yielding better (high) refractive index optical homogeneity. Index inhomogeneity typically occurs from compositional, and thereby density, fluctuations that result in striae. These striae are artifacts that degrade transmission through the optical component. Striae are typically 'born' upon cooling from the melting region at high temperatures when the molten glass is quite turbulent as gases escape the melt and convective currents flow within the melt. If the melt is rapidly quenched, the turbulent flow is "frozen" into the glass, resulting in bubbles or density gradients. Slow quenching allows the melt enough time to relax so that the fluctuations are not "frozen" into the glass. Other optical inhomogeneities in the glass may arise as the glass contracts when the temperature passes through the transformation region, near T_g. As the outside of the glass melt solidifies before the inside, the contraction during solidification can cause striations in the

melt which are then permanently frozen into the glass network. Such striae will be shown in the further FLIR images of fast versus slow cooled melts in the results and discussion chapter.

This chapter highlights some of the approaches used in experiments performed as part of this study to investigate crystallization behavior in the phase separated $GeSe_2$-As_2Se_3-PbSe glass system. The research focused on two glasses that represent the Pb-rich droplet morphology and the Pb-rich matrix morphology. These two compositions underwent rigorous testing of their properties and crystallization behavior.

The following chapters will outline the properties of the two compositions and the experiments that provided the data. The effect of the phase separation morphology on the crystallization behavior and post heat-treatment properties will be discussed. In addition to this, the issue of scale-up, examining more relevant cooling rates with increasing melt size towards commercial scale, will be demonstrated and discussed.

CHAPTER THREE: EXPERIMENTAL

In this chapter, we review the protocols used to batch, melt, quench, heat-treat, and measure the properties of the glass and glass-ceramic materials are discussed.

Sample Preparation

$GeSe_2$-As_2Se_3-PbSe glasses were batched in a MBraun Labmaster 130 glove box with a dry nitrogen atmosphere using elemental starting materials. All glasses were prepared using high purity raw materials (metals basis) from Alfa Aesar: selenium (99.999%), germanium (99.999%), antimony (99.999%), and lead (99.999%). No further purification for oxide or moisture removal was performed. The weighed batch was loaded into cleaned fused quartz tubes and sealed under vacuum to form sealed ampoules which then become the crucible for the melting. All glasses, unless otherwise stated, were melted in a rocking furnace overnight at a melting temperature, T_m = 850°C. The furnace was then cooled to the quench temperature, T_Q = 650°C, at 2°C/min prior to removal from the furnace for quenching. The glasses were removed from the furnace and quenched by flowing compressed air over the ampoules, constituting a 'fast' quench. In the initial part of this study, such an approach was chosen to minimize the extent of phase separation. The quench rate for this method was estimated to be ~120°C/min. The samples were subsequently annealed at 177°C for 2 hours to relax quench-related stresses in the glass. The melting and quenching protocol for these glasses were developed through trial-and-error to achieve robust glass samples that did not crack upon quenching and could be subsequently removed from the tube following annealing, for subsequent fabrication and analysis.

Fabrication of samples, if required for analysis, was performed by cutting 2.5 mm thick slices from the rod using a slow speed saw. These slices were then ground and polished by hand to form ~ 2 mm thick discs with two parallel polished surfaces. Grinding was done with silicon carbide grinding paper with finer and finer grit sizes. The final polishing step was completed using a polishing pad with 0.05 μm Al_2O_3 slurry. These fabricated samples were used for many measurements including transmission measurements, refractive index, and hardness.

The study focused on two glass compositions, 20 $GeSe_2$ – 60 As_2Se_3 – 20 PbSe (herein referred to as 20 PbSe) and 15 $GeSe_2$ – 45 As_2Se_3 – 40 PbSe (referred to as 40 PbSe). The atomic compositions of these glasses can be found in Table 1.

Table 1 – Atomic composition of 20 PbSe and 40 PbSe glasses

Component	20 PbSe (at%)	40 PbSe (at%)
Se	60.0	58.6
Ge	5.0	4.3
As	30.0	25.7
Pb	5.0	11.4

Bulk samples of glass were subsequently heat-treated to form glass-ceramics in furnaces in an open-air atmosphere, pictured below in Figure 6. The 40 PbSe glass samples were heat-treated at 210°C for 2 hours as a nucleation step followed by growth steps at 230°C, 240°C, or 250°C. The 20 PbSe glasses were heat-treated at 220°C for 2 hours as a nucleation step followed by growth steps at 250°C, 260°C, or 270°C. Physical and optical properties of the glasses were measured before and after heat-treatments.

Figure 6 – Furnace setup for nucleation and growth heat-treatments. Samples were placed on top of insulating fiber wool.

Physical Properties

The physical properties, including hardness and density, were measured for the glass and glass-ceramic materials in order to evaluate how bulk properties change as a result of crystallization in the two compositions.

Glass and glass-ceramic mechanical properties were characterized with Vickers microhardness, HV. These measurements were performed on glasses before heat-treatment, after the nucleation heat-treatment, and after the subsequent growth heat-treatment to evaluate the change in mechanical behavior with formation of the secondary crystalline phase. These hardness measurements assess the resistance to flaw formation in these brittle solids. The nucleation and

growth of crystals in a glass matrix should improve the hardness. Since the crystals are harder than the glass phase, the increased volume fraction of crystals will improve the overall hardness of the glass-ceramic composite.

Hardness measurements were performed on a Shimadzu DUH-211S Hardness Tester using a diamond indenter. Indents were created on polished sample surfaces using a 100 mN load with a hold time of 10 seconds. The hardness tester was calibrated using a metal calibration standard provided by Shimadzu. Sources of error can occur during this measurement if the sample does not have perfectly parallel surfaces or if there is extensive pre-existing surface damage (cracks or scratches).

The densities of the glasses and glass-ceramics were measured at every stage of heat-treatment. In most cases, crystallization in a glass matrix should lead to an increase in density as the atoms rearrange to have uniform bond lengths and angles. Such a change in density is important because it can directly affect the refractive index and can be correlated with extent of crystallization. Density was measured on glass samples using a method based on the Archimedes principle. The mass of samples in air (m_{air}), the mass of the samples submerged in DI water (m_{water}), and the density of water at the measurement temperature (ρ_{water}) were used to calculate the density of the sample (ρ_{sample}). The relationship can be seen below in Equation (3).

$$\rho_{sample} = \rho_{water} \frac{m_{air}}{m_{air} - m_{water}} \quad (3)$$

Thermal Analysis

Thermal analysis of the base glasses provides information on the glass transition and crystallization behavior. Thermal analysis was performed using a Netzsch DSC 204 F1 Phoenix Differential Scanning Calorimeter (DSC). Bulk samples of glass were finely crushed (< 125 μm) and put into sealed aluminum pans (20 ± 5 mg of glass). The base heating rate of the DSC curves was 10 °C/min. The DSC was calibrated by measuring the melting endotherms of indium, tin, bismuth, zinc, and cesium chloride standards. The instrument error on temperature after calibration was ± 2°C. The DSC was used to create nucleation-like and growth-like curves by analyzing curves after isothermal holds in the DSC. For these runs, the samples were rapidly heated (20°C/min) to a test temperature, held for a set time (30 minutes) then rapidly cooled below T_g before being ramped up at the normal base rate. The activation energy for crystallization was also determined using the DSC by methods described by Abdel-Wahab et al.,[43] Ozawa et al.,[44] and Matusita et al.[29] Heating rates of 10, 15, 20, 25, and 30°C/min were used to determine the activation energies by these methods.

The nucleation rate of a crystal species, I_0, can be determined by Equation (4):

$$\ln(I_0) = \frac{E_C}{R}\beta + C \qquad (4)$$

$$\beta = \left(\frac{1}{T_P} - \frac{1}{T_P^0}\right) \qquad (5)$$

where E_C is the activation energy for crystal growth, R is the gas constant, and C is a constant. T_P and T_P^0 are the temperatures corresponding to the maximums of the crystallization exotherms with

and without a nucleation step respectively.[28] During the nucleation step, the crystal species begins to nucleate throughout the sample. With these additional nucleation sites, the crystallization exotherm for this species will shift to lower temperatures compared to the base glass without the nucleation step. Since β is proportional to $ln(I_0)$, a nucleation-like curve can be made for a specific crystal species by plotting chosen nucleation temperatures on the abscissa and β on the ordinate. The creation of nucleation-like curves using this method was first shown by Marotta et al.[31]

Similar to nucleation-like curves, growth-like curves can be made for glasses through DSC isothermal holds by a process described by Ray et al.[32] The area of the crystallization peak is proportional to the volume fraction of crystals in the glass matrix. If growth occurs during the isothermal heat-treatment, the subsequent DSC run will show a crystallization peak with a smaller area compared to the base curve. By plotting the change in area of the peak against the temperature of the isothermal hold will produce a growth-like curve. For purposes of this work, we summarize the results of these measurements for the 20 and 40 PbSe compositions as nucleation-like (I) and growth-like (U) curves.

Structure and Morphology Characterization

X-ray Diffraction (XRD) was performed on the PANalytical Empyrean at Materials Characterization Facility at UCF. These measurements were run on the base and heat-treated glasses to see the evolution of crystal phases with heat-treatment. XRD was used to confirm the amorphous nature of the base glass and to confirm the presence of crystals in the heat-treated glasses. XRD in conjunction with selected area electron diffraction was used to identify the crystal

phases present in the heat-treated glasses. Diffraction patterns were referenced to the JCPDS database. Glass and glass-ceramic samples were finely ground and put in an aluminum sample holder. Scans were taken using Cu K_α radiation (1.54 Å) with a 2θ scan range from 10-70°.

Transmission Electron Microscopy (TEM) was performed on thin samples of glass. The images were obtained using 80 to 200 keV voltage, 1 nA current, and 57k – 225k magnification. Selected area electron diffraction (SAED) was performed on heat-treated glasses to confirm crystallinity and attempt crystal identification from the electron diffraction pattern. TEM samples were prepared by using a focused ion beam-assisted milling followed by a lift-out process at Penn State University. This was conducted using the FEI Helios 660 dual-beam with carbon and Pt GIS. Figure 7 shows the six sequential steps for the process. The first step involved protecting the region of interest from the ion milling by depositing layers of carbon. This protective mask was created using the GIS in the dual-beam instruments to deposit a thin layer of carbon assisted by the electron beam followed by further carbon deposition assisted by the ion beam to a thickness of 2 µm (step 1). After the carbon deposition, rough milling was conducted on regions adjacent to the protective layers to thin the region of interest and carbon protective layers to < 1 µm thick (step 2). The sample was then tilted to make a U-shaped cut on the sidewall of the thinned specimen using ion beam (step 3), and tilted back to thin it to < 500 nm (step 4). The W probe was then brought into contact with the top of the specimen and attached to the sample using ion-beam deposited Pt. The specimen was cut free from the sample by ion-milling through the two thin bridges of the specimen at either side of it, and lifted out of the rest of the sample (step 5). The specimen was then transferred over to a Cu TEM grid. The specimen was directed into contact with the grid, and

attached to the grid with ion-beam deposited Pt. The specimen was cut free from the probe and left attached to the Cu grid (step 6). The specimen was further thinned down to approximately 50 nm thick to allow sufficient electron transparency. Lower accelerating voltages (10 and 5 kV) were used for the final thinning step to decrease the depth of the ion damaged region on both sides of the sample.

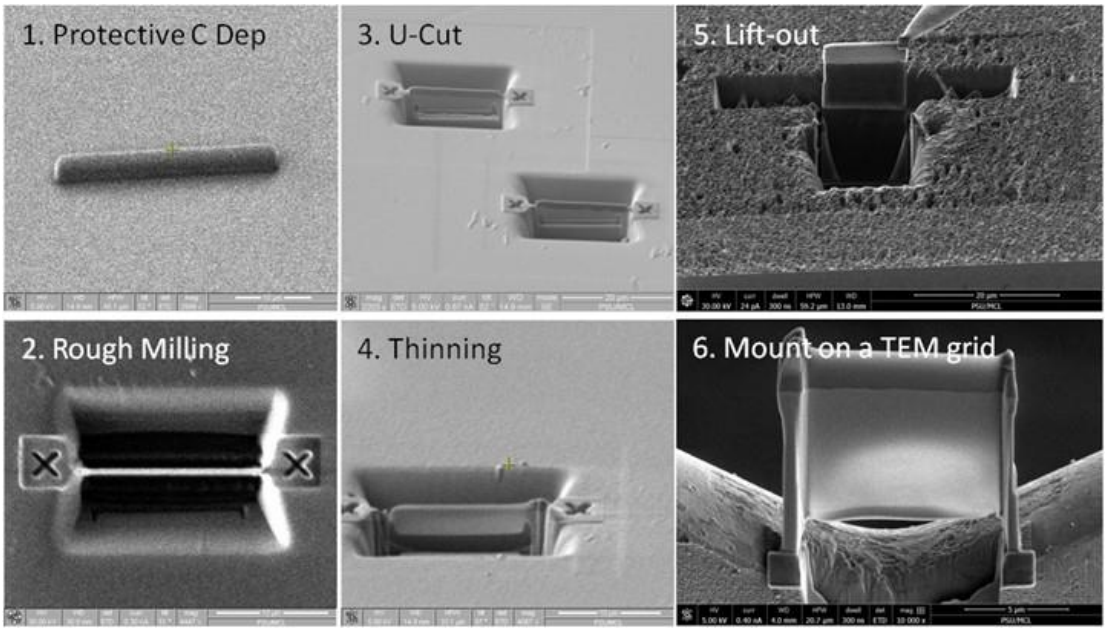

Figure 7 - The FIB-assisted lift-out process for the preparation of a cross-sectional TEM specimen

Energy dispersive x-ray spectroscopy (XEDS) was performed on the TEM samples to ascertain the how the elements were segregated in the glass. Additionally, semi-quantitative compositional analysis was performed to compare the compositions of the phases across multiple glasses. A commercial chalcogenide glass (Schott IRG24) was used as a reference for these semi-quantitative measurements seen below in Figure 8.

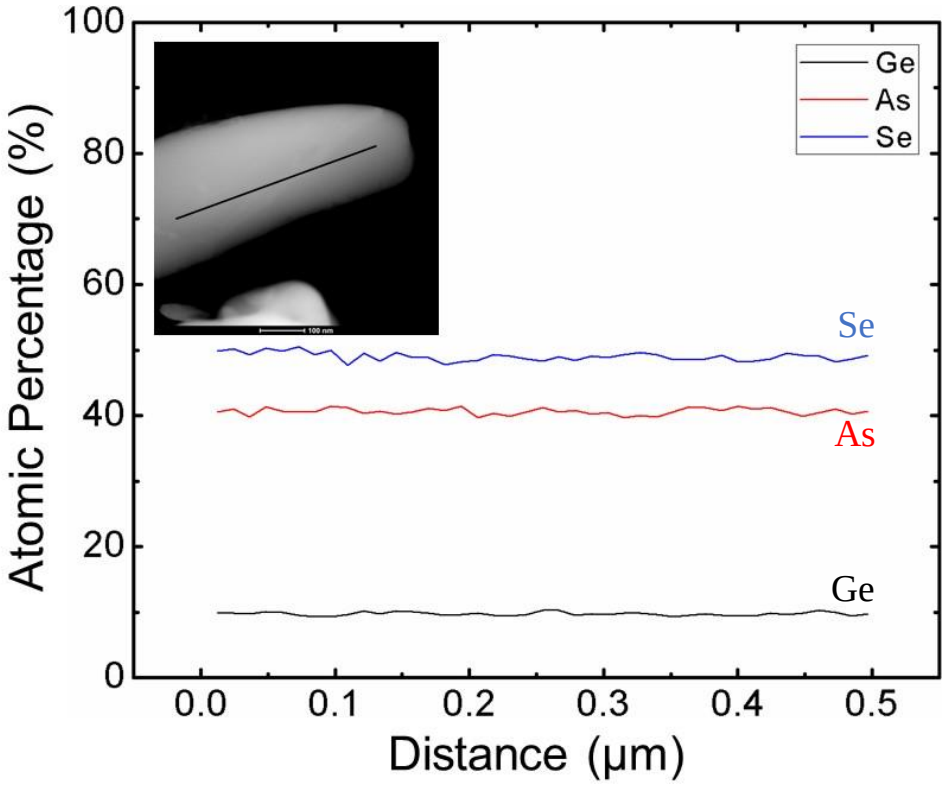

Figure 8 - XEDS line of Schott IRG24 ($Ge_{10}As_{40}Se_{50}$). Measurement error is approximately ± 1 at%.

Optical Properties

Applications of glass in optical components require good transmission and characterization of the refractive index. This is especially important in phase separated glasses where the multiple phases may cause light scattering. For this GRIN project, an increase in refractive index through crystallization is sought. Excessive crystallization can negatively affect the transmission. Therefore, it is important to understand how the refractive index and transmission window change with crystallization. This section outlines the measurements and instruments used to characterize these properties as a function of phase separation morphology and heat-treatment.

Transmission data was obtained using a ThermoFisher Scientific Nicolet iS5 Fourier Transform Infrared spectroscopy (FTIR). FTIR was performed on base and heat-treated samples (as described above). Measurements were done over a range of wavelengths from 1.4 to 25 μm on approximately 2 mm thick double-sided polished samples. For samples with significant transmission below the lower FTIR limit of 1.4 μm (e.g. the 40 PbSe glass), transmission was measured below 1.4 μm on a UV-Vis-NIR spectrometer. Sources of error for both instruments come from sample preparation where poor surface quality and wedging (i.e. non-parallel sides) reduces transmission.

Refractive index was measured before and after heat-treatment of the glasses using a Metricon Inc. prism coupler (2010M) that was modified to measure the index of bulk and thin film samples in the infrared. Specifics on the system modification and basic principles of its use and measurements on other chalcogenide glasses can be found in works by Carlie et al., Qiao et al., and Gleason et al.[45-47] The measurements reported in this thesis used either an optical parametric oscillator operating at 4.515 μm or a CO_2 laser operating at 9.294 μm. Ten measurements were performed on each sample to attain measurement errors of ± 0.0005 for the 4.515 μm laser and ± 0.0015 for the 9.294 μm laser. Two different prisms were used depending on the index of the sample. The lower index samples were measured using an undoped, single-crystal Ge prism (index range ~ 2.05 – 3.05). The higher index samples were measured using an undoped, single-crystal Si prism (index range ~ 2.95 – 3.35). The index measurements were calibrated using commercial samples (e.g. ZnSe and IG4) with known refractive indices. Sources of error for these measurements can come from poor surface quality which leads to poor optical coupling.

Quench Rate Experiments

In order to test the relationship between optical homogeneity, evidence of striae and our ability to translate the behavior of the smaller melts created in the UCF laboratory to commercial vendors, a comparison study examining quenching conditions in same size melts was developed. The goal of these experiments was to show how change in the quenching conditions affects optical homogeneity during scale-up. The two 100g 20 PbSe melts were batched in large 30 mm diameter silica tubes and melted. The melting parameters and quench temperature were kept the same for both glasses, but the quench method was altered to achieve different quench rates. The fast-cooled sample was quenched by removing the silica ampoule from the rocking furnace and set on a refractory brick while blasting it with compressed air to remove the heat. The slow-cooled sample was removed from the rocking furnace and left to cool in ambient air while set on the refractory brick. The melting and quenching conditions can be seen below in Table 2.

Table 2 – Melting and quench parameters for 20 PbSe fast and slow-cooled melts

	Fast-cooled	Slow-cooled
Size (g)	100	100
Diameter (mm)	30	30
Melt Temp. [°C]	850	850
Quench Temp. [°C]	650	650
Quench Method	Continuous air flow	No air flow
Quench Rate [°C/min]	120	48
Anneal Temp.[°C]	177	177
Anneal Time [hours]	2	2

The cooling rates of the fast-cooled and slow-cooled glasses were estimated by measuring the time-to-quench, t_Q, as the time from removal from the furnace to the point where the chalcogenide

glass pulls away from the walls of the silica ampoule. The glass is assumed to be at T_Q when removed from the furnace and at T_g when the glass pulls away from the walls.

In addition to the some of the basic property characterization described above (DSC, density, FTIR), the internal homogeneity was characterized using an infrared camera and IR interferometers (index uniformity) to assess if the resulting cooling rate impacted the presence of visible striae. Additionally, these same samples were measured for refractive index uniformity at the University of Rochester by the Moore Research Group to more directly quantify the impact of cooling rate on a commercially relevant metric, within melt index uniformity. High quality optical glass has a maximum peak-to-valley refractive index variation of 2×10^{-6} after extensive annealing.[48] While not needed for the present application, index changes induced by formation of crystal phases must be greater than the index non-uniformity throughout the slice of glass in order to be detectable. Hence, an index variation of $\sim 10^{-3}$, at minimum, would be required for this characterization.

The index uniformity measurements at University of Rochester were performed on a Mach-Zehnder interferometer at 4.5905 μm. The absolute refractive index at University of Rochester was measured on their Sagnac interferometer at 4.5905 μm. The Sagnac interferometer measures the deviation of the beam as it passes through the sample at different angles. These deviation measurements were then used to calculate the refractive index. Sources of error for these measurements come from poor surface quality of the test specimen, nonparallel sides, and severe internal striae as observed by imaging with a FLIR camera or interferometry. A detailed summary

of the specifications of sample shape and quality for these measurements can be found in Appendix B and Appendix C for reference.

CHAPTER FOUR: RESULTS AND DISCUSSION

This chapter presents the results of the base glass properties, the crystallization behavior of the glasses, a discussion on selecting glass-ceramic heat-treatment protocols, the effects of quench rate on properties, the effects of scale-up on the glass, and the glass-ceramic properties.

Base Glass Properties

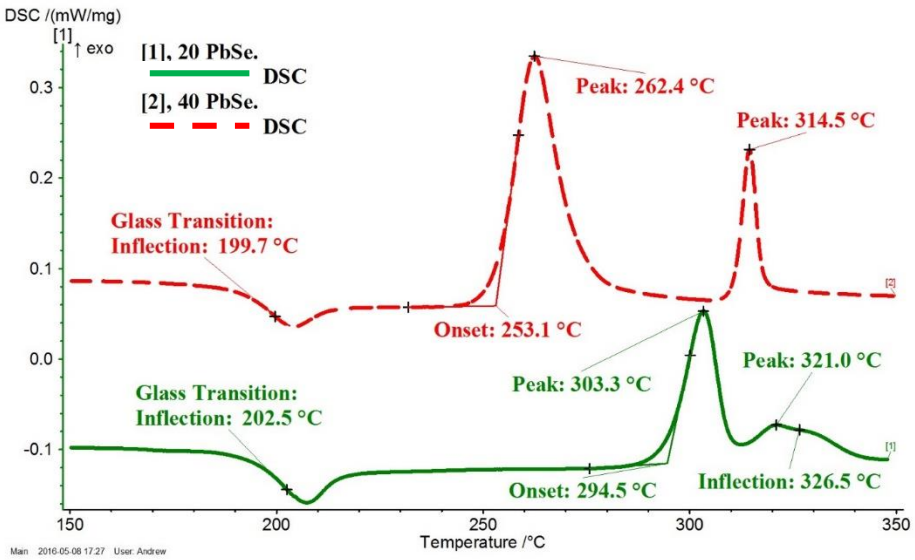

Figure 9 – DSC curves of 20 PbSe and 40 PbSe glasses. Heating rate:10°C/min (40g; 10 mm; T_Q=650°C)

In order to ascertain some of the key thermal properties of the as-quenched base glass, differential scanning calorimetry (DSC) was employed to evaluate the thermal attributes. Figure 9 shows the DSC curves for both glasses examined in our study. The 20 PbSe and 40 PbSe glasses show glass transition temperatures (T_g) around the same temperature at 203°C and 200°C, respectively. Here, we define T_g as the first point of inflection of the low-temperature endothermic feature. While the

T_g of the two glasses are similar, the crystallization features of the two glasses are very different. As can be seen, the 40 PbSe glass shows two distinct crystallization features with the onset of crystallization beginning at T_x = 253°C and two peak crystallization temperatures at 262°C and 315°C. The 20 PbSe glass shows one distinct crystallization peak followed by an asymmetric peak made of at least two crystallization features. The onset of crystallization for 20 PbSe is at 295°C with peak crystallization rates at 303°C, 321°, and 327°C for the three crystallization features.

The thermal stability of the glasses examined, ΔT, is defined as $\Delta T=T_x-T_g$. As ΔT increases, the more thermally stable the glass phase is and the less likely it is to crystallize. The ΔT values for the first crystallization peak in each of the 20 PbSe and 40 PbSe are 92°C and 53.4°C, respectively. The lower thermal stability of the high Pb glass is consistent with the observations by Xia et al,[24] in that they propose that Pb compounds act as a nucleating agent within the glass matrix; making it easier to crystallize. As the Pb-rich phase is in droplets for the 20 PbSe glass and in the matrix for the 40 PbSe material, the relative volume fraction of these poor crystallization stability phases will be markedly different and we may expect to see differences in both starting droplet-matrix composition and the subsequently formed, crystalline phases.

Table 3 shows some of the thermal properties of the base 20 PbSe and 40 PbSe glasses, with the error of the measurements shown. In addition to acting as a nucleating agent during crystallization, the large Pb atoms and their presence in higher concentrations in the 40 PbSe base glass, can be seen to affect the glass properties in several ways. Firstly, the Pb content increases the density as more and more Pb atoms are stuffed into the free volume of the glass network. The measured

densities seen in Table 3 clearly illustrate this trend as increasing PbSe content from 20 PbSe to 40 PbSe increases the density from 4.99 g/cm^3 to 5.54 g/cm^3. The refractive index of a material is closely related to its density so the increase in density is expected to be accompanied by an increase in refractive index.[1] This behavior is shown in these glasses with the low-Pb glass and high-Pb glass having refractive index values of 2.8490 and 3.0473 at 4.515μm., respectively.

Table 3 - Thermal and physical properties of 20 PbSe and 40 PbSe as-quenched base glass

	20 PbSe	40 PbSe
T_g [°C]	203 ± 2	200 ± 2
T_x [°C]	295 ± 2	253 ± 2
T_p [°C]	303 ± 2	262 ± 2
Density [g/cm^3]	4.99 ± 0.01	5.54 ± 0.02
Hardness [kg$_f$/mm^2]	161 ± 3.4	168 ± 3.2
Refractive Index (at λ in μm)	2.8490 ± 0.0005 (4.515) 2.8360 ± 0.0015 (9.294)	3.0473 ± 0.0005 (4.515) 3.0290 ± 0.0015 (9.294)

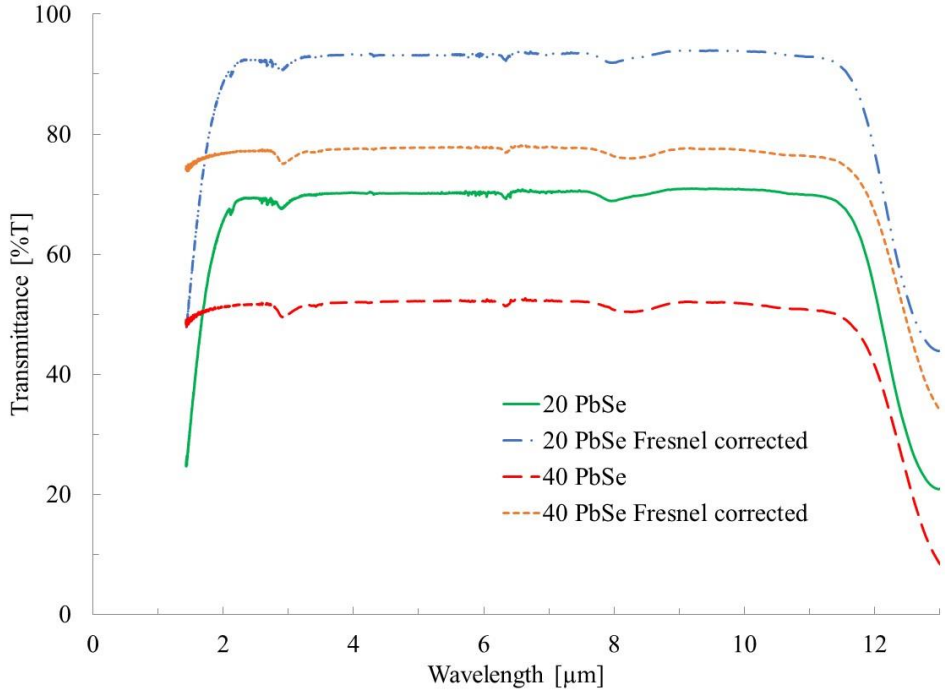

Figure 10 – Transmission window for 20 PbSe and 40 PbSe (40 g; 10 mm; T_Q = 650°C) Thickness normalized to 2 mm.

Key to understanding the pre- and post-heat-treatment suitability for use in an optical component is the glass/glass-ceramics' transmission across the infrared spectral region. The shape of the short wavelength (UV) edge of the glass is indicative of the magnitude of scattering loss induced by the crystallites (size and index). The transmission window for the as-quenched 20 PbSe and 40 PbSe base glass (40 g melts) are seen above in Figure 10. These measurements were performed on an FTIR system that has a range of 1.4 µm to 25 µm. The entire transmission window can be seen for the 20 PbSe. The limits of the transmission window are defined as 90% of the max transmission. Using this criteria, the transmission window of the 20 PbSe glass was found to be 1.993 µm to 11.705 µm. The long-wavelength cut off for the 40 PbSe can be seen at 11.712 µm. The short-

wavelength cutoff is below the range for the FTIR and can be seen below in UV-Vis-NIR figure and the short-wavelength cutoff is 1.319 μm.

The desired application for these glasses requires transmission in the 3 to 5 μm range. As can be seen, both of these glasses show good transmission over these ranges. The observed tail associated with the rapid quench of this small melt, cannot be assumed to be observed in larger melts that possess higher thermal mass and require slower cooling rates to avoid thermal shock and to ensure high optical homogeneity. Here, high homogeneity was not a primary objective of our study, but rather, the optical properties of the starting material and how this relates to the as-quenched morphology.

Larger melts will cool more slowly leading to larger, as-quenched droplets of the secondary, amorphous phase. While the glass remains amorphous, the index difference and size of the droplets will impact the sharpness (steepness) of the short wavelength edge for the glass. Crystallizing these glasses will cause the short-wavelength edge to shift to higher wavelengths due to the formation of scattering crystallites of different refractive index. As long as these crystallites remain below the 1/10 of the wavelength of light, the scattering tail is acceptable. It is important to be careful not to crystallize the glass too much as this might ruin the transmission.

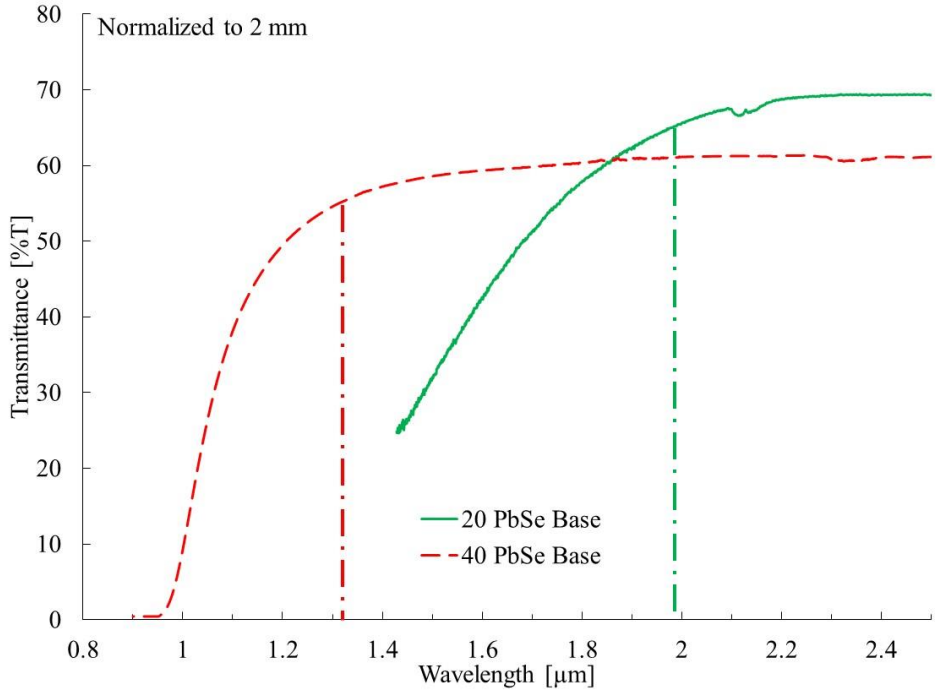

Figure 11 –Short-wavelength cutoff for 20 PbSe and 40 PbSe (40 g; 10 mm; T_Q = 650°C) Thickness normalized to 2 mm. Not corrected for Fresnel losses.

As mentioned above, the short-wavelength cut-off in transmission is strongly tied to scattering effects which result from phase inhomogeneities and the presence of multiple phases with different refractive indices present within the as-quenched or heat-treated (crystallized) material in the form of phase-separated droplets, crystallites, embedded particles (impurities), or striae. The $GeSe_2$ – As_2Se_3 – PbSe glass system has shown the presence of droplet-matrix phase separation in the as-quenched glass as quantified by both transmission measurements and electron microscopy. The droplets act as scattering centers that limit the low-wavelength transmission of the glasses. As the size and number of these scattering centers increase the low-wavelength cut-off of the glass will shift to higher wavelengths. If the scattering centers remain small in size, then the scattering effect

will be negligible. Since the low-wavelength cuff-off of the 20 PbSe is higher than the 40 PbSe glass, the 20 PbSe glass should have larger droplets than the 40 PbSe glass.

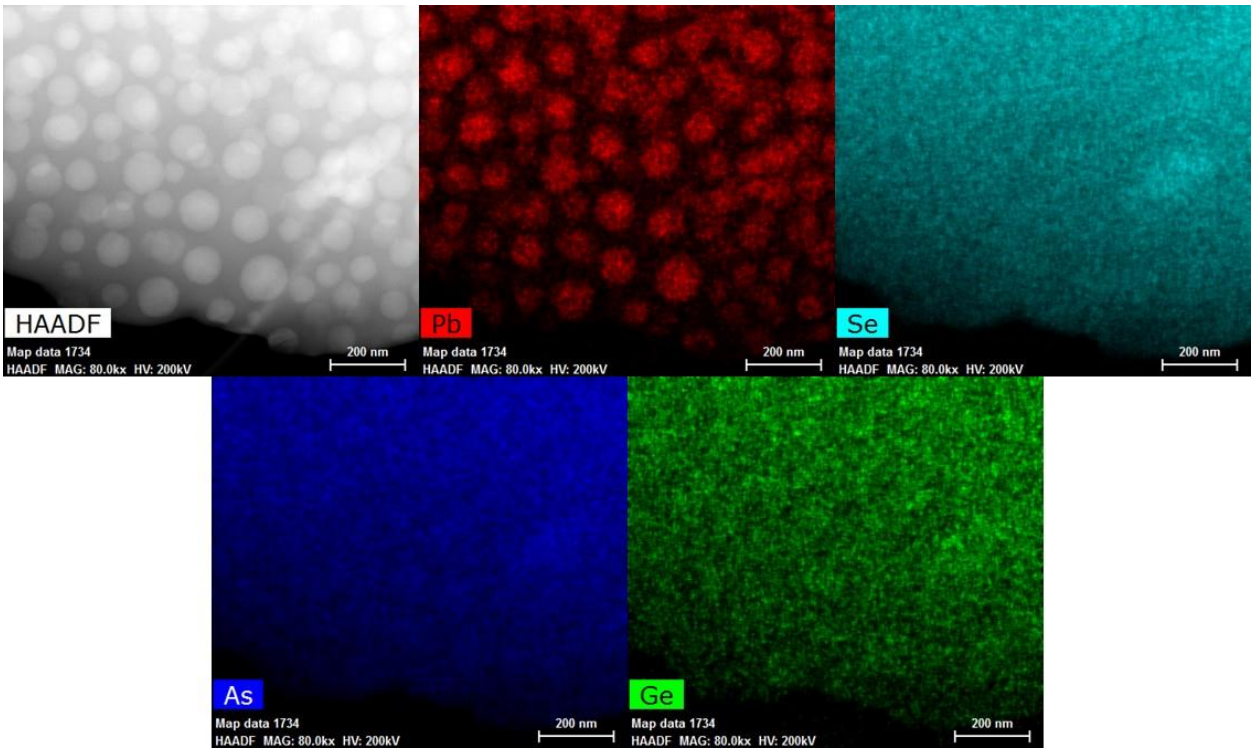

Figure 12 – TEM image and XEDS mapping of base 20 PbSe glass (40 g; 10 mm; T_Q = 650°C)

The TEM images of the base 20 PbSe glass, seen in Figure 12, show droplet-matrix phase separation in the glass matrix. The droplets are approximately 100 to 130 nm in size and the XEDS mapping shows that they are Pb-rich. Of the four elements that comprise this glass, only the Pb component shows any preference for phase segregation. This leads to Pb-rich droplets and a Pb-deficient matrix. As previously mentioned, the Pb is expected to promote crystal growth. For the 20 PbSe glass, subsequent heat-treatments of the Pb rich droplets should yield Pb-rich crystals in a Pb-deficient glassy matrix. Figure 13 shows quantitative compositional information of the

droplet and the matrix for the 20 PbSe glass. The XEDS line scan shows that the as-batched 5 at% Pb in the 20 PbSe glass disperses in both the droplets and matrix but is larger in the Pb-rich droplet phase. As seen, XEDS shows the Pb content to be ~ 7 at% in the matrix and peaks at ~ 18 at% in the droplets. The line scan also shows a slight decrease in the As and Ge in the droplets, suggesting a Pb rich glass composition. This localized decrease in As and Ge is not obvious in the color-coded, elemental mapping seen in Figure 12.

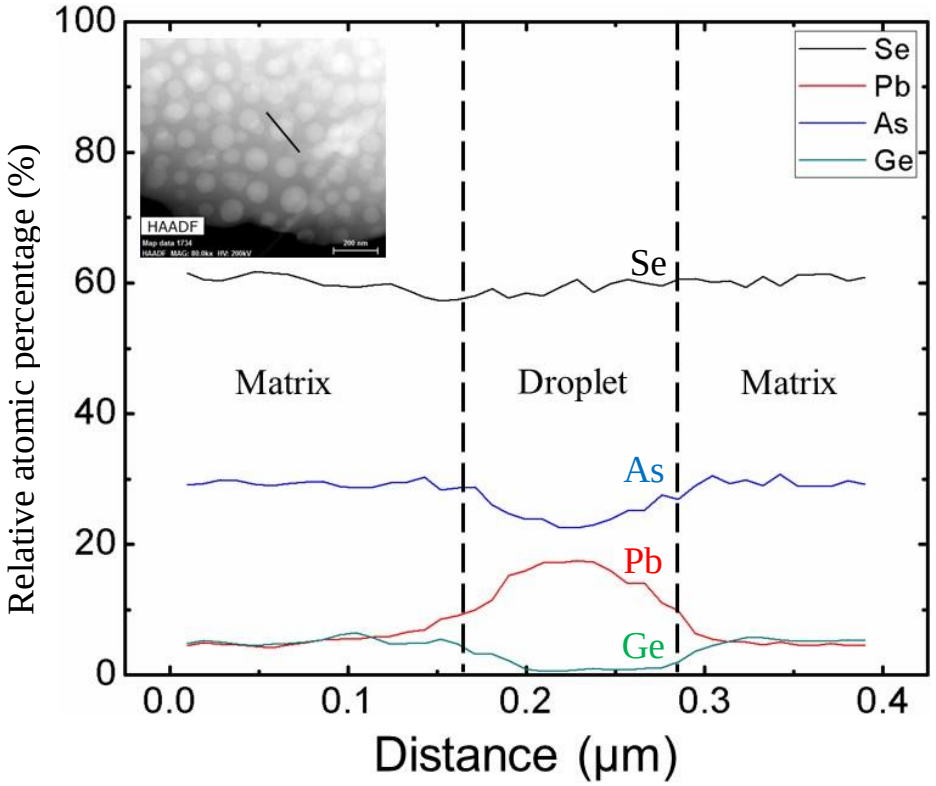

Figure 13 – XEDS line scan across droplet-matrix phase boundaries for base 20 PbSe glass (40 g; 10 mm; T_Q = 650°C). Error is approximately ± 1 at%.

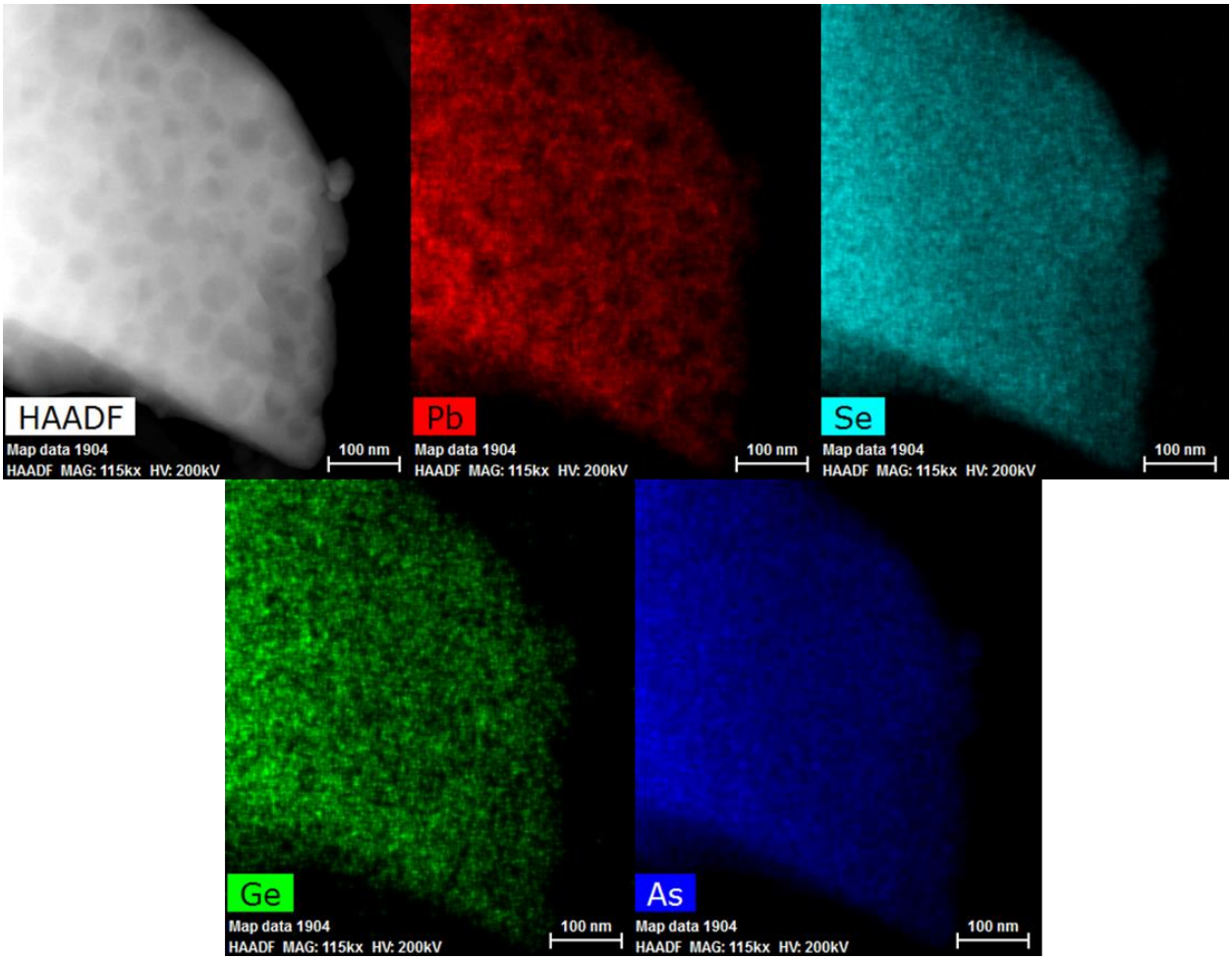

Figure 14 - TEM image and XEDS mapping of base 40 PbSe glass (40 g; 10 mm; T_Q = 650°C)

While the 20 PbSe glass showed Pb-rich droplets in a Pb-deficient matrix, the TEM images from the 40 PbSe glass, seen in Figure 14, clearly show the presence of Pb-deficient droplets in a Pb-rich matrix. In addition to the change in compositional morphology, the droplets in the 40 PbSe glass were found to be measurably smaller than those seen in the 20 PbSe glass. The 40 PbSe droplets were found to be approximately 35 to 45 nm in diameter as compared to 100 to 130 nm in the 20 PbSe glass. The size difference is likely due to their positions relative to the immiscibility dome. Since the 40 PbSe glass is closer to the edge of the immiscibility dome, the lever rule

predicts that the matrix will have a larger volume fraction in the 40 PbSe glass compared to the 20 PbSe glass which is further from the immiscibility dome edge. Because the Pb-rich phase is the matrix, crystallization is expected to occur in the matrix while maintaining amorphous droplets. The precipitating crystal species was expected to correspond with the first crystallization peak seen in the DSC curve. Compared to the 20 PbSe glass, the Pb-rich phase constitutes a much greater volume fraction of the melt. Because the Pb-rich phase is suspected to be the crystallizing phase under these heat-treatments, the crystallization process should show more effect on the bulk properties than the 20 PbSe glass. Similar to the data shown in Figure 12 for the 20 PbSe glass, Figure 15 shows relative quantitative compositional information of the droplet and the matrix. The as-batched Pb content for the 40 PbSe glass was 11.4 at%. The XEDS line scan shows that Pb content was ~ 11 at% in the matrix and reaches a minimum of ~ 5 at% in the droplets. The line scan also shows a decrease in Ge and an increase of As in the droplets (perhaps to compensate for the decrease in Pb and Ge) that is not obvious in the mapping seen in Figure 14. This suggests that the crystalline phase we might expect to see upon heat-treatment of the 20 and 40 PbSe glasses, would be different. As will be shown later in this section, indeed this is the case.

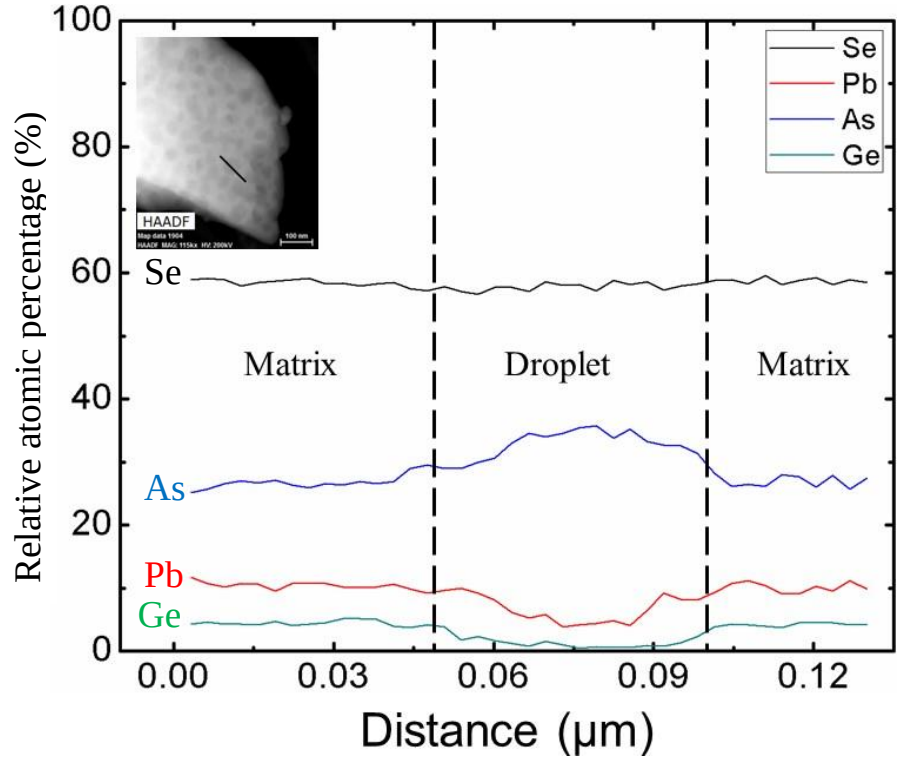

Figure 15 - XEDS line scan across droplet-matrix phase boundaries for base 40 PbSe glass (40 g; 10 mm; T_Q = 650°C). Error is approximately ± 1 at%.

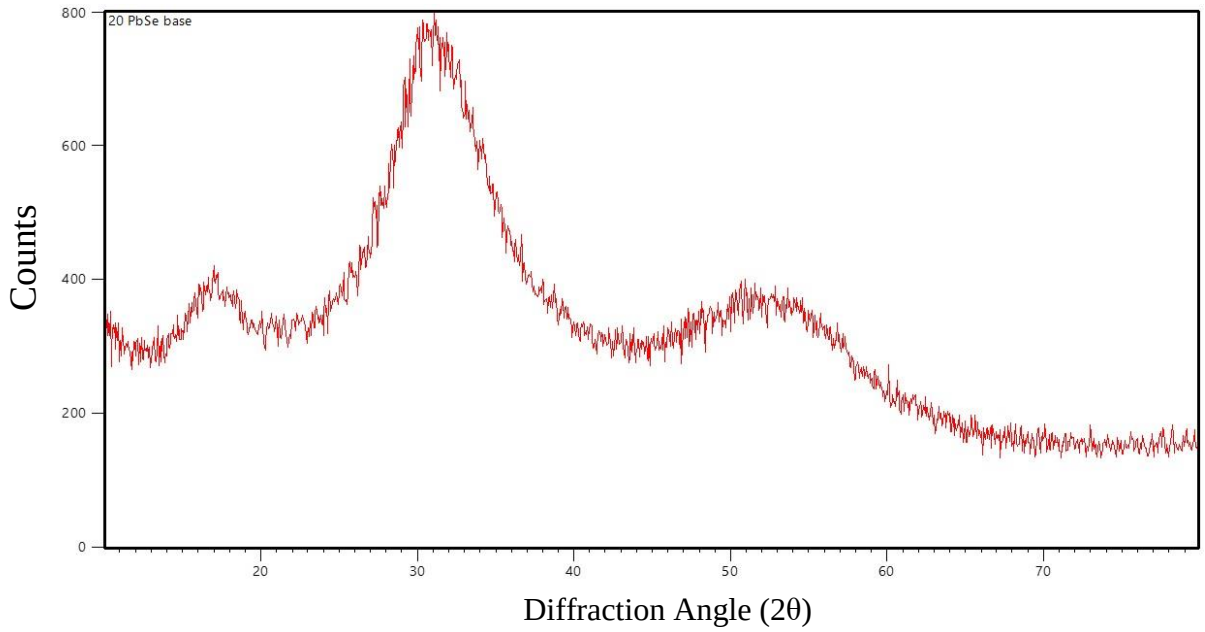

Figure 16 – XRD pattern of base 20 PbSe glass powder

To confirm that the as-quenched glasses are indeed amorphous and to assess the resulting crystalline phases imparted by post-thermal heat-treatments, X-ray Diffraction was used on powder samples of both glasses. Figure 16 and Figure 17 show the XRD patterns for the base 20 PbSe and 40 PbSe glasses, respectively. Both glasses show three broad amorphous humps. The three amorphous humps are located with peaks around 17°, 31°, and 53°. The lack of sharp peaks in these figures indicate that there were no measurable crystals located in the as-quenched glass. This was supported by the TEM measurements that also detected no crystals in the base glass.

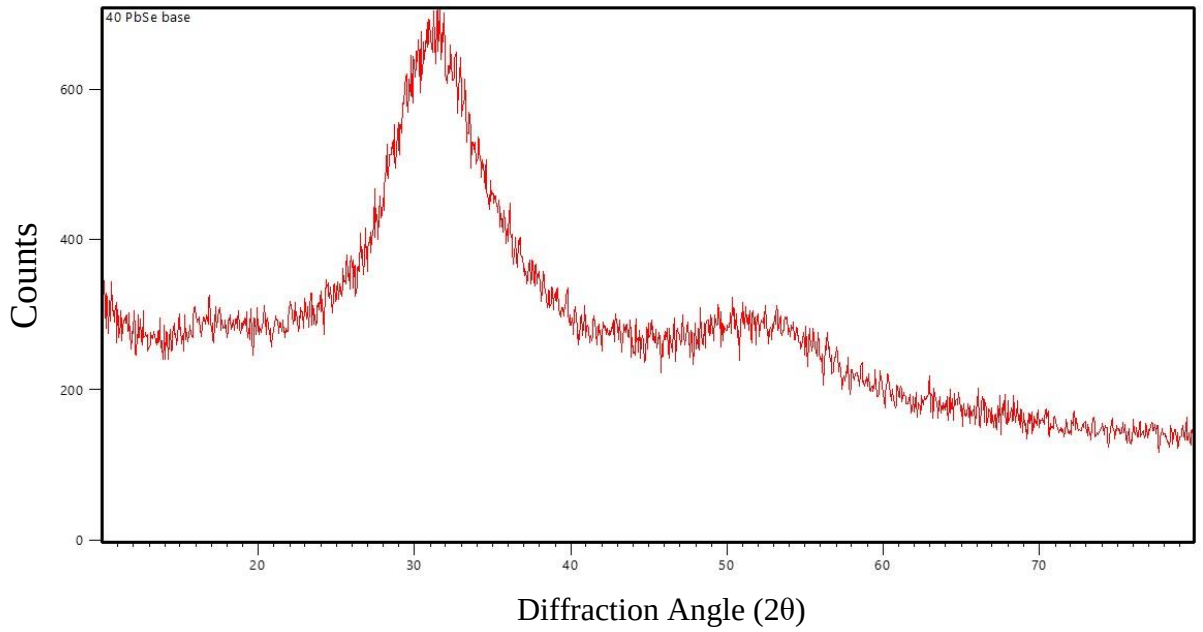

Figure 17 – XRD pattern of base 40 PbSe glass powder

Activation Energy of Crystallization

The base DSC runs of the 20 PbSe and 40 PbSe glasses showed that the thermal stability, ΔT, of the 40 PbSe glass was lower than the 20 PbSe. It was expected that the main crystal phase of the 40 PbSe glass would have a lower activation energy than the main 20 PbSe crystal peak because

of its lower temperature T_x value and higher bulk Pb content. These experiments sought to confirm this by measuring the activation energy by three commonly employed DSC techniques. While these tools are typically applied to homogeneous glasses, we have modified our approach and interpretation for these glasses since they start out phase separated.

The activation energy for crystallization, E_c, can be calculated for glasses through DSC measurements using several equations. The first method was based off the Kissinger equation seen in Equation (6).[43] This equation relates the activation energy to variations of peak crystallization temperature, T_p, with changes in heating rate, Q.

$$\ln\left(\frac{T_p^2}{Q}\right) = \left(\frac{E_c}{RT_p}\right) + constant \qquad (6)$$

The activation energy was determined from this relationship by plotting $1000/T_p$ against $\ln (T_p^2/Q)$. The slope of the trend line gives E_c/R where R is the gas constant and the activation energy is given in kJ/mol. Figure 18 shows the plots for the main peak of the 20 PbSe glass and both peaks for the 40 PbSe. The activation energies for the main 20 PbSe peak, the first 40 PbSe peak, and the second 40 PbSe peak were found to be 113 kJ/mol, 144 kJ/mol, and 285 kJ/mol, respectively.

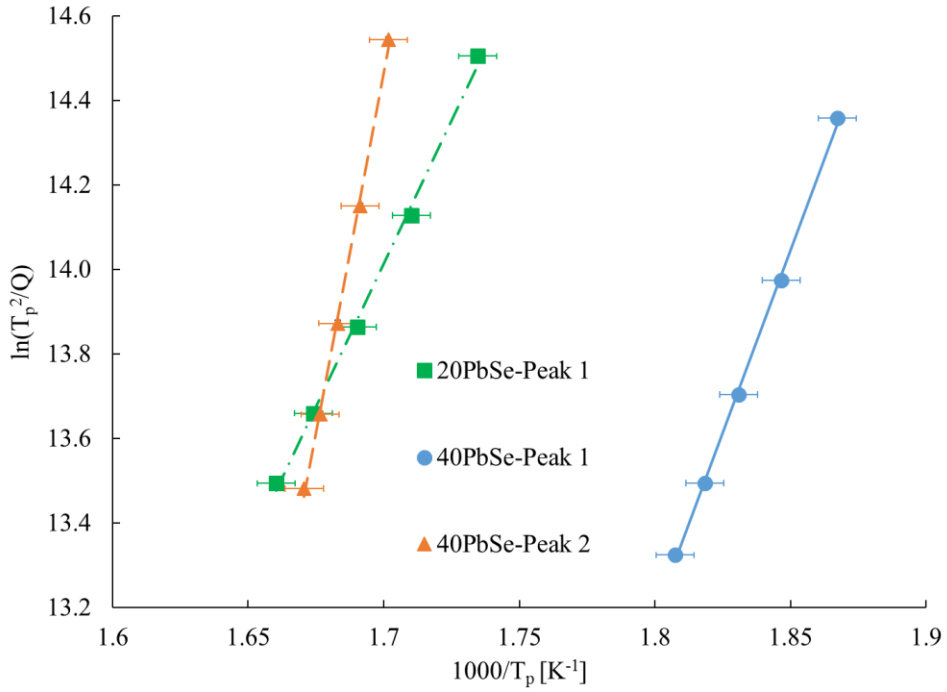

Figure 18 – Plots of ln (T_p^2/Q) versus 1000/T_p used to determine activation energy of crystallization through the Kissinger equation. (40 g; 10 mm; T_Q = 650°C)

The second method used an equation proposed by Augis-Bennett.[49] Equation (7) shows this relationship which is similar to the Kissinger equation, but includes a term involving the frequency factor, K_0. Figure 19 shows a plot of 1000/T_p against ln (T_p/Q) of the three crystals peaks. Just like the Kissinger method, the slope of these lines give E_c/R. The activation energies for the main 20 PbSe peak, the first 40 PbSe peak, and the second 40 PbSe peak were found to be 118 kJ/mol, 149 kJ/mol, and 290 kJ/mol, respectively. One would thus expect that these activation energies should coincide with the least to most resistant phase that could evolve from the as-quenched glass upon heat-treatment.

$$\ln\left(\frac{T_p}{Q}\right) = \left(\frac{E_c}{RT_p}\right) + \ln K_0 \qquad (7)$$

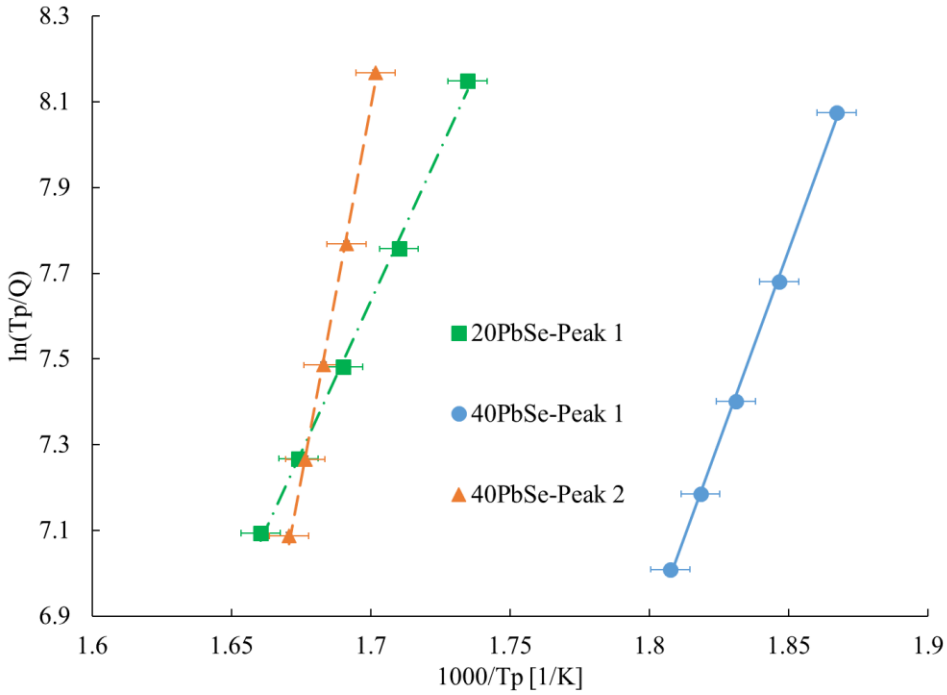

Figure 19 - Plots of ln (T_p/Q) versus 1000/T_p used to determine activation energy of crystallization through the Augis-Bennett equation. (40 g; 10 mm; T_Q = 650°C)

The third method is based off the Ozawa equation,[29] seen in Equation (8). As opposed to the other two equations, this method uses the onset of crystallization, T_x, instead of T_p. Figure 20 shows the plot of 1000/T_x against ln Q for the main peaks from 20 PbSe and 40 PbSe. The activation energies for the main 20 PbSe peak, the first 40 PbSe peak, and the second 40 PbSe peak were found to be 123 kJ/mol, 153 kJ/mol, and 295 kJ/mol, respectively.

$$\ln Q = \frac{-E_c}{RT_x} + constant \qquad (8)$$

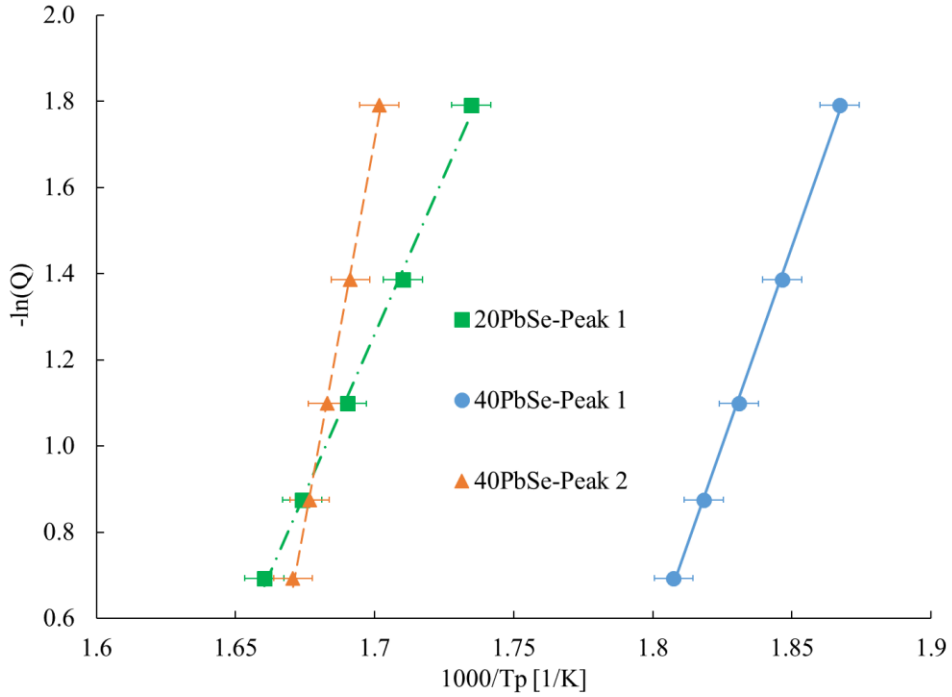

Figure 20 - Plots of -ln(Q) versus 1000/Tp used to determine activation energy of crystallization through the Ozawa equation. (40 g; 10 mm; T_Q = 650°C)

Table 4 shows a summary of the activation energies calculated from the three methods. Each method provides a different value but they generally agree with each other in their trends across the three peaks examined.

The average activation energies for the main 20 PbSe peak, the first 40 PbSe peak, and the second 40 PbSe peak were found to be 118 ± 5 kJ/mol, 149 ± 5 kJ/mol, and 290 ± 5 kJ/mol, respectively. This data suggests that the main crystal phase of the 20 PbSe glass should have a lower energy barrier to crystallization the crystal phases of the 40 PbSe glass.

Because of the high bulk Pb-content, the first 40 PbSe crystal phase was expected to have a lower activation energy than the main crystal phase of the 20 PbSe glass. While this was expected, the

results from the activation energy experiments seem to display the opposite behavior. This can be best explained by looking at the XEDS line scans in Figure 13 and Figure 15. While the 40 PbSe glass has a higher bulk concentration of Pb (11.4 at%) than the 20 PbSe (5.0 at%), the XEDS line scans showed that the 20 PbSe droplets (18 at%) had a higher Pb concentration than the 40 PbSe matrix (11.0 at%). The segregation of the Pb atoms from the phase separation causes higher local Pb concentrations which leads to the unexpected lower activation energy of the 20 PbSe main crystal peak.

Table 4 – Activation Energies [kJ/mol] determined through the Kissinger, Augis-Bennett, and Ozawa equations

	Kissinger	Augis-Bennett	Ozawa	Average	STDEV
20 PbSe-1st peak	112.71	117.61	122.51	117.61	4.90
40 PbSe-1st peak	144.01	148.54	153.06	148.54	4.53
40 PbSe-2nd peak	285.05	289.98	294.91	289.98	4.93

Nucleation and Growth

Nucleation-like and growth-like curves provide information on the relative rates of nucleation and growth of crystals in the glass matrix as a function of temperature, but does not give absolute values. Understanding the temperature regimes and rates (i.e. timescales for nucleation and growth at specific temperatures) for nucleation and growth are important to know in order to control the number and size of crystals in the glass matrix. This behavior can be used to define the suitable temperatures and times for heat-treatments used to generate crystals with controlled number density (defined in the nucleation step) and final size (defined in the growth step).

In an “ideal” material for controlled crystallization, the nucleation-like and growth-like curves would be well separated. If the nucleation and growth behaviors overlap in temperature space, heat-treatments in the overlap region lead to a broader size distribution of crystal sizes, as early nuclei grow while new nuclei form. Good separation of the two rate curves allows for the implementation of a two-step heat-treatment where the first step nucleates crystals in the matrix without appreciable growth and the second step grows the previously nucleated crystals without generating additional new nuclei. This two-step heat-treatment procedure yields crystals with a narrow size distribution.

In this nucleation and growth behavior study, four melts were investigated. Two small (40 g; 10 mm) melts of 20 PbSe and 40 PbSe were created and used to define heat-treatment protocol for the glass-ceramic study. Additionally, two larger melts for 20 PbSe (150 g; 30 mm) and 40 PbSe (400 g; 30 mm) were prepared and characterized in order to see how melt size might change the behavior. This analysis would provide insight as to the scalability of a specific thermal heat-treatment protocol in a scaled up glass.

The nucleation and growth behavior of two 20 PbSe melts of differing size (and thus cooling rates) are shown in Figure 21 and Figure 22. The glasses in these figures were of a small melt (40 g; 10 mm) and large melt (150 g; 30 mm) respectively. Both glasses underwent the same melting/quenching conditions with the only difference being the size of the melts and the diameter of the quartz tubes within which they were melted. The greater melt volume and the larger diameter of the tube, the longer pathway for heat to escape during the quenching process. This should lead

to different cooling rates for the two melts and would be expected to be most prominent in the center of the melts. While it is often assumed that these glasses have no as-quenched nuclei, there is likely a small amount of as-quenched nuclei, as suggested by the exotherms in the DSC curves. The difference in the number of as-quenched nuclei may lead to differences in nucleation and growth behavior. If there are more as-quenched nuclei (as one might expect in a glass that saw a slower cooling rate from the melt), the nucleation rate may be lower due to saturation of the nucleation sites. Additionally, more as-quenched nuclei could lead to a shifting of both the nucleation and growth curves as more potential sites for crystallization are formed sooner in the thermal process.

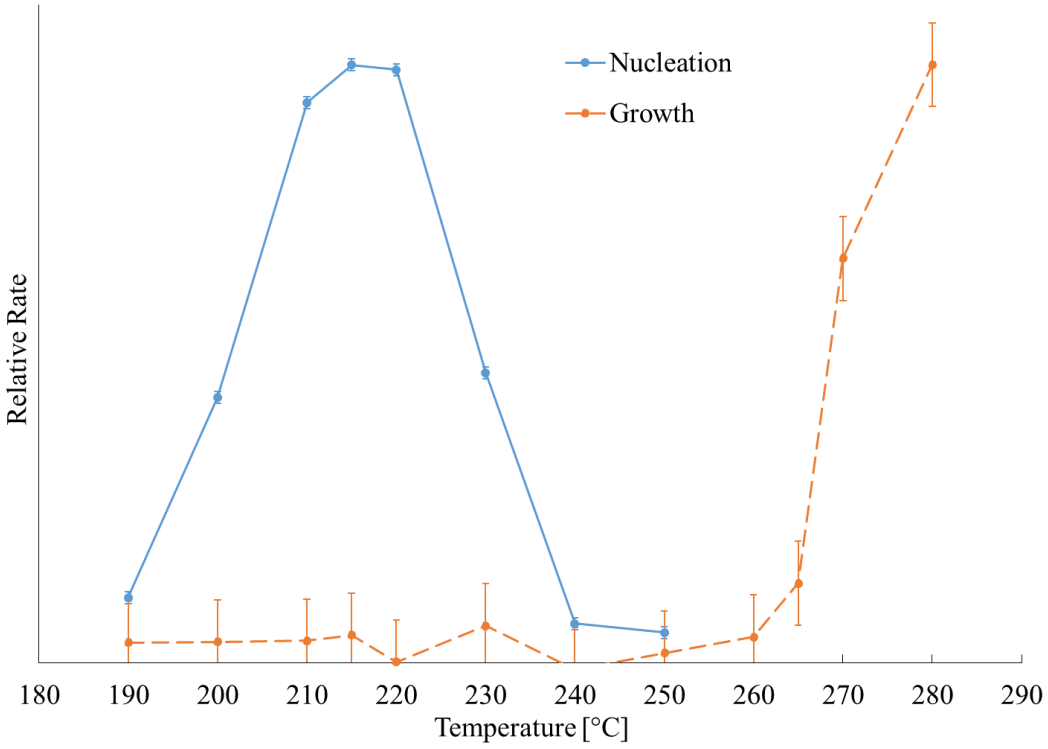

Figure 21 – Nucleation-like and growth-like curves for 20 PbSe (40 g; 10 mm; T_Q = 650°C)

As seen in Figure 21 and Figure 22, the nucleation rates of both large and small melts show similar behavior with their maxima nucleation in the 215°C – 220°C range and the nucleation regime between 190°C and 240°C. This suggests that in the lower PbSe containing glass, the concentration of as-quenched nuclei is likely similar. The growth behavior is also similar, but the large melt shows higher growth rates over the 260°C to 270°C range compared to the smaller 40g melt, reaching its maximum measurable growth rate at 270°C as opposed to the small melt which reaches its maximum measureable growth rate at 280°C. This can likely be explained by the presence of a larger number of as-quenched nuclei in the large melt which would be expected to cool more slowly due to its larger volume. With more nuclei, there are more sites for subsequent crystal growth which increases the rate at which the volume fraction of crystals reaches the saturation point. Here, the saturation point is defined as the point where the material no longer shows signs of further crystallization, likely due to a consumption of species required for the crystal phase to form/further grow. This happens when there is no longer any of these constituents in the (nearby) residual glass phase to crystallize, or the migration distance is too far for that species to travel, or the residual glass phase becomes stable once depleted of crystal-forming constituents as compared to the crystal of interest.

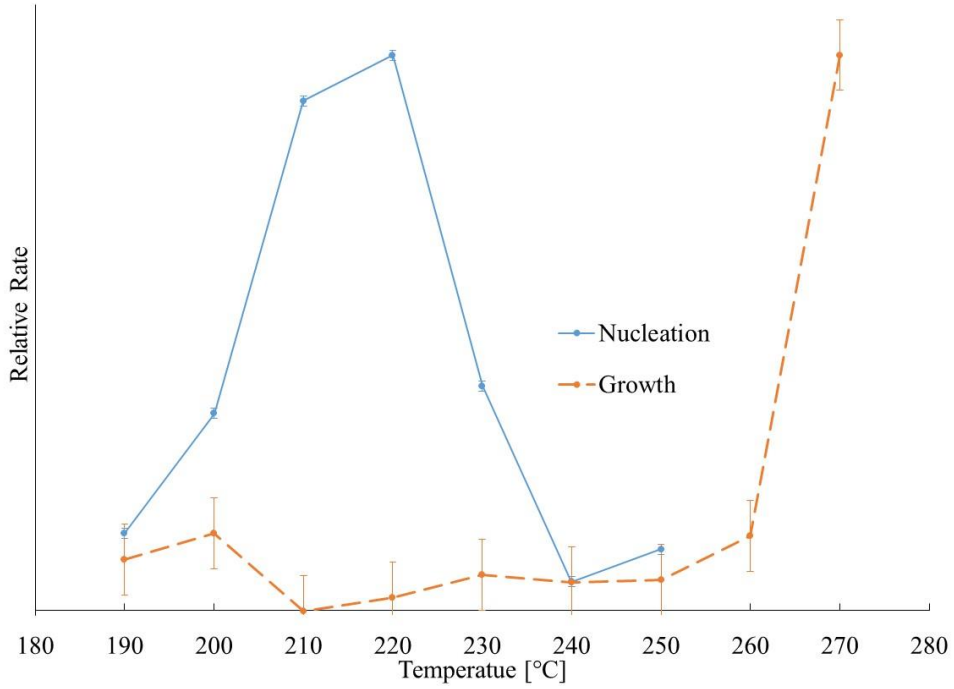

Figure 22 – Nucleation-like and growth-like curves for 20 PbSe (150g; 30mm; T_Q = 650°C)

In the figures, there is a clear separation of the nucleation-like and growth-like curves an aspect that is desirable for making glass-ceramics based on a thermally separated, two-step heat-treatment protocol. The growth regime does not begin until 20-25°C after the nucleation regime ends. This composition's separated nucleation and growth curves makes it favorable for use in controlled crystallization. While the 20 PbSe composition shows good separation between the nucleation and growth curves, the nucleation and growth curves of the 40 PbSe glasses, Figure 23 and Figure 24, shows that the nucleation and growth curves overlap with growth starting to increase near the maximum of the nucleation rate.

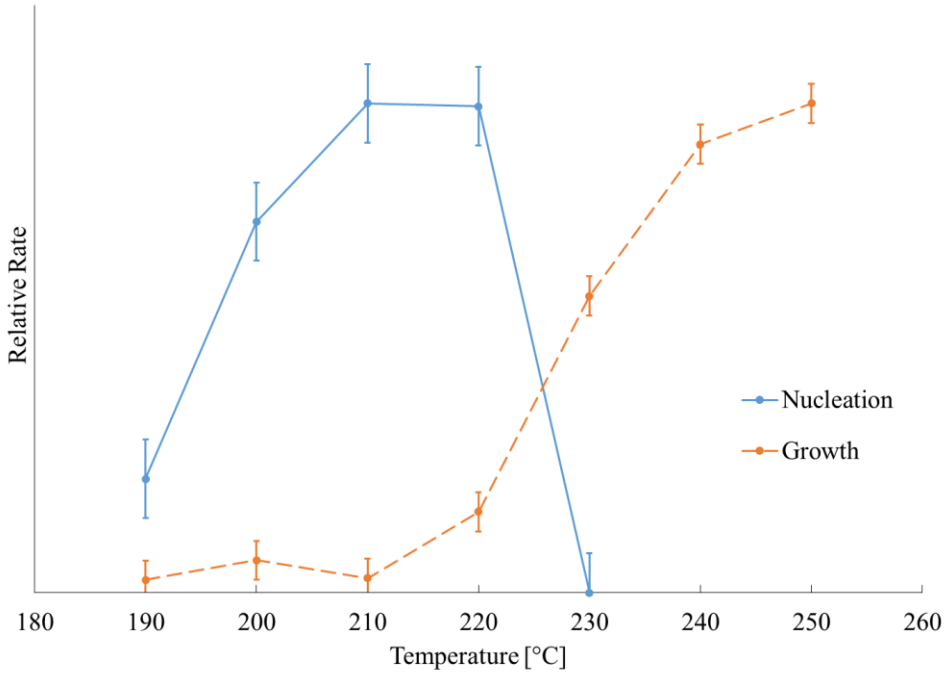

Figure 23 – Nucleation-like and growth-like curves for 40 PbSe (40g; 10 mm; T_Q = 650°C)

The nucleation and growth behavior of two 40 PbSe melts are shown in Figure 23 and Figure 24. The glasses in these figures were of a small melt (40 g; 10 mm) and large melt (400 g; 30 mm) respectively. Both glasses underwent the same melting/quenching conditions, with the same variation as noted above expected due to melt volume and cooling rates in 10 mm versus 30 mm tubes. The nucleation rates of both large and small melts show the same behavior with their maximum nucleation in the 210°C – 220°C range and the nucleation regime between 190°C and 230°C. The growth rates of both glasses show the same behavior with the growth regime starting at 220°C and reaching the maximum measurable growth rate at 250°C. While the 20 PbSe glasses showed different growth behavior, the 40 PbSe glasses did not. From this, it can be reasoned that difference in as-quenched nuclei between the large and small melts were not as significant as in the 20 PbSe melts.

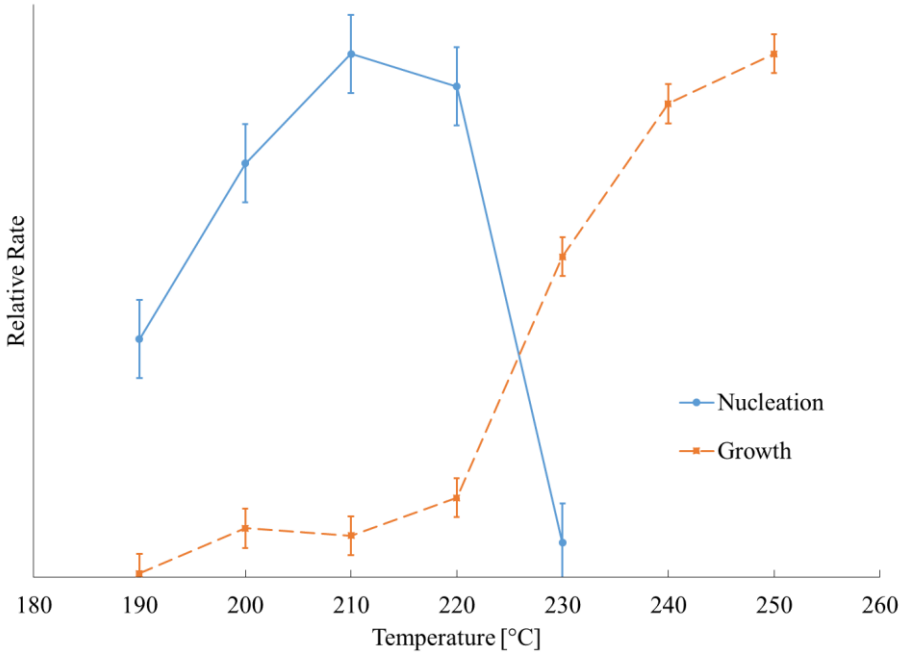

Figure 24 - Nucleation-like and growth-like curves for 40 PbSe (400g; 30 mm; T_Q = 650°C)

These experiments show that changing the melt volume have very little effect on the nucleation rate curves for both the 20 PbSe and 40 PbSe compositions. The melt volume did have a small effect on the growth behavior of the 20 PbSe, but not on the 40 PbSe glass. Additionally, these experiments also show that 20 PbSe nucleation and growth curves are well separated, making it ideal for controlled nucleation and growth. The 40 PbSe glass shows more overlap than the 20 PbSe glass, but still contains regions where nucleation-only and growth-only heat-treatments can be done.

The nucleation-like and growth-like curves for both the 20 PbSe and 40 PbSe small melts (40 g) were used to define the heat-treatment protocols to be used in the subsequent crystallization study

to form the resulting glass-ceramic. The nucleation heat-treatment was chosen to be the maximum nucleation rate where zero growth rate was seen. The nucleation steps for the 20 PbSe and 40 PbSe were chosen to be 220°C and 210°C, respectively. Three growth steps were chosen for each composition for after the nucleation treatment. These temperatures were chosen to represent the highest growth rate and two other temperatures that had positive, non-zero growth rates and no significant nucleation rates. The three growth temperatures were 250°C, 260°C, and 270°C for 20 PbSe and 230°C, 240°C, and 250°C for 40 PbSe.

Quench Rate Experiments

In order to evaluate the relationship between optical homogeneity and quenching conditions, a comparison study between two melts of identical chemistry and melt size was developed where the way the melt was quenched in the ampoule was varied. The goal of these experiments was to show how changing the quenching conditions can improve optical homogeneity during the scale-up. Two 100g 20PbSe glasses were quenched under different conditions to produce fast-cooled and slow-cooled glass samples. As stated in the experimental section (p.29), the quench rates for the fast-cooled and slow-cooled glasses were estimated by recording the amount of time from removal from the furnace to when the chalcogenide glass pulls away from the wall of the silica. It was assumed that the melt was at 650°C when removed from the furnace. The other major assumption was that the glass pulls away from the silica ampoule when the melt passes through the glass transition region, nominally at a viscosity of 10^{12} Pa s. The fast-cooled glass took approximately 3.5 minutes to quench and the glass transition temperature was 209°C as seen below in Figure 26. Similarly, the slow-cooled glass took approximately 9 minutes to quench and the

glass transition temperature was 203°C. These quenching conditions led to an approximately 2°C/min and 0.8°C/min quench rates for the fast-cooled and slow-cooled samples respectively.

Thick samples (thickness, t~ 5 mm) from each sample were fabricated from near the top of the boule as depicted below in Figure 25. These polished samples were used for density, transmission, and refractive index measurements. Because these melts are lab scale, there is a very small distance between the bulk of the melt and the side wall. The glass near the side wall will cool and contract before the inner volume which leads to a convective flow and turbulence in the melt as it cools. While the samples are annealed to allow them to have their internal stress made more uniform, this variation in thermal history leads to density fluctuations in the melt and this worsens as the cooling rate increases. For industry scale melts, the larger vessels used for melting decrease the volume of melt that is close to the wall which should lead to less turbulence for the bulk of the melt which results in a glass with better optical homogeneity.

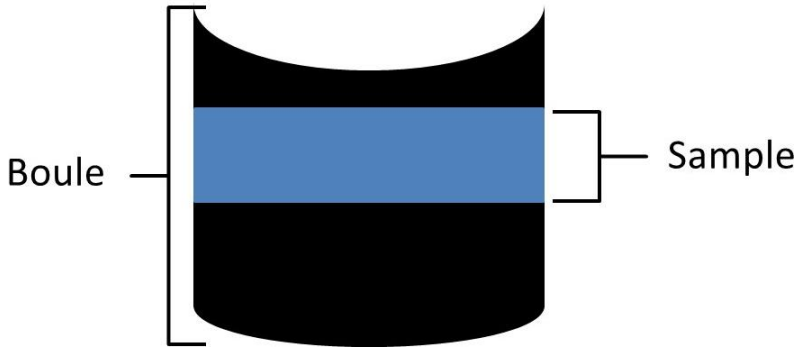

Figure 25 – Cross-sectional diagram of sample location from 100g, 30 mm diameter boule

Figure 26 displays the DSC curves for both the fast-cooled and slow-cooled glasses. The difference in the thermal histories of the slow-cooled and fast-cooled glasses can be seen in their thermal

analysis curves, as they have glass transition temperatures of 203°C and 209°C, respectively. This is outside the instrumental error of +/- 2°C. As stated in the introduction section (p.5), the fast-cooled glass should have a higher T_g than the slow-cooled glass which is supported by this experiment.

As seen below, the slow-cooled glass has crystallization peak temperatures at 304°C and 328°C while the fast-cooled glasses has crystallization peak temperatures at 309°C and 334°C. This suggests that the slow-cooled melt should contain more as-quenched nuclei than the fast-cooled melt because the slower cooling rate allows for more time for crystal nuclei to potentially form. It can be expected that crystallization occurs at lower temperatures in the DSC curve because the pre-existing crystal nuclei can start growing at the beginning of the crystallization temperature range. This increases the rate of crystallization at earlier temperatures thus shifting the crystallization peak to lower temperatures. What is clear from the DSC traces is that the variation in cooling rate does not lead to new peaks or shoulders which would be indicative of other species (nuclei) for potential crystallization due to the rate of quench.

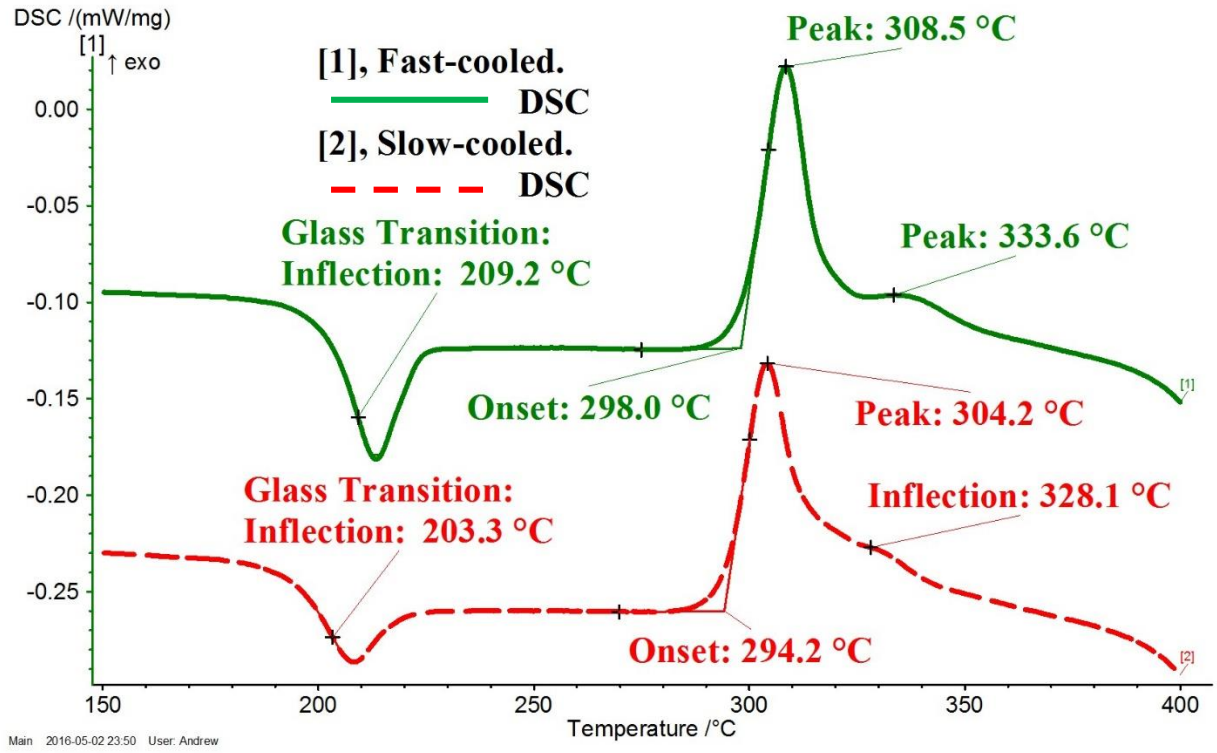

Figure 26 – DSC of the slow-cooled and fast cooled 20 PbSe glasses. Heating rate: 10°C/min

As seen in Figure 1, a fast-cooled glass should have a larger volume than a slow-cooled glass. While this is likely the case in these glasses, the difference in density between these two glasses show relatively little difference between each other. Despite the fact that there is relatively little change in density, the refractive index does show noticeable change. While the fast-cooled glass was expected to have a lower refractive index than the slow-cooled glass, the fast-cooled glass had higher refractive index at both 4.515 µm and 9.294 µm. These glasses both show striations, indications of density fluctuations, as seen in Figure 27. While both samples display these density fluctuations, the fast-cooled glass had more severe striations. Since the index measurements used for these measurements are from a single point on the sample's surface, the presence of these density fluctuations could affect the index measurements.

Table 5 – Refractive index and density measurements of fast-cooled and slow-cooled glasses

	Refractive Index (4.515 μm)		Refractive Index (9.294 μm)		Density [g/cm^3]		Density Sample Size [g]
	Average	Error	Average	Error	Average	STDEV	Average
Fast-cooled	2.8522	0.0005	2.8384	0.0015	4.998	0.005	9.554
Slow-cooled	2.8457	0.0005	2.8312	0.0015	5.007	0.006	8.694

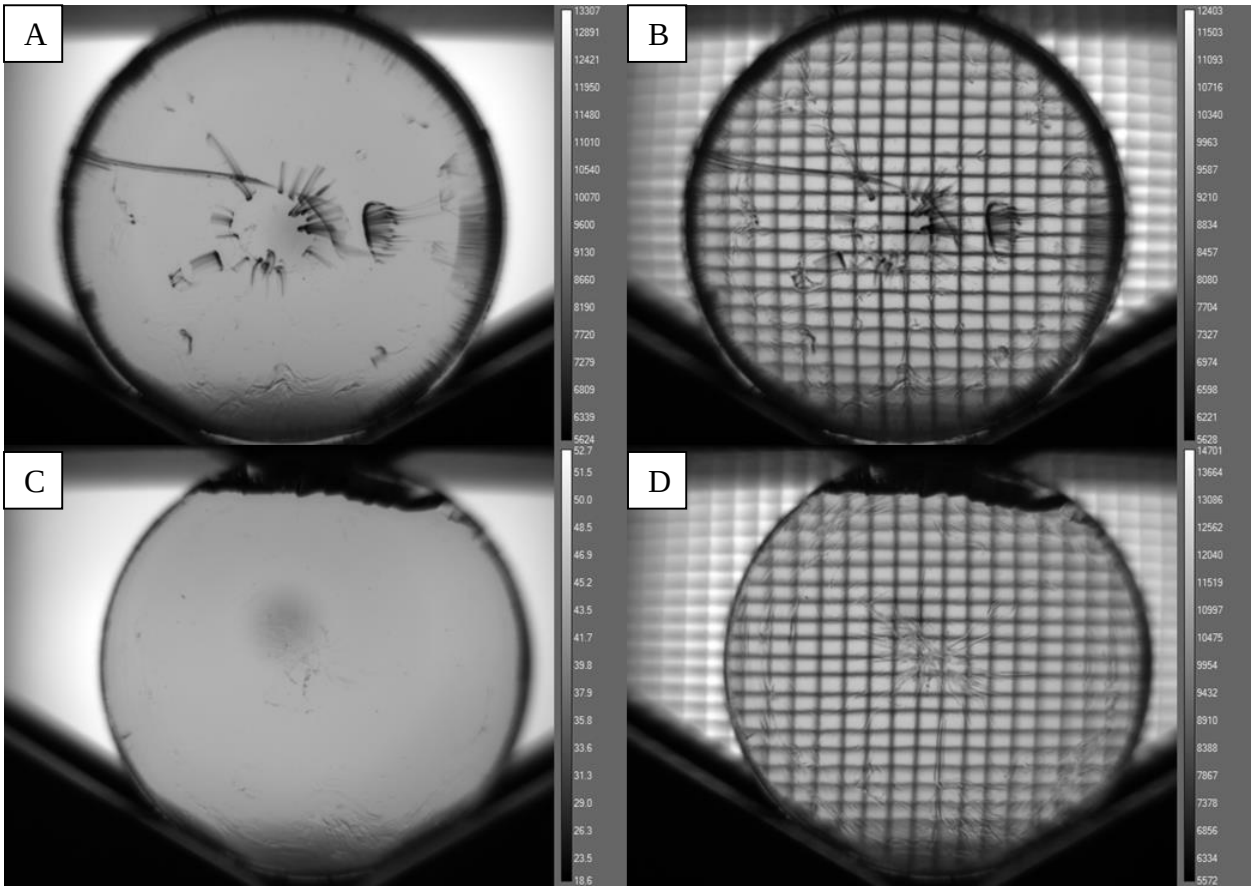

Figure 27 - Images of fast-cooled and slow-cooled glasses taken with FLIR IR camera. Each disc is 30 mm in diameter and the grid is composed of approximately 1.5 x 2 mm squares (A) Fast-cooled without grid (B) Fast-cooled with grid (C) Slow-cooled without grid (D) Slow-cooled with grid

A FLIR infrared camera was used to look for internal defects in the glass samples. In Figure 21 above, the fast-cooled melt (*A* and *B*) shows a major crack running halfway across the sample. This crack runs through the sample from surface-to-surface and occurred during the quench as a result of thermal shock. Additionally, there are very obvious signs of inhomogeneities linked to the contraction during the quench and the turbulence of the melt. The "starburst" pattern seen in the center of the sample and the striae around edge are a result of contraction near the meniscus and ampoule wall, respectively. Other inhomogeneities in the bulk of the melt come from the turbulent, convective flow during the quench which leads to the fluctuations in density. The slow-cooled glass shows the same inhomogeneities, but the severity of the defects are much more subdued due to the slow cooling rate that allowed more relaxation.

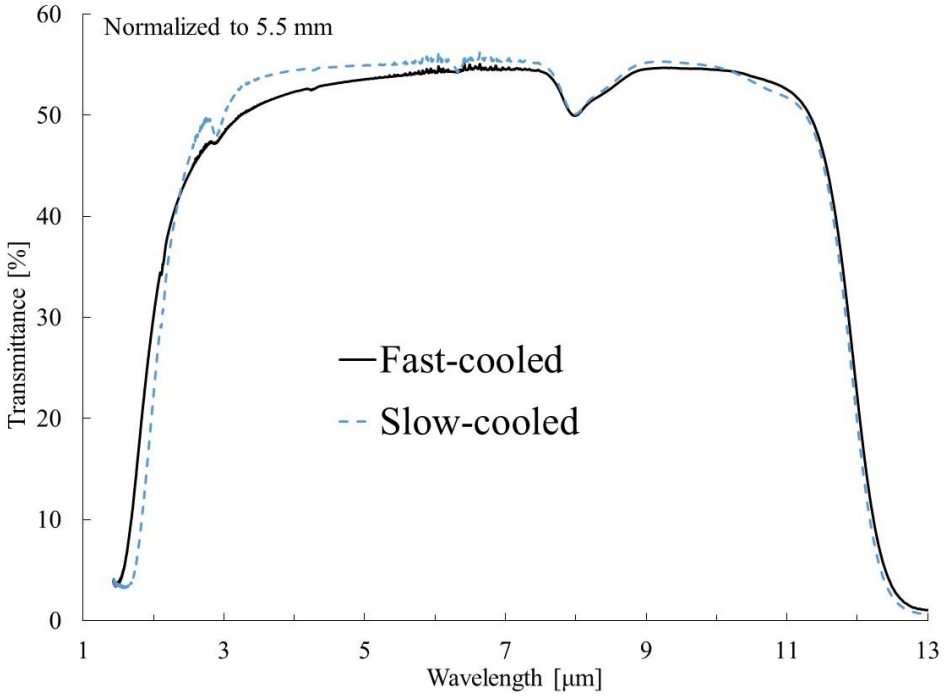

Figure 28 – FTIR spectra of the fast-cooled and slow-cooled glasses. Sample thickness was normalized to 5.5 mm. Not corrected for Fresnel loss

The transmission window for these glasses were measured using FTIR spectroscopy. As seen above in Figure 28, the two glasses show good transmission from 3 to 11 µm despite the striae in the glass samples. These transmission measurements were taken at locations away from the center and edge in order to avoid the most extreme inhomogeneities. The transmission windows for both glasses are very similar. The short-wavelength cutoffs for the fast-cooled and slow-cooled glasses are 3.16 µm and 3.03 µm, respectively. The long-wavelength cutoffs are 11.36 µm for the fast-cooled glass and 11.21 µm for the slow-cooled glass.

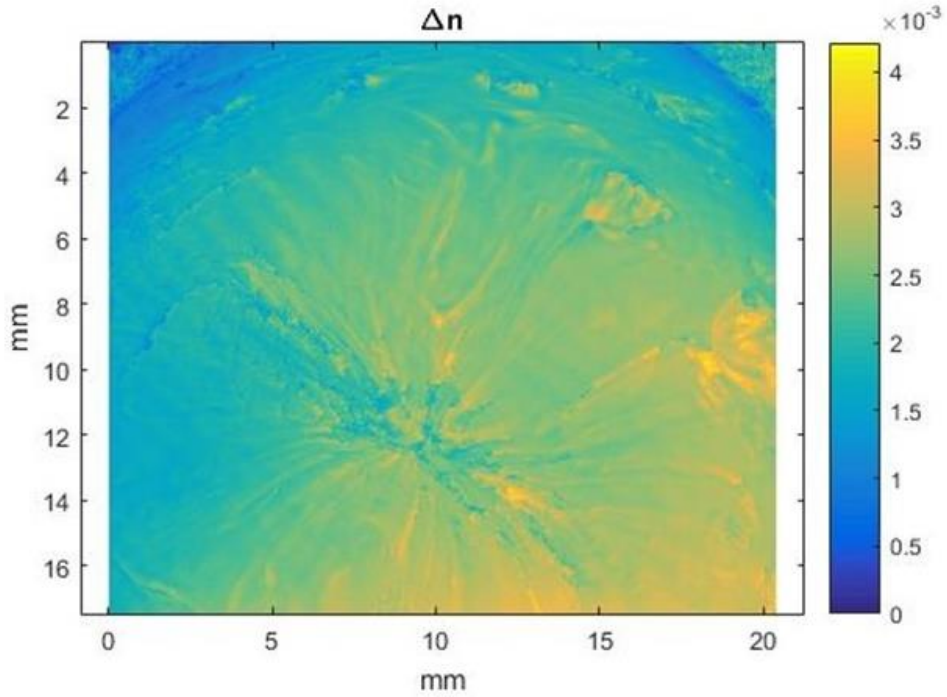

Figure 29 – Index homogeneity map of slow-cooled melt at 4.5905 µm

The index measurements shown in Table 5 were taken at a single point on the glass sample. These index values were taken as surface measurements. The samples were sent to the University of Rochester for absolute index (through-sample measurement) and index homogeneity mapping.

Figure 29 shows the spatial variation in refractive index across a section of the sample as measured by the Mach-Zehnder system at UofR. The striae are clearly present throughout the bulk of the slow-cooled sample. This image provides a much clearer representation of the significant density fluctuations present in the glass. Because the index variations follow the pattern of the striae so closely, it is consistent with these striae being the result of density fluctuations caused by turbulent melt flow during the quench. Like the slow-cooled melt, the fast-cooled melt shows significant striae throughout the bulk of the sample as seen in Figure 30. As mentioned above, the fast-cooled sample showed significantly more visible inhomogeneities in the FLIR images (Figure 27). The presence of these inhomogeneities makes the index measurement and mapping more difficult which likely explains the more muted color in Figure 30 compared to Figure 29.

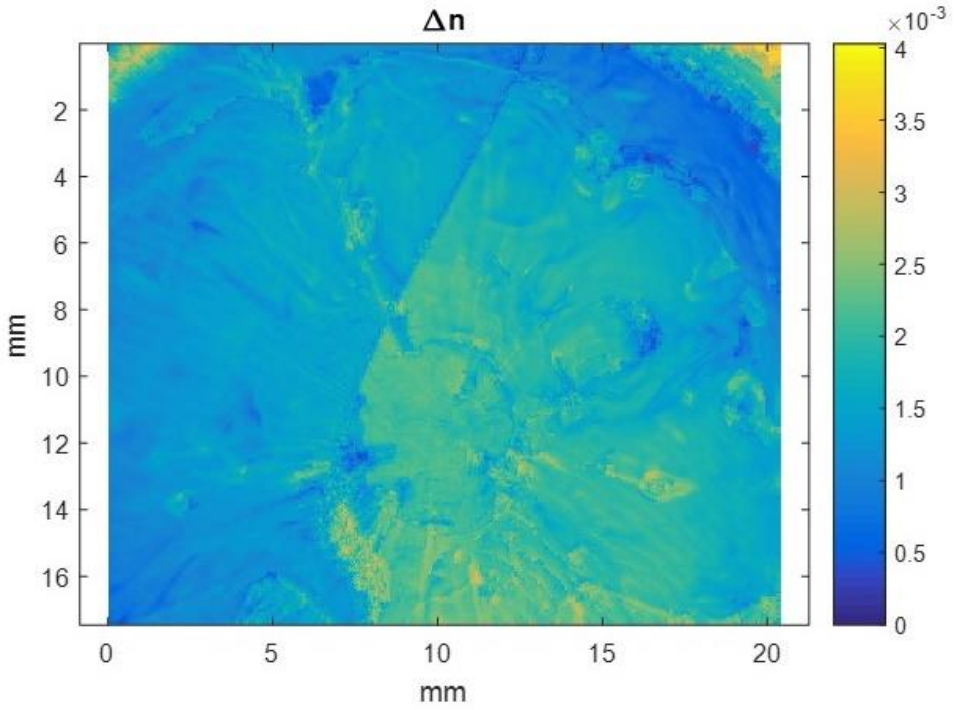

Figure 30 – Index homogeneity map of fast-cooled melt at 4.5905 µm

Absolute refractive index at 4.5905 µm was measured on the Sagnac system at UofR. The striae in both samples made the measurements extremely difficult to make. Eleven measurements were made on the slow-cooled sample. Each measurement was performed at a different angle while the deviation of the beam passing through the sample was measured which is then used to calculate the refractive index. The refractive index at 4.5905 µm was found to be 2.88(476) ± 0.03(215). Absolute index measurements were also attempted on the fast-cooled sample, but the internal striae made the measurements impossible.

The quench rate experiments show how the melting and quench protocols for lab-scale melts affect the properties of the glass samples. The quench rate affects the refractive index, density, and T_g in ways that were consistent with behavior predicted in Figure 1.[1] The quench methods also have a significant effect on the presence of striae in the melt. The slow-cooled melt showed less extreme striae because the melt had more time to relax during cooling. This led to a more optical homogeneous glass that allowed some measurements to be performed at University of Rochester. The fast-cooled glass showed extremely turbulent striae that prevented full characterization at University of Rochester.

Commercial Scale-Up

In an effort to show commercial viability, the 20 PbSe composition was scaled up to larger sizes with a partnership with Amorphous Materials Inc. (AMI). The lab-scale melts made at UCF were between 40 and 150 g. These glasses were in the form of 10 – 30 mm diameter boules. Figure 31 shows that these melts have minor differences in the primary T_g, T_x, and T_p values, but show the

same crystallization features. The onset of crystallization, T_x, for the small and large melts were 294°C and 292°C, respectively. The 150 g melt showed crystallization peaks, T_p, at 301°C, 321°C, and 326°C. The crystallization peaks for these same crystal species for 40 g melt were seen at 303°C, 321°C, and 327°C. The main difference between the large and small UCF melts is the presence of two distinct glass transition temperatures in the large melt at 207°C and 217°C while the small melt only showed one T_g at 203°C. The presence of two glass transition temperatures is expected for glasses that show phase separation like the 20 PbSe composition. The second T_g in the 40 g is obscured in the DSC signal because the volume fraction of the secondary phase was too small to be detected separately from the primary T_g.

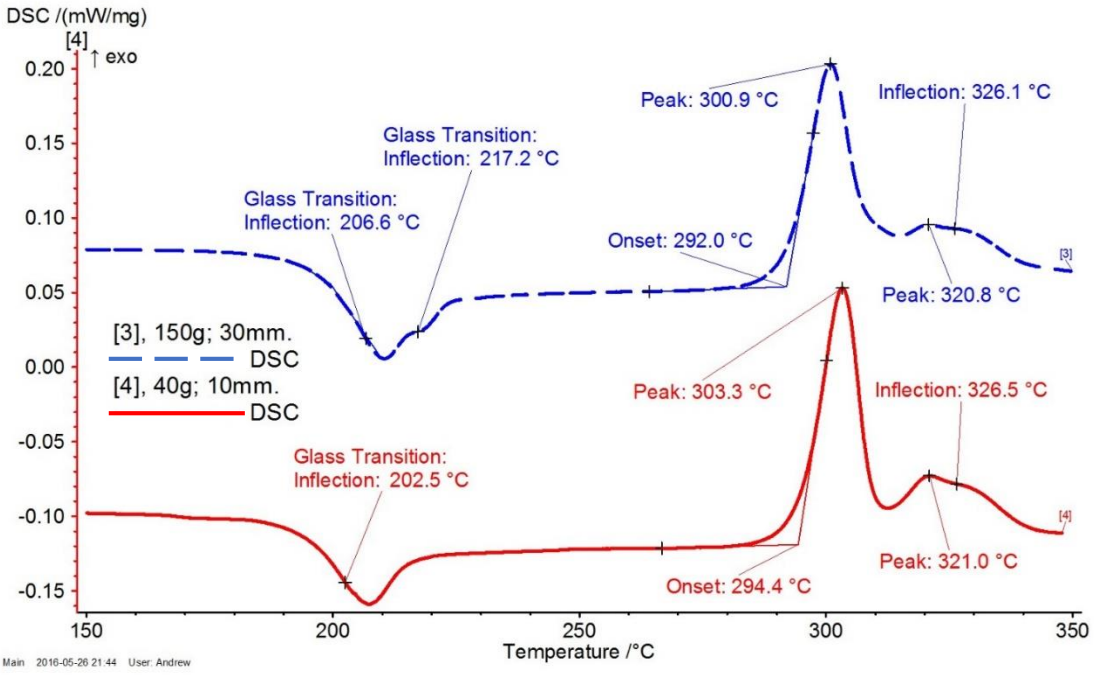

Figure 31 - DSC curves of 20 PbSe glasses melted at UCF (T_Q = 650°C). Heating rate: 10°C/min

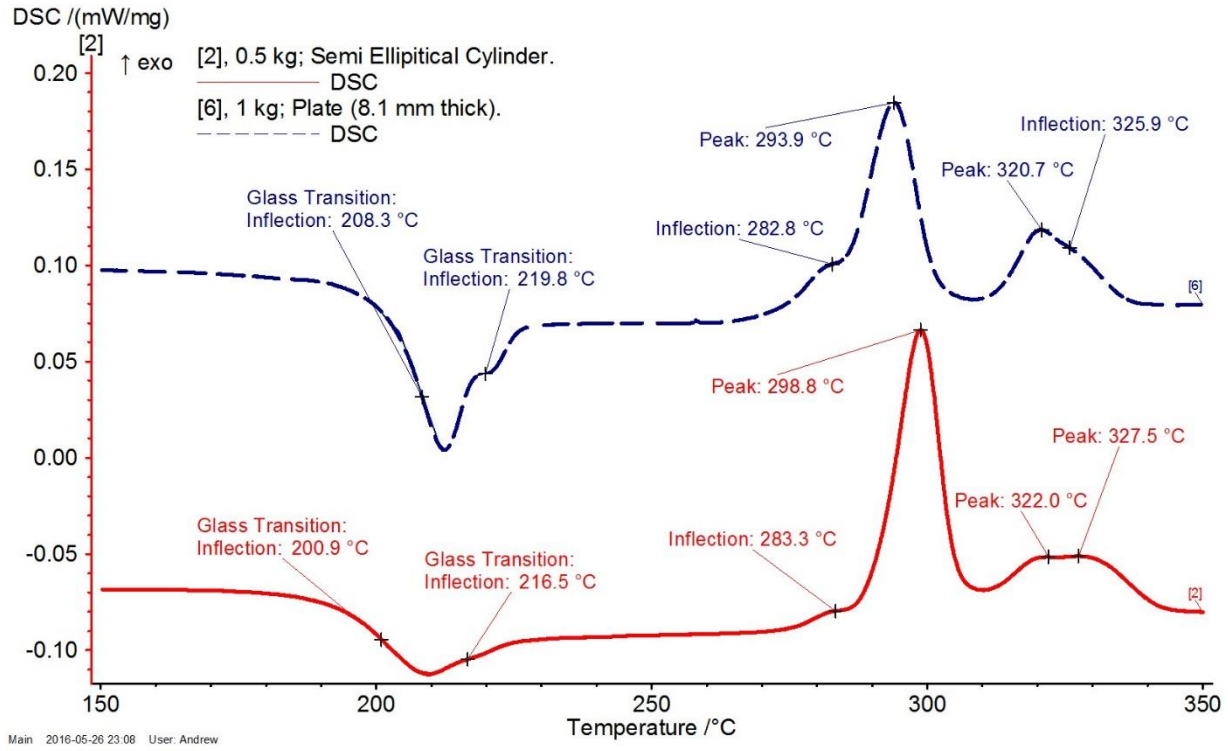

Figure 32 - DSC curves of 20 PbSe glasses melted at AMI. Heating rate: 10°C/min

The 20 PbSe glasses melted at AMI ranged from 0.5 kg to 1.5 kg. These batches were either in the form of semi elliptical cylinders (major radius ~ 27 mm; minor radius ~ 10 mm) or ~200 mm diameter plates (8.1 - 12.15 mm thick). The DSC curves for the glasses melted at AMI are shown above Figure 32. The 0.5 kg melt showed two glass transition temperatures at 201°C and 217°C. The 0.5 kg glass also shows four crystallization features at 283°C, 299°C, 322°C and 328°C. The 1 kg plate showed two glass transition temperatures at 208°C and 220°C. Like the 0.5 kg melt, the 1 kg melt showed four crystallization features at 283°C, 294°C, 321°C and 326°C. The AMI glasses show the three crystallization features seen in the UCF melts. The T_p of the two higher temperature crystallization features are at the same temperatures. The main crystallization peak in

the 1 kg plate was found to be about 10°C less than the UCF melts. This is consistent with an increased amount of as-quenched nuclei of that crystal phase present in the base glass. This is expected because the AMI melts were cooled at a slower rate. The main difference between the AMI and UCF melts is the additional crystallization feature at approximately 283°C. Since the crystallization feature is seen in all of the AMI melts and none of the UCF melts, it is likely the result of the melt and quench protocol used at AMI versus UCF.

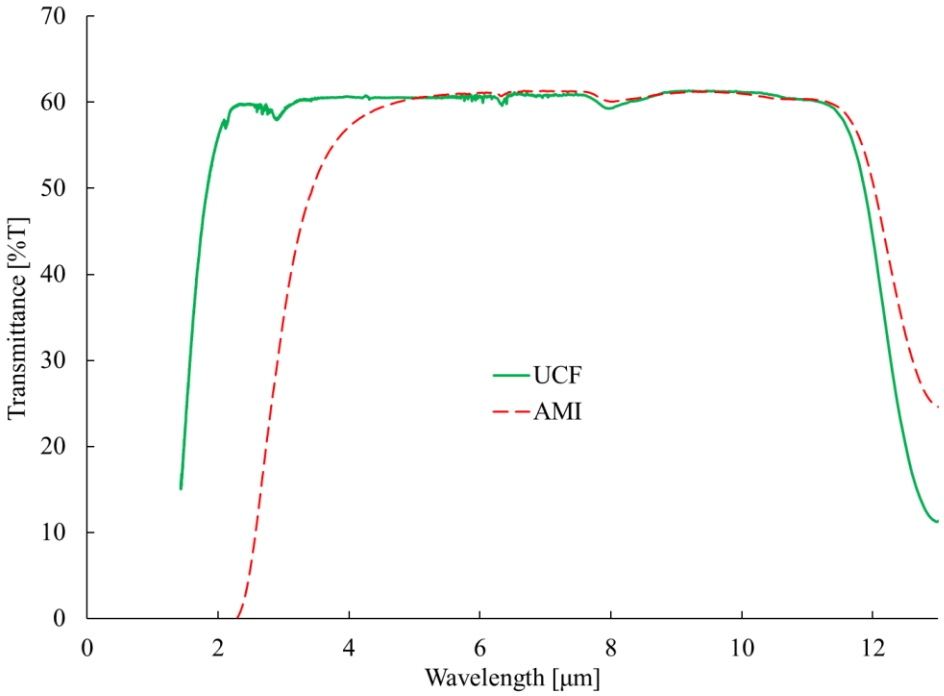

Figure 33 - Transmission window for 20 PbSe UCF (40 g; 10 mm; T_Q = 650°C) and AMI melts

Figure 33 shows transmission spectra of the 20 PbSe melts from UCF and AMI. These base glasses show much different short wavelength cutoffs. The UCF melt was found to maintain high transmission from 1.993 µm to 11.705 µm. The transmission window of the AMI melt was found to be from 3.778 µm to 11.830 µm. The transmission window of the base AMI glass showed

unacceptable losses for the desired application which needs a transmission window from 3 µm to 5 µm. Further heat-treatment, to increase the refractive index will only make the cutoff position worse. The likely cause for this higher cutoff wavelength is the droplet size in the as-quenched glass. Figure 34 shows TEM images of both the UCF and AMI melts. The Pb-rich droplets in the AMI glass (200 to 340 nm) were found to be over twice as big as those in the UCF melt (100 to 130 nm). The larger droplets cause the cutoff to shift to higher wavelengths due to diffuse scattering.

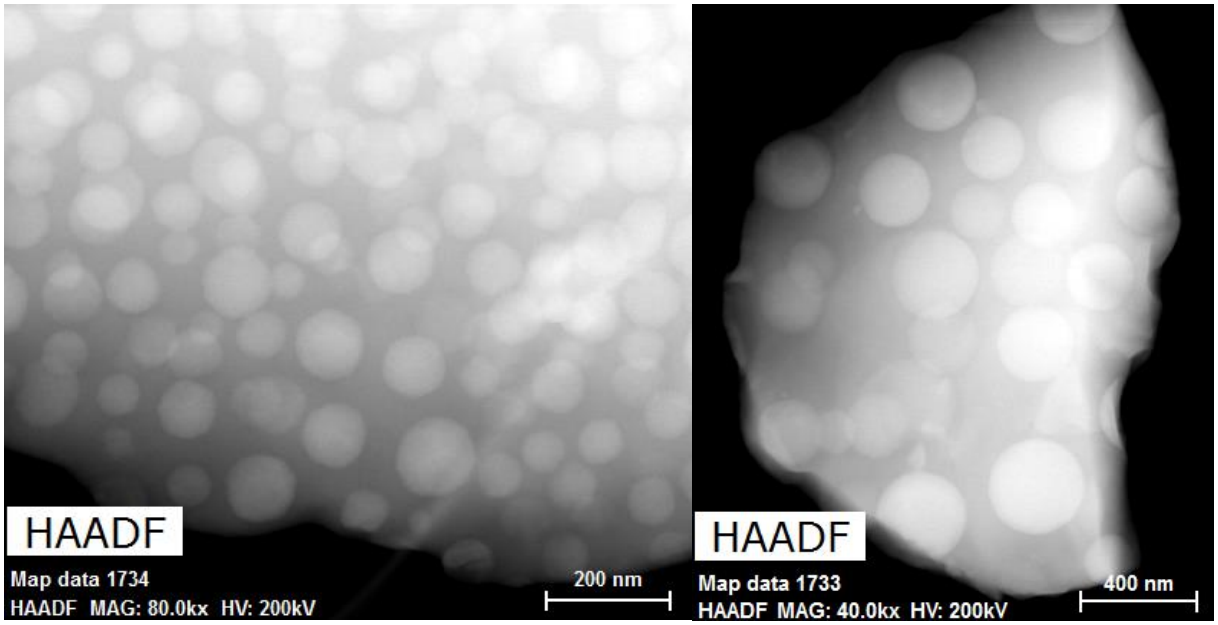

Figure 34 – Dark-field TEM images of 20 PbSe melts from UCF melt 100 – 130 nm droplets (left) and AMI melt with 200 to 340 nm (right)

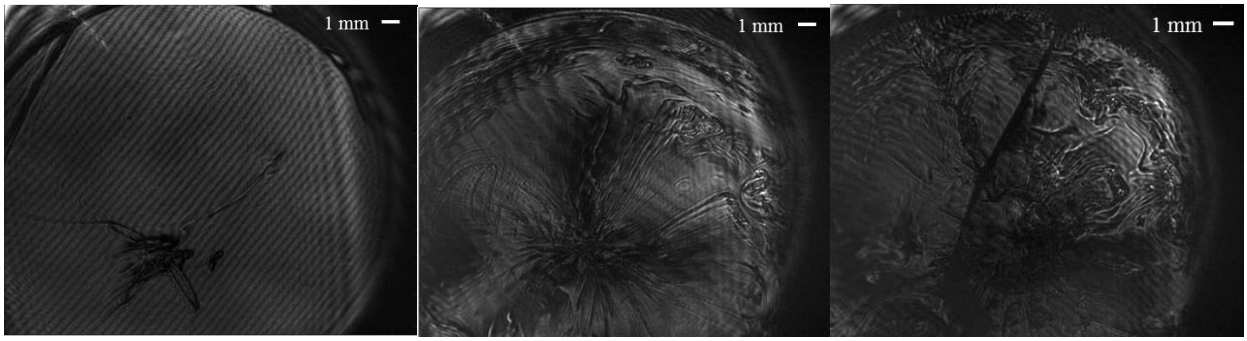

Figure 35 – IR image of 20 PbSe melts. (A) 1 kg commercially polished AMI melt (B) Slow-cooled UCF melt (100g) (C) Fast-cooled UCF melt (100g)

As previously mentioned, the larger vessels and milder quenching conditions of the commercial glasses allows for more optical homogeneity. This is most evident in Figure 35 which shows IR images of the commercial melt, the slow-cooled melt, and the fast-cooled melt. The AMI glass (A) shows one major defect, but almost no internal striae as indicated by the uniform fringes seen across the sample. The gentle quench method and large vessel size greatly reduces the turbulent flow of the melt during quench compared to the lab-scale melts done at UCF. The striae caused by turbulence can clearly be seen in the images for the slow-cooled (B) and fast-cooled (C) glasses. The result of the commercial quenching yields a much more uniform index map as seen in Figure 36 for the 1 kg melt. This index map shows extremely uniform index except around the major defects.

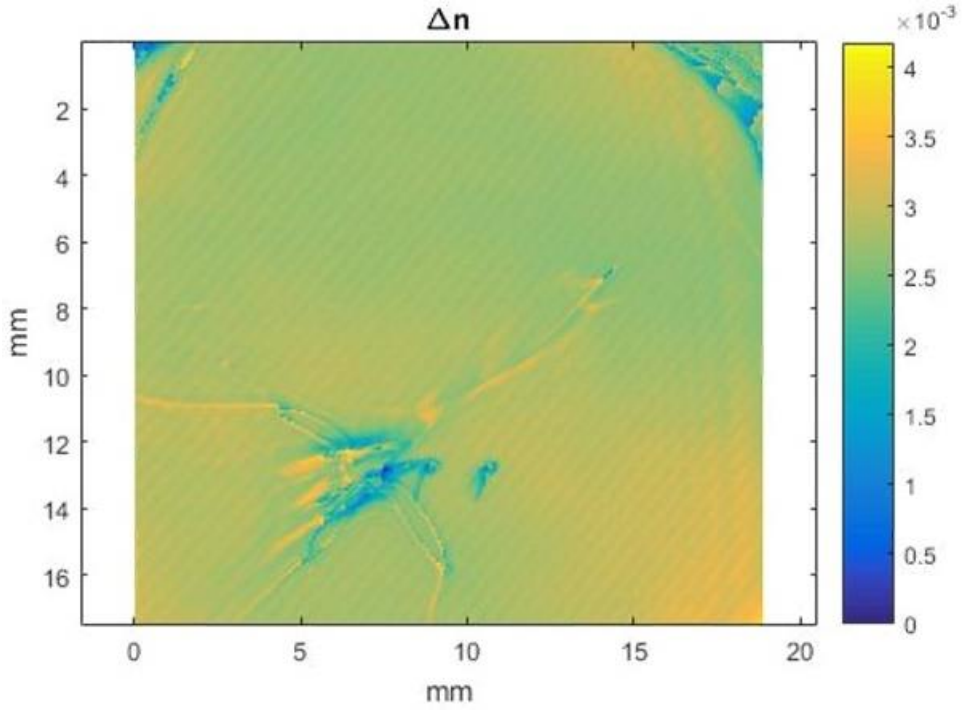

Figure 36 – Index homogeneity map of 1 kg batch AMI glass

Scale-up efforts for the 20 PbSe glasses with the commercial partner, AMI, have shown good optical homogeneity and the ability to increase the size of the melt while maintaining a non-crystalline structure throughout the material. While there are some promising initial findings from the scale-up, the current transmission window of the base glass does not provide adequate transmission for the application. The melting and quenching protocol used by AMI has yielded an additional crystal phase that affects the crystallization behavior of the other crystals.

Glass-Ceramic Properties

Based on the nucleation-like and growth-like curves seen in Figure 21 and Figure 23, heat-treatment protocols were established for both the 20 PbSe and 40 PbSe glasses. Using the heat-

treatment temperatures defined based on the nucleation and growth curves, the nucleation step for each glass was chosen to be at the maximum nucleation rate seen in the figures. The nucleation time was chosen to be 2 hours in order to thoroughly saturate the nucleation sites in the glass. The nucleation steps for the 20 PbSe and 40 PbSe glasses were 220°C for 2 hours and 210°C for 2 hours, respectively. The growth temperatures were chosen at temperatures where there was near zero nucleation and non-zero growth according to the nucleation-like and growth-like curves. Additionally, the growth times were chosen to ensure a maximum of crystal growth could be compared and defined to be 30 minutes. In theory, a smaller Δn could be realized at shorter growth times (yielding parts of better optical transmission due to less scattering) but this protocol was chosen for consistency.

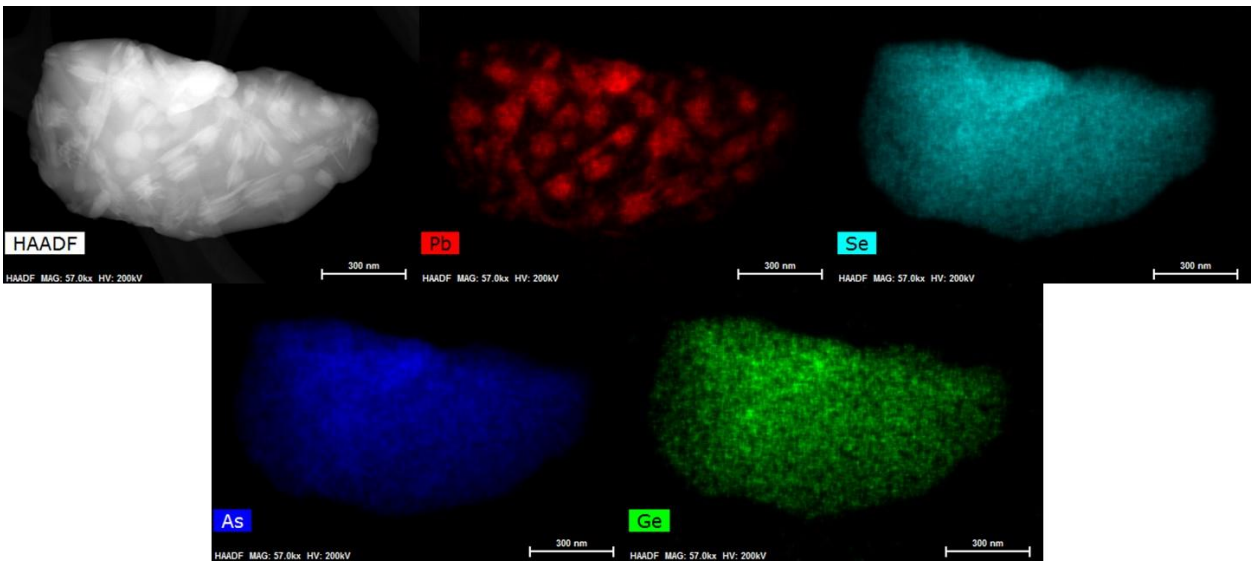

Figure 37 – Dark field TEM image and XEDS mapping of crystallites in 20 PbSe glass heat-treated at 220°C for 2 hours + 270°C for 30 minutes. Scale bars are 300 nm (40 g; 10 mm; T_Q=650°C)

Figure 37 shows the 20 PbSe glass after it was heat-treated at 220°C for 2 hours followed by a growth treatment at 270°C for 30 minutes. When compared to the TEM images shown in Figure 12, the secondary phase is no longer spherical, amorphous droplets. Since the same TEM protocol was used for these samples as the base glass samples the change seen was caused by the heat-treatment which caused crystals to form within the Pb-rich droplets. This glass-ceramic maintains the Pb segregation with Pb-rich crystals in an amorphous Pb-deficient matrix, as seen in the XEDS mapping above. SAED was performed on the crystalline phase to confirm the presence of crystallization. Figure 38 shows the analysis of the diffraction pattern with possible crystal assignments including a monoclinic As_2Se_3 crystal phase and a cubic $Ge_{0.1}Pb_{0.9}Se_{1.0}$ crystal. This pattern clearly shows that there are multiple crystal phases present in the glass sample. Since these heat-treatments targeted the nucleation and growth of the first crystal peak seen in the DSC, a majority of the crystals seen in the TEM images are likely this crystal phase.

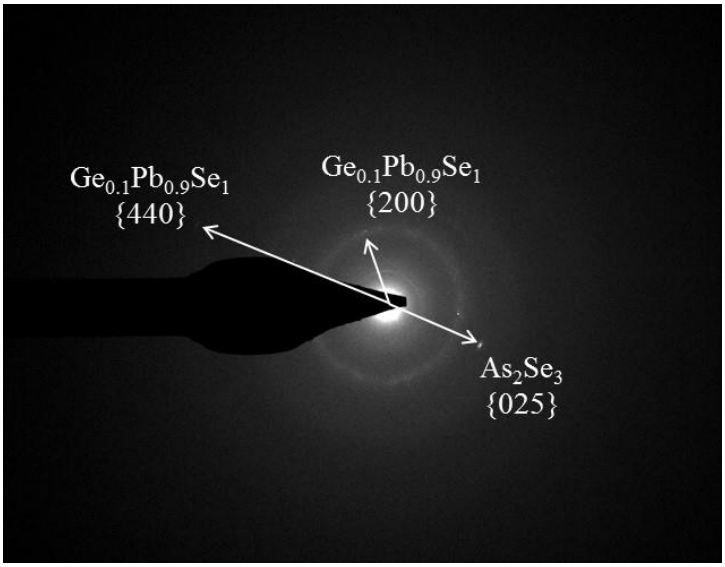

Figure 38 - SAED of crystalline phase of 20 PbSe glass heat-treated at 220°C for 2 hours + 270°C for 30 minutes

Table 6 – Base, nucleated, and grown properties of 20 PbSe glass with the average standard deviation for each measurement

	Base	Nucleated 220°C-2hrs	Grown 250°C-30min	Grown 260°C-30min	Grown 270°C-30min
Density [g/cm^3] {± 0.015}	4.990	4.968	4.955	4.974	4.996
Hardness [kg_f/mm^2] {± 3.1}	161.4	156.3	156.9	165.1	165.3
Refractive Index at 4.515 µm {± 0.0005}	2.8440	2.8309	2.8317	2.8618	2.8723

Table 6 shows the density, hardness, and refractive index data for the 20 PbSe glass as it progresses through the nucleation and growth heat-treatments. All three of these properties were expected to increase after crystallization. The change in all three values were expected to increase with increasing growth temperature. The density values show very little change over the course of the heat-treatments. This is likely due to the fact that the Archimedes method used to measure density measures the apparent density of the glass. Since the crystallization is occurring in the Pb-rich droplets, the crystallization-induced density change would be confined to the droplets and the immediate surrounding area. Because of the small scale density changes it is likely that any density changes will not be detected by this measurement.

Like the density, the Vickers hardness measurements showed very little increase with the heat-treatments. The introduction of crystals should increase the overall hardness of the material because crystals are known to be harder than glass due to their stronger, more uniform bonds.

Additionally, hardness increases in this system as PbSe content increases. In the case of the 20 PbSe composition, the heat treatments are transforming a soft glass matrix with hard glass droplets to a soft glass matrix with hard, dispersed crystals. Because the small volume fraction hard phase is transforming to a harder phase while the soft phase remains unchanged, it makes sense that there would be a relatively small change in hardness.

While the density and hardness values for the 20 PbSe show very little change with the heat-treatments, the index and transmission windows were affected by the heat-treatments. As seen in Table 6, the refractive index at 4.515 μm decreases from 2.8440 to 2.8309 after the nucleation heat-treatment. The subsequent growth heat-treatments at 250°C, 260°C, and 270°C increase the refractive index to 2.8317, 2.8618, and 2.8723, respectively. The initial decrease in index is likely caused by small-scale crystallization that changes the composition of the residual glass during the heat-treatment. The subsequent increase in index is caused by the growth of these crystals with higher refractive index to the point where their volume fraction becomes significant.

While these heat-treatments changed the refractive index, they also caused the short wavelength cutoff to shift to higher wavelengths as seen in Figure 39. The short wavelength cutoff (90% of max transmission) of the 20 PbSe base glass was found to be 1.993 μm. The nucleation step slightly shifted the cutoff to 2.033 μm. The subsequent growth heat-treatments noticeably shift the cutoff to higher wavelengths. The 250°C, 260°C and 270°C heat-treatments shifted the cutoffs to 2.280 μm, 4.956 μm, and 6.326 μm, respectively. Since the target transmission window for the application is 3-5 μm, the shifts seen in the 260°C and 270°C growth heat-treatments were too

much for the application. As previously mentioned, the shift in the short wavelength cutoff is caused by increased scattering due to the size of secondary phases (droplets/crystals) in the matrix. While these growth temperatures show good increases in index, their loss in transmission is unacceptable for the application. Adjustments to the nucleation and growth protocols may be able to produce a higher number density of crystals of a smaller size. This could lead to an acceptable change in index and transmission window.

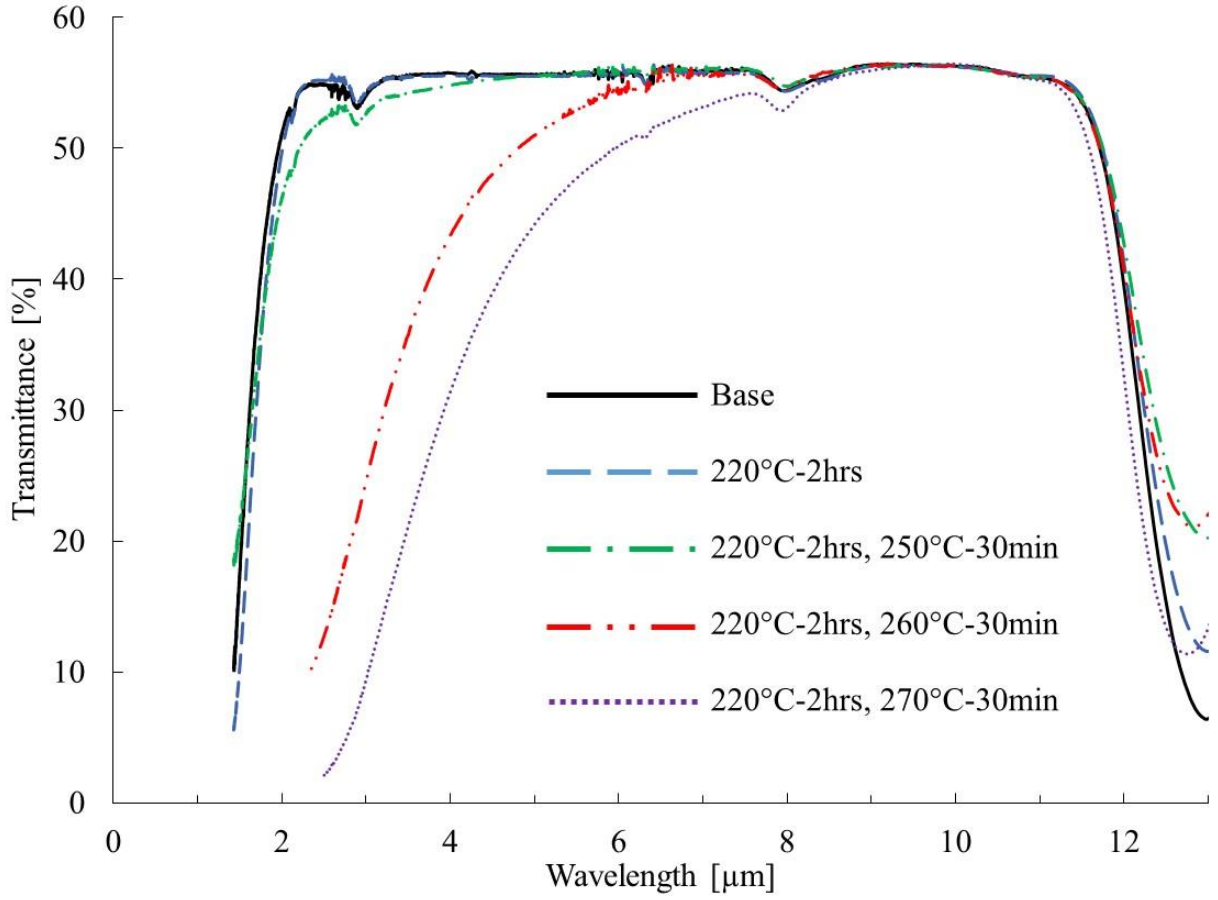

Figure 39 – FTIR transmission spectra of base and heat-treated 20 PbSe (40 g; 10 mm; T_Q=650°C). Sample thickness normalized to 2 mm. Not corrected for Fresnel Loss

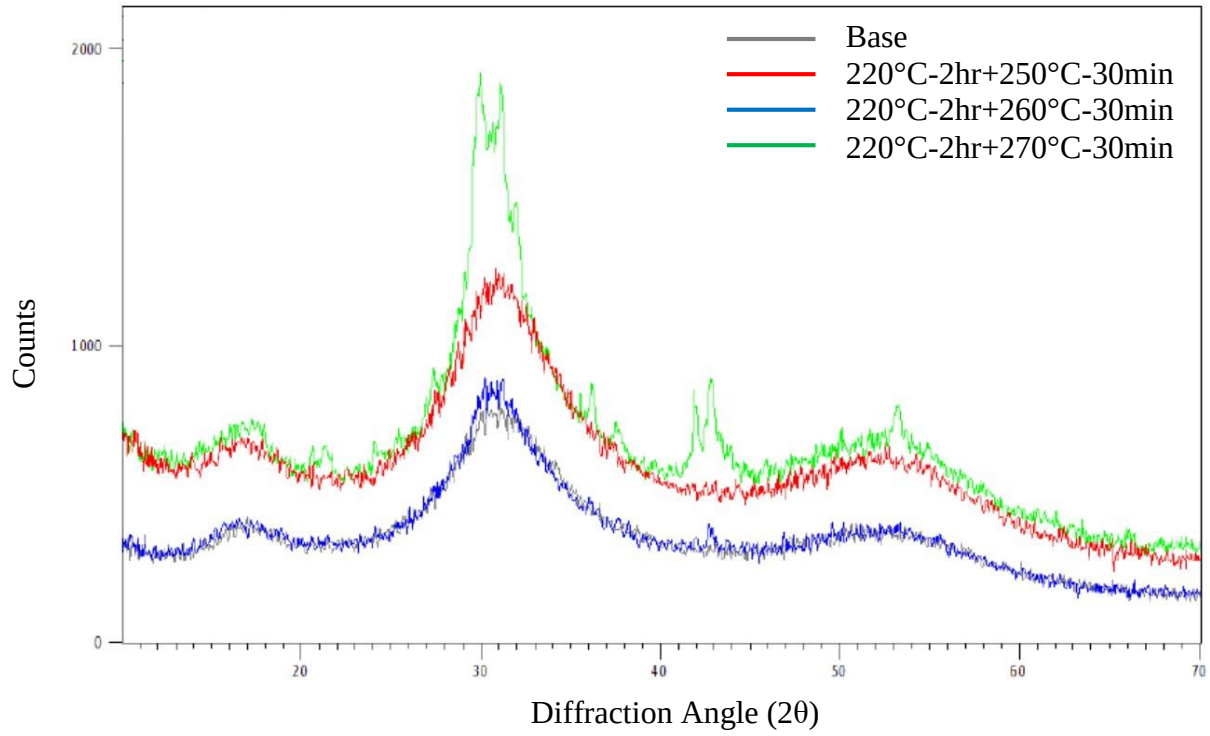

Figure 40 - XRD of base and heat-treated 20 PbSe glass powder (40 g; 10 mm; T_Q = 650°C)

XRD was performed on glass powder from all three of the nucleated (210°C-2 hrs) and grown heat-treatments in order to identify the precipitating crystal phase(s) and to see at what temperature detectable crystallization occurs. Figure 40 shows the overlay of the base glass, nucleation + 250°C-30 min, nucleation + 260°C-30 min, and nucleation + 270°C-30 min samples. The base glass and the nucleation + 250°C-30 min samples show the same amorphous curves and no sharp peaks. The nucleation + 260°C-30 min looks very similar to the base curve, but has grown one sharp peak at approximately 43°. The sample that underwent the higher growth treatment at 270°C appears much more crystallized than the previous samples, but still shows an amorphous baseline. An attempt was made to identify the crystal peaks for the 270°C grown sample, seen below in Figure 41. The same crystal patterns identified in the SAED measurements, above, were applied

to this XRD pattern. The remaining peaks were fitted with the best fit crystal peaks from the database that contained As, Ge, Se, and Pb. None of the reference patterns in the database match the crystal peaks perfectly, but do match some of the peaks. It is likely that there are additional crystals present have similar structures to these, but with additional atoms in the crystal lattice causing distortions. The true crystal species are likely multicomponent compounds that have no standard reference patterns in the database.

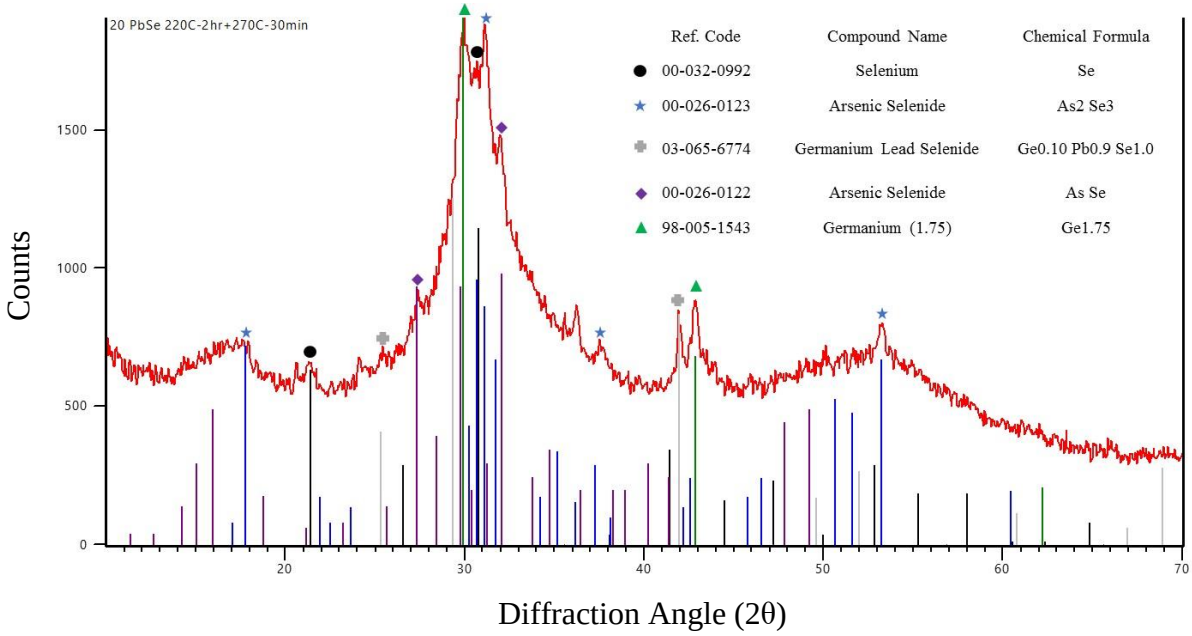

Figure 41 - XRD of heat-treated 20 PbSe glass powder (220°C-2hr+270°C-30min) with peak assignments.

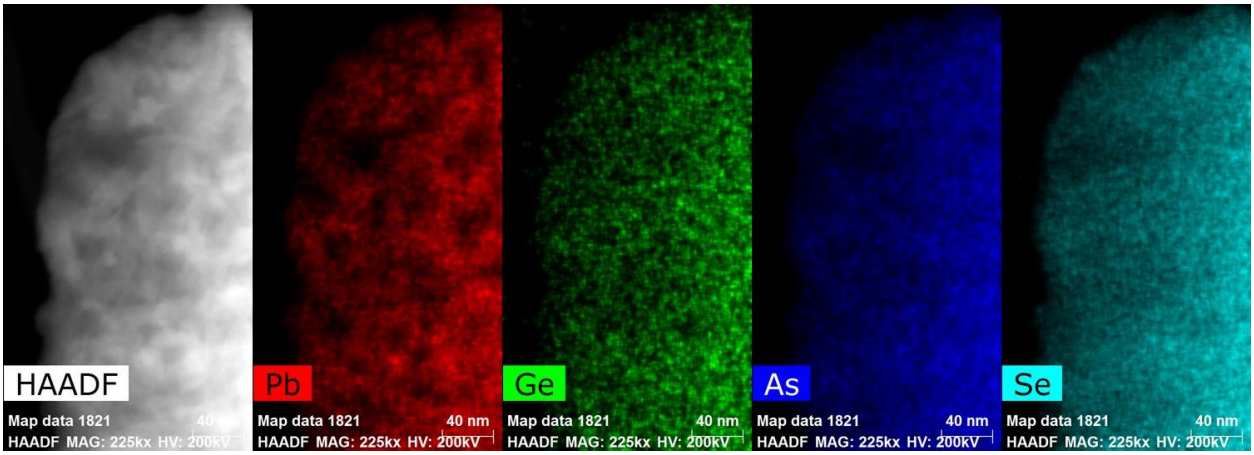

Figure 42 – Dark field TEM image and XEDS mapping of 40 PbSe glass heat-treated at 210°C for 2 hours + 250°C for 30 minutes (40 g; 10 mm; T_Q = 650°C)

Figure 42 shows the 40 PbSe glass after it was heat-treated at 210°C for 2 hours followed by a growth treatment at 250°C for 30 minutes. When compared to the TEM images shown in Figure 14, the matrix phase has completely crystallized. Since the TEM protocols were the same as the base sample this crystallization is believed to be caused by the heat-treatment and not the e^- beam. This glass-ceramic maintains the Pb segregation with Pb-rich crystals in the matrix section with secondary Pb-deficient droplets, as seen in the XEDS mapping above. SAED was performed on the crystalline phase to confirm the presence of crystallization. Figure 43 shows the analysis of the diffraction pattern with possible crystal assignments including a monoclinic As_2Se_3 crystal phase, a cubic PbSe crystal, and a hexagonal Se crystal phase. This pattern clearly shows that there are multiple crystal phases present in the glass sample.

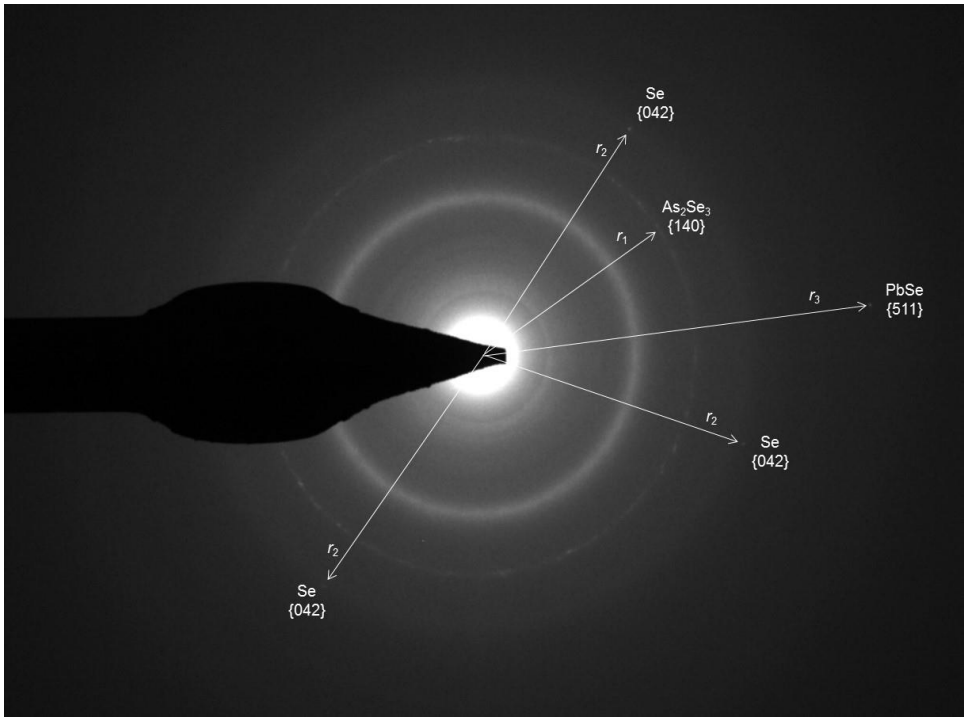

Figure 43 – SAED of crystalline phase of 40 PbSe glass heat-treated at 210°C for 2 hours + 250°C for 30 minutes

Table 7 - Base, nucleated, and grown properties of 40 PbSe glass

	Base	Nucleated 210°C-2hrs	Grown 230°C-30min	Grown 240°C-30min	Grown 250°C-30min
Density [g/cm^3] {± 0.017}	5.543	5.530	5.536	5.610	5.631
Hardness [kg$_f$/mm^2] {± 3.4}	167.5	169.5	179.3	185.8	191.1
Refractive Index at 4.515 µm {± 0.0005}	3.0473	3.0374	3.0788	3.1552	3.1663

Table 7 shows the density, hardness, and refractive index data for the 40 PbSe glass as it progresses through the nucleation and growth heat-treatments. There is very little change in the density after nucleation where the density goes from 5.543 g/cm^3 to 5.530 g/cm^3. The density remains close to this value after the 230°C for 30 minutes with a value of 5.536 g/cm^3. The high heat-treatments at 240°C and 250°C show noticeable increases in density to 5.610 g/cm^3 and 5.631 g/cm^3. Compared to the 20 PbSe, there is a noticeable increase in the density at the higher heat-treatments. This is believed to be due to where the crystallization is occurring in the glass. In the 20 PbSe composition, crystallization did not significantly change the density. The crystallization in the 40 PbSe showed significant changes because the crystallization occurs in the glass matrix. Because the crystallization occurred in the majority phase, it had a more direct effect on the apparent density of the glass which can be measured with the Archimedes method.

While the 20 PbSe glass showed very little change in hardness with heat-treatment, the 40 PbSe glass showed significant increases in hardness after growth heat-treatments. The nucleation heat-treatment did not change the hardness significantly, going from 168 kg_f/mm^2 to 170 kg_f/mm^2 which is within the standard deviation of the measurement. The subsequent growth heat-treatments show a significant rise in hardness to 179 kg_f/mm^2, 186 kg_f/mm^2, and 191 kg_f/mm^2 for the 230°C, 240°C, and 250°C heat-treatments respectively. As previously stated, the introduction of crystals will increase the hardness of the material because the crystals are known to be harder than crystals. Because the crystallization occurred in the majority phase, the large volume fraction of crystals (harder phase) significantly affected the overall hardness of the material.

Like the 20 PbSe glass, the 40 PbSe glass showed an initial decrease in refractive index after nucleation, as seen in Table 7. The refractive index at 4.515 μm decreases from 3.0473to 3.0374 after the nucleation heat-treatment. The subsequent growth heat-treatments at 230°C, 240°C, and 250°C increase the refractive index to 3.0788, 3.1552, and 3.1663, respectively. The maximum change in index between base and heat-treated was Δn = 0.119. This Δn is greater than what was seen in the 20 PbSe glass which showed a maximum Δn of 0.0283. The larger Δn is likely due to the higher volume fraction of crystals due to the fact that crystallization occurs in the Pb-rich majority phase (matrix). Crystals cause local increases in refractive index by introducing a higher refractive index phase or by increasing the local density. As seen in Table 7, the increase in refractive index correlates with the density increase.

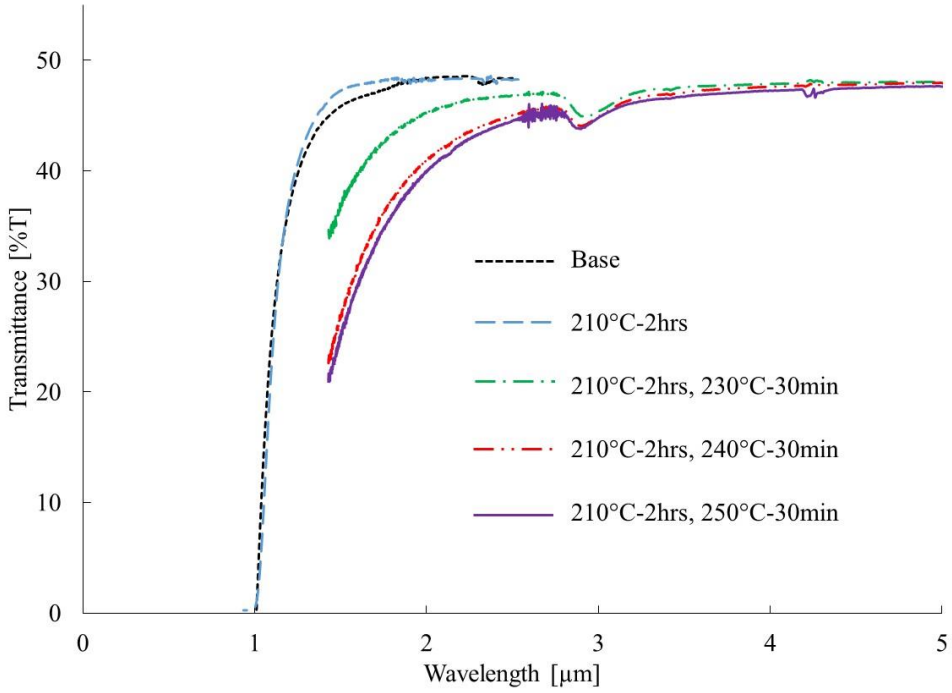

Figure 44 – FTIR and UV-Vis-NIR transmission spectra of base and heat-treated 40 PbSe (40 g; 10 mm; T_Q = 650°C) Sample thickness normalized to 2 mm. Not corrected for Fresnel loss.

The large refractive index change after crystallization seen in the 40 PbSe glasses is desirable for the target application. It is also important to maintain transmission from 3 µm to 5 µm while increasing the refractive index which the 20 PbSe failed to do. The heat-treatments of the 40 PbSe glass also caused the short wavelength cutoff to shift to higher wavelengths, as seen in Figure 44. The short wavelength cutoff (90% of max transmission) of the 40 PbSe base glass was found to be 1.319 µm. The nucleation step slightly shifted the cutoff to 1.285 µm. The subsequent growth heat-treatments noticeably shift the cutoff to higher wavelengths. The 230°C, 240°C and 250°C heat-treatments shifted the cutoffs to 1.911 µm, 2.176 µm, and 2.318 µm, respectively. As stated before, the target transmission window for the application is 3-5 µm and all of the post-heat-treated glasses maintain their transmission in this window.

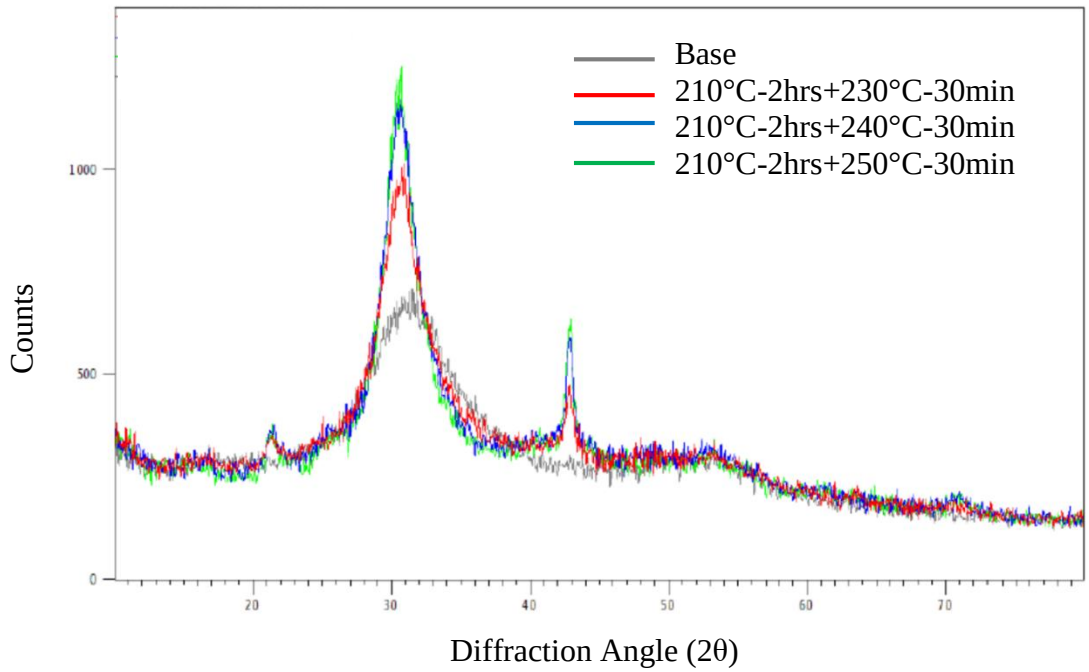

Figure 45 – XRD of base and heat-treated 40 PbSe glass powder (40 g; 10 mm; T_Q = 650°C)

XRD was performed on glass powder from all three of the nucleated (220°C-2 hrs) and grown heat-treatments. Figure 45 shows the overlay of the base glass, nucleation + 230°C-30 min, nucleation + 240°C-30 min, and nucleation + 250°C-30 min samples. While the base glass shows no signs of crystallization, even the lowest heat-treatment shows sharp peaks. The nucleation + 230°C-30 min, nucleation + 240°C-30 min, and nucleation + 250°C-30 min samples all show three sharp peaks at approximately 22°, 31°, and 43°. As the growth treatment increases in temperature, the second two crystal peaks become narrower and more intense. An attempt was made to identify the crystal peaks for the 250°C grown sample, seen below in Figure 46. The same crystal patterns identified in the SAED measurements were applied to this XRD pattern. These patterns do not fit the crystal peaks perfectly, but there are some matching peaks. Based on the XRD and SAED peak identification analysis, these are the main crystals present after heat-treatment or the true crystal species have similar structures to these, but with additional atoms in the crystal lattice causing distortions. The true crystal species is likely a ternary compound that has no standard reference pattern in the databases.

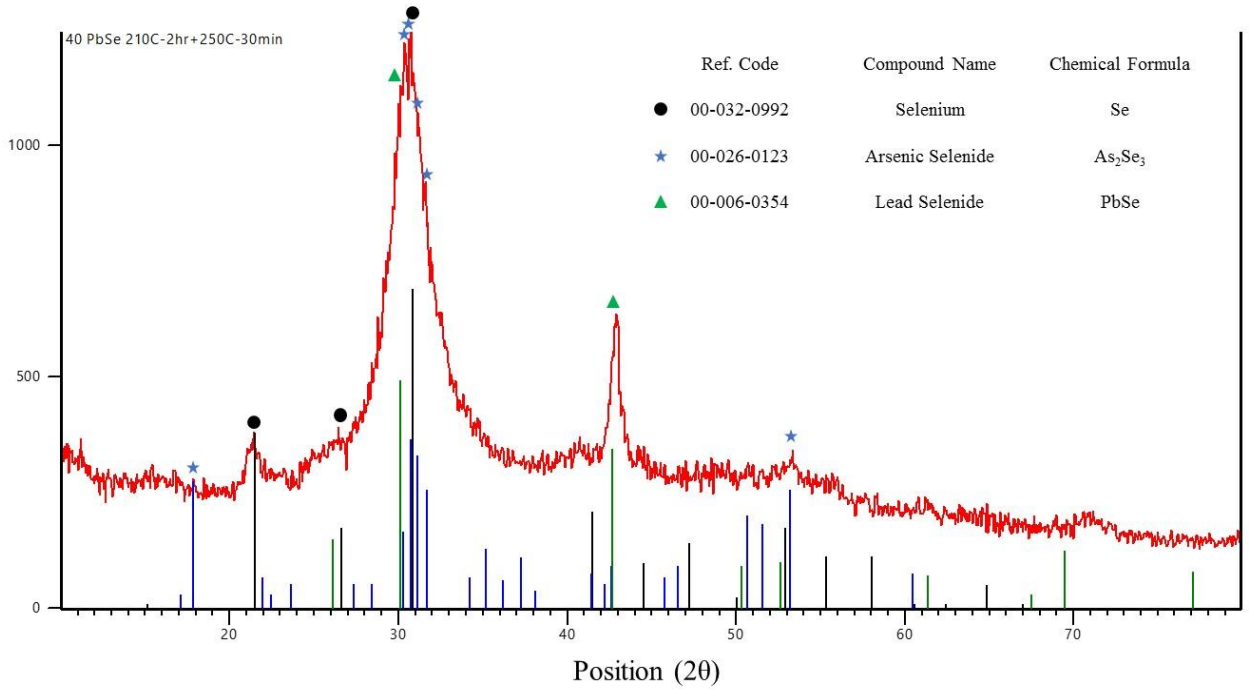

Figure 46 – XRD of heat-treated 40 PbSe glass powder (210°C-2hr+250°C-30min) with peak assignments

The 20 PbSe and 40 PbSe glasses examined in the study both showed droplet-matrix phase separation morphology upon quenching from the melt, but showed opposite Pb-segregation behavior. Specifically, 20 PbSe glass exhibited Pb-rich droplets in a Pb-deficient matrix whereas 40 PbSe exhibited Pb-deficient droplets within a Pb-rich matrix. The Pb-segregation into the droplet or matrix phase of the resulting amorphous phase separated morphology has a large effect on the crystallization behavior on the property evolution of the two glasses. Because the 20 PbSe glass had Pb-rich droplets, the observed crystallization largely took place within the droplets. Conversely, the 40 PbSe glass had a Pb-rich matrix and thus crystallization mainly occurring the matrix. With crystallization in the continuous/majority phase, the 40 PbSe properties are affected more significantly as seen in the larger changes in hardness, density, and refractive index by the

crystallization process than the 20 PbSe where the crystallization occurs in the discontinuous/minority phase.

CHAPTER FIVE: CONCLUSIONS

The research presented in this thesis work has investigated the crystallization behavior in two multicomponent $GeSe_2$-As_2Se_3-PbSe glass compositions containing 20 and 40 mol% PbSe (20 PbSe and 40 PbSe, respectively). The glass system was studied to determine its suitability for use as a candidate GRIN component for use in an IR optical system. Glasses for the desired application must exhibit suitable transmission within the spectral window of use and a sufficient refractive index modification to yield a glass-ceramic composite with measurable Δn as compared to the base glass' refractive index. For the target application, we required a material that exhibited transmission from 3 μm to 5 μm and the ability to induce a measurable change in induced refractive index (through controlled crystallization of a high index, nanocrystalline phase) enabling two- to three-dimensional spatial control and formation of a gradient refractive index.

Both glass compositions were found to exhibit droplet-matrix phase separation for melt sizes and melt/quench protocols used in the study. The as-quenched glass morphology of both glasses possessed a less stable (to crystallization) Pb-rich phase and a more stable, Pb-deficient phase. The two compositions differed in two key ways in that 20 PbSe possessed Pb-rich droplets and 40PbSe was dominated by a Pb-rich matrix phase.

The thermal and physical properties of both glasses were investigated and it was found that both compositions exhibited crystallization that could be controlled through specific nucleation and growth thermal protocols. Thermal analysis was used to generate nucleation and growth curves that provided guidance to the targeted thermal regimes used for subsequent heat-treatments. Index

change, while maintaining suitable transmission, was quantified for both targeted heat-treatment protocols. It was found that the extent and rates of crystallization varied markedly with composition as related to the starting, as-quenched chemistry and morphology. The resulting post-heat-treatment crystallization results in both of the glasses studied, result in a positive induced refractive index change while only the 40 PbSe maintains the required MWIR transmission.

Key findings from the characterization of as-quenched base glass morphology showed that:

- Crystallization tends to occur in the Pb-rich phase of the glass.
- The 20 PbSe glass had Pb-rich droplets and the 40 PbSe glass had a Pb-rich matrix which expected to directly affect the crystallization behavior; the magnitude of this compositional variation between droplets and matrices was quantified via XEDS on TEM specimens prepared to analyze phase separation.
- Droplets in the 20 PbSe glass exhibited a 2-3X increase in Pb (at%) level from the concentration batched and a concurrent decrease in Ge and As; Se showed no variation in concentration inside or outside the droplet.
- Droplets in the 40 PbSe glass exhibited a reduction in Pb content (~2X) and Ge content with a ~1.2X increase in As content.
- Droplets in the 20 PbSe glass (100-130 nm) were found to be roughly twice as big as those in the 40 PbSe glass (35-45 nm).
- Droplet sizes seen in the respective base glass compositions directly affected the short wavelength cutoff of the two glasses; the 20 PbSe glass was found to cut off (90% point, ~ 2 mm part thickness) at 1.993 μm, whereas the 40 PbSe had a shorter wavelength cutoff of

1.319 μm. This is consistent with both the size of the scattering centers seen in the glasses and the expected index difference between the two glass phases estimated based on Pb-content.

- Scale-up of the lab-scale melts to commercial size for 20 PbSe, exacerbated the transmission issue since the larger melt (~1 kg) required slower cooling rates resulting in glasses that contained larger droplet sizes (200-340 nm); in comparison, this led to a transmission cutoff (3.78 μm) in the middle of the desired transmission window for a t = 3 mm part.

Nucleation and growth regimes were defined through the creation of nucleation and growth rate curves from DSC analysis for both compositions. Key findings resulting from these experiments showed:

- The influence of melt size (40g and 150g) while measurable, was small as defined by the position of the temperatures of maximum nucleation and growth rate; 40 PbSe glass showed greater overlap between the two curves reducing the temperature regime where growth could take place without measurable nucleation.
- Two-step thermal treatment conditions were chosen based on these curves which allowed selection of suitable temperatures where nucleation could occur without growth (step 1) and growth could occur without nucleation (step 2). These (specific) temperatures/times were chosen to create nanocomposite samples that were analyzed for property modification discussed below.
- Activation energies for crystallization (based on analysis of the first exotherm found in each glass' DSC scan) were calculated; it was found that crystallization in the 20 PbSe had

a lower activation energy than that seen in the 40 PbSe starting material; we postulate this is due to the higher local Pb content present in the (first) crystallizing phase being present in the majority (matrix) phase, rather than in the minority (droplet) phase.

The impact of crystallization on glass' physical properties were investigated. It was found for the specific nucleation and growth times and temperatures chosen for this specific example, that:

- Crystallization was found to occur initially in the Pb-rich phase; post heat-treated (crystallized) glass-ceramics exhibited changes in hardness, density, and refractive index when crystallization was in the majority (matrix) phase.
- When the crystallization occurred in the minority phase, the hardness and density were changed negligibly while the refractive index still showed significant change.
- After the two-step heat-treatment protocol, both glasses were shown to produce a significant Δn, but the heat-treatment required to attain this Δn in the 20 PbSe glass led to an unacceptable loss in transmission.

This work demonstrates how phase separated glasses differ in their post heat-treated physical property changes. Additionally, the role of the lower stability phase being in the majority (matrix) or minority (droplets) for metastable phase separated glasses has been shown. These findings show how control of the crystallization process can be used to develop a nanocomposite glass-ceramic with a measurable refractive index change (up to 0.119) with a corresponding acceptable MWIR transmission. From these findings, such materials can be considered candidates for GRIN components in an IR optical system. While the composition and crystallization protocols may require further optimization the basis of this work clearly demonstrates how knowledge of the

starting glass morphology and crystallization behavior can be used to engineer a suitable glass-ceramic for advanced optical applications.

APPENDIX A:
2016 DCS PROCEEDING

Engineering Novel Infrared Glass Ceramics for Advanced Optical Solutions

K. Richardson*[a], A. Buff[a], C. Smith[a], L. Sisken[a], J. David Musgraves[b], P. Wachtel[b], T. Mayer[c, e], A. Swisher[c], A. Pogrebnyakov[c], M. Kang[c], C. Pantano[c], D. Werner[c], A. Kirk[d], S. Aiken[d], C. Rivero-Baleine[d]

[a]College of Optics and Photonics, CREOL, University of Central Florida, 4000 Central Florida Blvd., Orlando, FL, USA 29650; [b]IRradiance Glass, Inc., 3267 Progress Drive, Orlando, FL, USA 32826; [c]Dept. of Electrical Engineering, The Pennsylvania State University, University Park, PA, USA 16802; [d]Lockheed Martin Corporation, Orlando, FL, USA 32819; [e]now at Virginia Polytechnic Institute and State University, Blacksburg VA 24061

Abstract

Advanced photonic devices require novel optical materials that serve specified optical function but also possess attributes which can be tailored to accommodate specific optical design, manufacturing or component/device integration constraints. Multi-component chalcogenide glass (ChG) materials have been developed which exhibit broad spectral transparency with a range of physical properties that can be tuned to vary with composition, material microstructure and form. Specific tradeoffs that highlight the impact of material morphology and optical properties including transmission, loss and refractive index, are presented. This paper presents the crystallization behavior and property evolution of 20 $GeSe_2$-60 As_2Se_3-20 PbSe glass including a demonstration of a 1D GRIN profile through the use of controlled crystallization.

Keywords: Chalcogenide glass, GRIN, glass-ceramic, nucleation, crystallization, infrared nanocomposite

Introduction

Chalcogenide glasses are well known for their mid-IR transparency and their high refractive index, but are limited by their weak thermal/mechanical properties. Controlled crystallization of the base glass can improve these properties as observed in oxide and non-oxide glasses.[1, 3, 24] Additionally, introducing crystals may introduce other effects such as change in refractive index and nonlinear optical properties.[4-6] Recent activities by researchers including the those of the present effort[8] have been investigating the strategy to realize manufacturable gradient refractive index materials as part of the DARPA M-GRIN program.[7]

A study of glass formation and properties of $GeSe_2$-As_2Se_3-PbSe system was reported by Yang et al.[10] In their work, they sought a suitable glass composition space for development of IR-transmitting chalcogenide glass-ceramic. In their previous work,[24, 25] the group demonstrated that a stable glass composition is key to producing IR-transmitting chalcogenide glass-ceramics. Compared to the similar previously reported GeS_2-Sb_2S_3-PbS system[24], the $GeSe_2$-based glasses have better rigidity, chemical stability, and transmit further into the IR.[10] Additionally, As2Se3 favors thermal stability which helps control the crystallite size during heat-treatment.[10, 25] Controlled crystallization of these glasses are important because uncontrolled crystal size leads to opaque glass-ceramics which cannot transmit in the IR.[26, 27] Yang et al. mapped the glass forming region of this system (Figure 1).[10] In this system, the relatively low Pb content is expected to fill the role of a nucleation agent with further heat-treatment,[10] as similarly reported for an analogous sulfide system.[24]

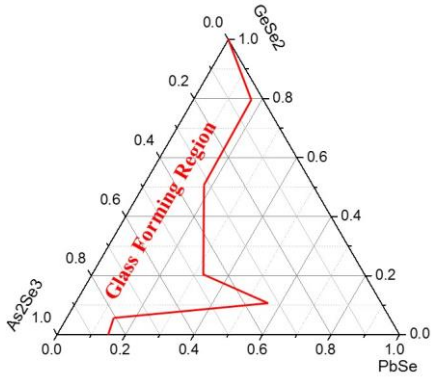

Figure 1. Glass forming region of the $GeSe_2$-As_2Se_3-PbSe system

In the present work, we summarize results of efforts to induce 'effective' optical properties that result from controlled nucleation and growth of a secondary phase in a base matrix. By controlling the relative volume fraction of each phase (glass and crystallite) in a composite, two phase material, effective properties can be estimated based on the lever-rule. Here, the effective refractive index, n_{eff}, can be approximated by knowing the volume fraction (v) of each respective phase and its index, n, as shown in equation (1),

$$n_{eff} = (v_{glass})(n_{glass}) + (v_{crystal})(n_{crystal}) \quad (1)$$

where v indicates the volume fraction, and n is the species' refractive index at the wavelength of interest. Formation of a glass-ceramic which contains a volume fraction, $v_{crystal}$ of crystalline species with index $n_{crystal}$ yields a resulting glass-ceramic index, $n_{glass\text{-}ceramic}$ where the index change, Δn from that of the parent glass can be quantified by measurement of the starting glass and resulting glass-ceramic indices as shown in equation (2).

$$\Delta n = (n_{glass\text{-}ceramic}) \approx (n_{glass+crystal} - n_{glass}) \quad (2)$$

For infrared optical applications where spatial (x, y, and z) control of crystal growth to realize a nanocomposite can create a gradient in refractive index (GRIN), the goal is to choose a host material system that results in formation of a secondary crystalline phase with index either higher or lower than the parent glass possessing low absorption in the band of interest. A key issue is the need for controlled crystallization behavior which will enable a nanocomposite with monosized, small crystallites, that minimizes scattering. Spatial variation in the number density of such crystallites yields a gradient in n_{eff} and creates the resulting GRIN medium. As can be seen such as depicted in Figure 2, this work aims to create such a gradient nanocomposite in a multicomponent chalcogenide glass material suitable for use in the mid- and longwave-infrared region of the spectrum.

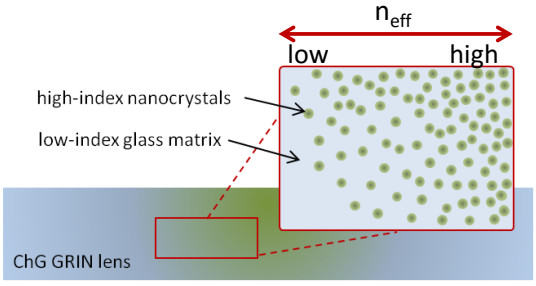

Figure 2. Chalcogenide glass (ChG) GRIN lens where a gradient index is created through the spatial control of high refractive index particles embedded in a lower refractive index glass matrix

To identify the formation mechanisms needed to create the phase with such spatial control is the unique aspect of this approach. The $GeSe_2$-As_2Se_3-PbSe (GAP-Se) system exhibits many of these desirable attributes and forms the basis of our investigation.

Experimental

$GeSe_2$-As_2Se_3-PbSe glasses were batched in an MBraun Labmaster 130 glove box with a controlled atmosphere (O_2<10 ppm and H_2O<10 ppm). All glasses were prepared using high purity raw materials (metals basis) from Alfa Aesar: selenium (99.999%), germanium (99.999%), antimony (99.999%), and lead (99.999%). The glass batches were put into cleaned fused quartz tubes and sealed under vacuum to form ampoules. The glasses were melted in a rocking furnace overnight. The molten glass was quenched from the melting temperature by flowing compressed air over the ampoules.

Thermal analysis was performed using a TA Instruments DSC 2920 Differential Scanning Calorimeter (DSC). Bulk samples of glass were finely crushed (< 125 μm) and put into sealed aluminum pans (30 ± 2.5 mg of glass). The base heating rate of the DSC curves was 10 °C/min. The DSC was used to create nucleation-like and growth-like curves by analyzing curves after isothermal holds in the DSC. For these runs, the samples were rapidly heated (20°C/min) to a test temperature, held for a set time (2 hours for nucleation, 30 minutes for growth) then rapidly cooled below T_g before being ramped up at the normal base rate.

Bulk samples of glass were heat-treated in furnaces in an open-air atmosphere. Heat-treated samples underwent a nucleation heat-treatment at 220°C for 2 hours. Samples underwent growth heat-treatments at 240°C, 250°C, and 270°C for 2 hours. A gradient furnace with a linear temperature profile from 225°C to 260°C was used to heat-treat a 5 cm long rod that was previously underwent a nucleation heat-treatment.

Transmission data was obtained using Fourier Transform Infrared spectroscopy (FTIR). FTIR was performed on base and heat-treated samples (as described above). Measurements were done over a range of wavelengths from 1.7 to 6 μm on 1 mm thick samples that were done on double-sided polished samples.

Hot stage in-situ X-ray Diffraction (XRD) was performed on the base class over the course of a multistep heating schedule. The in-situ XRD run consisted of a scan at room temperature, three scans during the nucleation step at 220°C for 2 hours, three scans during the growth step at 270°C for 2 hours. Scans were taken using Cu k_α radiation with a scan range from 0-70°.

Field emission scanning electron microscopy (SEM) was performed on samples that were heat-treated under the protocols described above. Transmission Electron Microscopy (TEM) was performed on shards of glass using. TEM samples were prepared by finely grinding powder from the center of the glass rod. The glass powder was placed in isopropyl alcohol and sonicated for 5 minutes. A few drops were placed on a lacey carbon TEM grid. The bright field images were obtained using 200 keV voltage, 1 nA current, and 500K - 600K magnification (high mag). Energy-dispersive X-ray spectroscopy (XEDS) was used to identify the compositions of the crystal and matrix phases.

Hardness and coefficient of thermal expansion were determined for glasses before heat-treatment, after nucleation heat-treatment, and after growth heat-treatment. Hardness measurements were performed on a Shimadzu DUH-211S Hardness Tester using a Vickers diamond indenter. Indents were performed using a 100 mN load with a hold time of 10 seconds. The coefficient of thermal expansion for the glasses was determined using a thermomechanical analyzer (TMA). The test samples were in the form of 10 mm-long glass rods with a 10 mm diameter. The change in length of the rod was measured from 50°C to 150°C with a 3°C/min heating rate.

Results and Discussion

The goal of this work is to study multi-component chalcogenide glass materials for use in infrared GRIN lenses. For this application, it is important to understand the properties of the base glass, the crystallization behavior and how the properties change with crystallization.

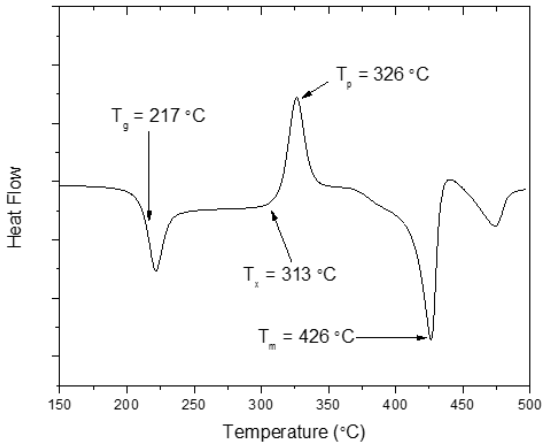

Figure 3. DSC of 20 $GeSe_2$-60 As_2Se_3-20 PbSe glass. Heating rate 20°C/min. Exothermic up.

Figure shows the differential scanning calorimetry (DSC) data of the 20 $GeSe_2$-60 As_2Se_3-20 PbSe glass. The DSC plot shows that the glass transition temperature (taken as the point of inflection of the first endothermic feature) was found to be T_g = 217°C. The figure also shows a prominent crystal peak (first exothermic feature) that starts at T_x = 313°C with the crystallization peak at T_p = 326°C. Following the first crystal peak there is a second crystal peak around 375°C. The melting endothermic features corresponding to the two crystal phases are shown with their peaks at 426°C and 480°C. This property data was used as basis for developing nucleation and growth protocols.

In order to establish a heat-treatment protocol, nucleation-like and growth-like curves were developed using techniques described in Massera et al.[28] Figure shows the nucleation-like and growth-like curves for the 20 $GeSe_2$-60 As_2Se_3-20 PbSe composition. The nucleation-like curves shows nucleation occurs over the range of 200°C to 240°C with the maximum nucleation rate at 220°C. The growth-like curve shows that growth starts after 240°C and continues to increase to 290°C where it reaches its maximum measureable growth rate by this technique. The two curves show good separation in that the nucleation rate is low during the growth regime and vice-versa. This crystallization behavior is essential for controlled crystallization. A two-step heat-treatment protocol can be implemented so that the first step uniformly nucleates crystals in the glass matrix. A second heat-treatment step would then grow the nucleated crystals to a uniform size. By selectively nucleating or growing crystals, the local refractive index can be changed to yield a specified microstructure containing the desired volume fraction of crystals and a corresponding glass fraction to locally yield the desired n_{eff}. With spatial control of the local formation, a gradient refractive index can be created.

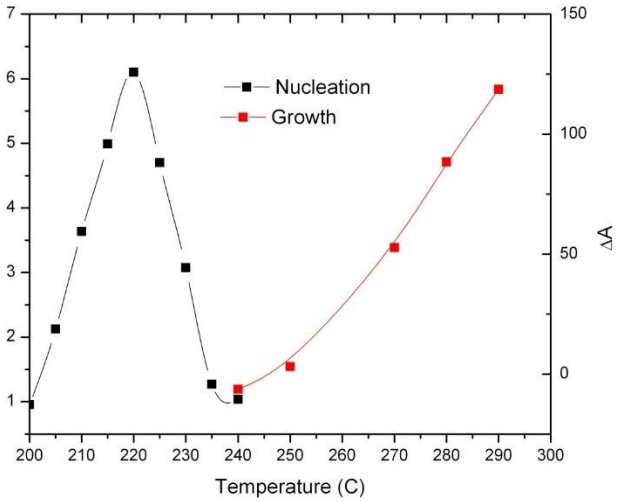

Figure 4. Nucleation-like (I) and growth-like (U) curves for 20 $GeSe_2$-60 As_2Se_3-20 PbSe glass

Using heat-treatment conditions defined by the specific composition's I-U curve, one can create crystals that can be detected via TEM, such as shown in Figure 5. The irregularly shaped crystalline particles are darker in the image than the surrounding matrix due to their higher Pb content as shown by the XEDS results in Table.

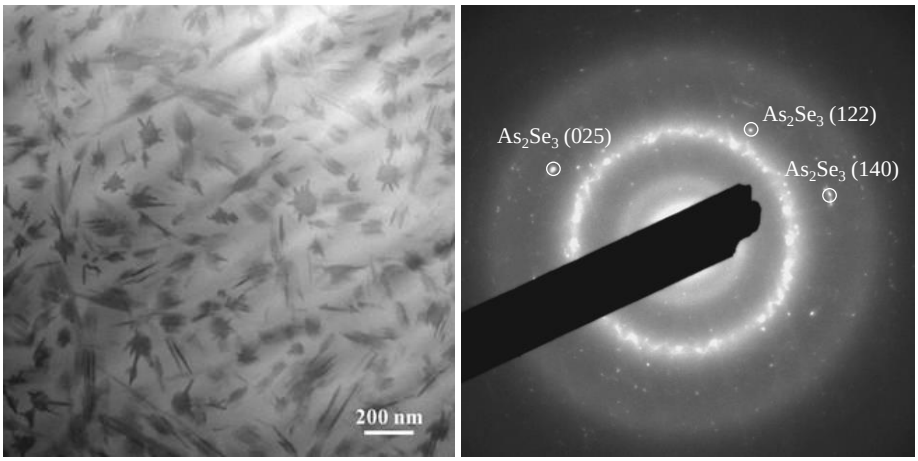

Figure 5 - TEM image (left) of heat-treated 20 $GeSe_2$-60 As_2Se_3-20 PbSe following a two-step heat-treatment protocol. Distinct crystal phases, PbSe and As_2Se_3 can be seen as confirmed by SAED (right).

Table 1 - XEDS results from TEM of heat-treated 20 $GeSe_2$-60 As_2Se_3-20 PbSe

Element	Particle (at%)	Matrix (at%)
Ge	4.2 ± 0.4	8.6 ± 0.6
As	21.8 ± 0.7	27.1 ± 1.0
Se	56.2 ± 0.9	58.9 ± 1.3
Pb	17.9 ± 1.6	5.4 ± 1.8

Without tight control of conditions that control crystallite size and number density, scattering can result such as shown in Figure 6. Figure shows how the short wavelength cutoff of the glasses shifts to higher wavelengths with increasing growth temperature in the high growth rate temperature regime. As the growth temperature increases, the increased crystal growth rates lead to larger crystal sizes. The presence of crystals leads to a loss of transmission (Mie

scattering) of wavelengths up to 10 times larger than the size of the crystal. For GRIN lenses, it is important to have crystals large enough to affect the local refractive index, but not so large that they cause scattering in the application window (here, mid-wave, λ = 3-5 μm). These competing factors highlight the importance of understanding the crystallization behavior in order to crystallize the glass in a controlled manner. The results from the transmission study show that the increased growth temperature leads to lower short-wavelength transmission.

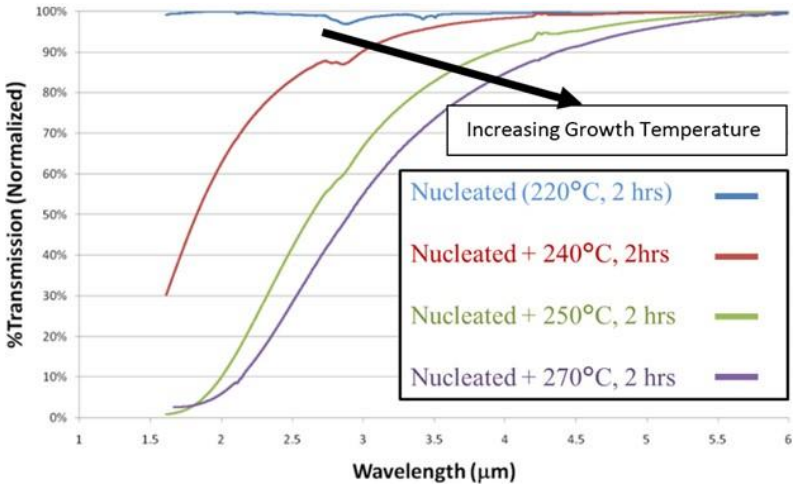

Figure 6 - Impact of scattering induced by crystal growth rates which adversely impact short wavelength transmission in heat-treated 20 $GeSe_2$-60 As_2Se_3-20 PbSe

The evolution of the crystal phase was observed via in-situ hot stage XRD. XRD scans were run as the sample underwent a nucleation and growth heat-treatment times and temperatures. Figure shows multiple scans (1-8) over the nucleation and growth heat-treatment schedule employed for this analysis. Scan 1 was run before the heat-treatment began, scans 2-4 occurred during the nucleation step, scans 5-7 occurred during the growth step, and scan 8 was taken after the heat-treatment protocol at room temperature. As the heat-treatment progressed, the features seen around $2\theta = 31°$ and 42° became more defined. This sharpening of features indicates that crystal growth occurs during the heat-treatment. While the crystal features in the XRD are not sharp enough to definitively identify the crystal phases, they are consistent with the known As_2Se_3 and PbSe crystal phases.

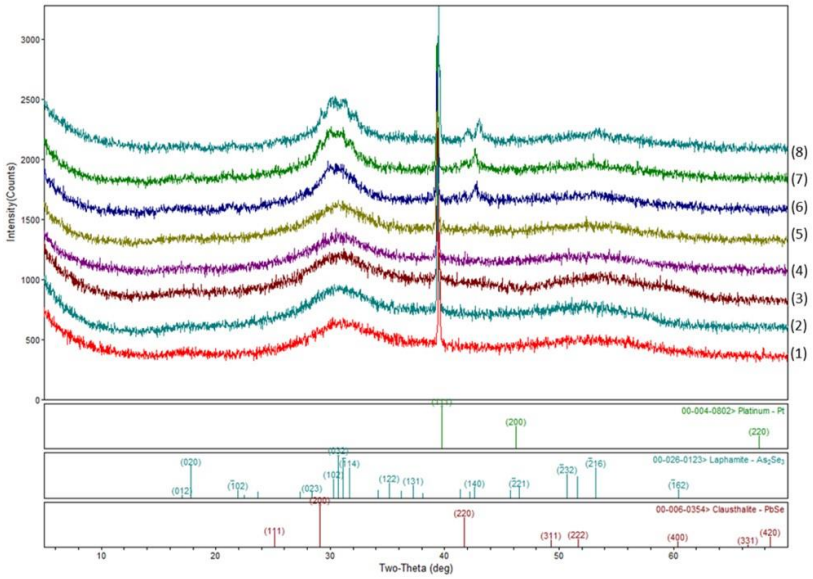

Figure 7 - In-situ hot stage X-ray Diffraction of 20 $GeSe_2$-60 As_2Se_3-20 PbSe with Pt sample holder

As a demonstration of a true GRIN profile, a pre-nucleated, 5 cm long rod of 20 $GeSe_2$-60 As_2Se_3-20 PbSe was placed in a furnace with a linear temperature gradient (225°C to 260°C) that spanned a representative high growth rate temperature regime. Here the goal was to induce a gradient in volume fraction crystallites along the length of the rod, which would translate into a step-wise gradient in effective refractive index, n_{eff}. Since crystallite size is related to growth rate (varying) at heat-treatment temperature (temperature range shown), a single rod would be expected to contain varying crystallite volume fractions. Here, the rod was sliced and slices were ground, polished and then measured for index as a function of spatial position in the rod. The refractive index of the rod was measured at several points throughout the rod at three different wavelengths (λ = 3 μm, 4 μm, and 5 μm). As can be seen in Figure , the refractive index through the rod increases as function of distance along the rod, resulting in the production of a 1D (longitudinal) GRIN profile. Extension of such thermal control to other directions (radial, axial) or the use of laser exposure to nucleate the formation of nuclei required for subsequent crystallization, will result in the formation of a spatially controlled, 2- or 3D GRIN profile.

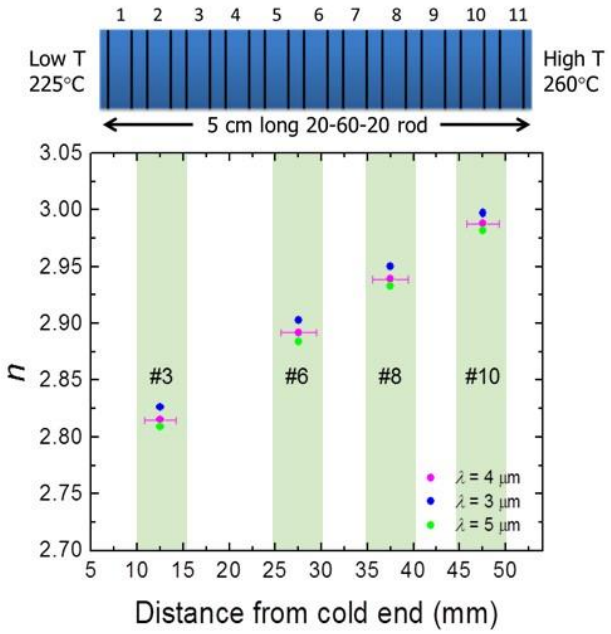

Figure 8 - Refractive index as a function of spatial position through 5 cm long rod heat-treated in gradient furnace; slice number on rod (above) correspond with slice numbers (#3, #6, #8 and #10) measured at three, mid-IR wavelengths

Following the creation of the secondary crystalline phase, the resulting glass-ceramic has not only modified optical properties but also other changes to physical properties which can be quantified as being intermediate to that of the parent bulk glass and fully crystallized ceramic. For a related GAP-Se glass-ceramic, these properties have been tabulated as compared to SCHOTT's IRG 26, As2Se3 glass. Shown in table 2 is the evolution of physical properties for the base glass, nucleated only and nucleated and grown glass-ceramic created under conditions similar to those discussed above.

Table 2 Physical properties of GAP-Se material as compared to commercial IRG 26 glass (As_2Se_3)[50]

Property	As_2Se_3*	GAP-Se	Nucleated	Grown
Transmission Window (μm)	1.0-12	1.1-16	1.2-16	2.0-16
Refractive Index (at 4 μm)	2.7946	2.9565	2.9885	3.2968
dn/dT (x 10^{-6} °C^{-1}) (at λ, μm)	36.1-32.7 (3-5 μm)	47 (3.39)	--	--
Glass transition temperature, Tg (°C)	185	189	189	189
Softening point, (°C)	--	213	--	--
Crystallization Temp, T_x, (°C)	--	250	250	250
Upper Use temperature (°C)	--	162	162	163
Dispersion value (3-5 μm)		69	71	41
Thermal expansion (ppm/°C)	20.8	18.82	19.13	19.31
Density (g/cm^3)	4.63	5.5677	5.6361	5.5394
Micro-hardness (GPa)	1.04	1.657	1.638	1.785

Conclusion

This work reports the use of controlled crystallization to produce a GRIN profile in multi-component $GeSe_2$-As_2Se_3-PbSe (GAP-Se) glass. From studying the crystallization behavior of this glass, it was determined that the nucleation and growth regimes were well separated. The nucleation and growth curves were used to develop heat-treatments for bulk samples. The bulk heat-treatments showed results consistent with the growth curve measurements. The presence

of Pb-rich crystals after heat-treatment were able to locally change the refractive index of the glass. The authors were able to demonstrate an effective 1D GRIN profile using a gradient furnace to spatially control the growth rate in the glass. The same formation of the GRIN behavior results in changes in the physical properties which are intermediate to that of the base glass and that of a fully crystallized ceramic of the same conditions.

ACKNOWLEDGMENTS

This work was supported by the Defense Advanced Research Projects Agency under Air Force Research Laboratory contract FA8650-12-C-7225 through the M-GRIN Tech Area 2 program.

REFERENCES

[1] Mueller, R. W., Hoeness, H. W. and Glaswerke, S., "Spin-cast ZERODUR mirror substrates of the 8 m class and lightweighted substrates for secondary mirrors," Adaptive optics and optical structures, 288-97 (1990).
[2] Shelby, J. E., [Introduction to Glass Science and Technology], The Royal Society of Chemistry, Cambridge, UK (2005).
[3] Xia, F., Zhang, X., Ren, J., Chen, G., Ma, H. and Adam, J. L. , "Glass formation and crystallization behavior of a novel GeS2-Sb2S3-PbS chalcogenide glass system," J Am Ceram Soc 89(7), 2154-7 (2006).
[4] Lumeau, J., Sinitskii, A., Glebova, L., Glebov, L. B. and Zanotto, E. D. , "Method to assess the homogeneity of partially crystallized glasses: application to a photo-thermo-refractive glass," J.Non Cryst.Solids 355(34-36), 1760-8 (2009).
[5] Oikawa, T., Honma, T. and Komatsu, T. , "Laser-induced crystal growth of nonlinear optical Ba3Ti 3O6 (BO3)2 on glass surface," Crystal Research and Technology 43(12), 1253-1257 (2008).
[6] Zeng, H., Liu, Z., Jiang, Q., Li, B., Yang, C., Shang, Z., Ren, J. and Chen, G. , "Large third-order optical nonlinearity of ZnO-Bi2O3-B2O3 glass-ceramic containing Bi2ZnB2O7 nanocrystals," Journal of the European Ceramic Society 34(16), 4383-4388 (2014).
[7] Mayer, T., Werner, D., Rivero-Baleine, C. and Richardson, K. "Innovative Design and Manufacturing of Gradient-Index-Based Transformation Optics Components," FA8650-12-C-7225 (2012).
[8] Maher, M. "Manufacturable Gradient Index Optics (M-GRIN)," DARPA, 2016 <http://www.darpa.mil/program/manufacturable-gradient-index-optics> (17 February 2016).
[9] Yang, G., Zhang, X., Ren, J., Yunxia, Y., Chen, G., Ma, H. and Adam, J. L. , "Glass formation and properties of chalcogenides in a GeSe 2-As2Se3-PbSe system," J Am Ceram Soc 90(5), 1500-1503 (2007).
[10] Donghui, Z., Fang, X., Guorong, C., Xianghua, Z., Hongli, M. and Adam, L. J. , "Formation and properties of chalcogenide glasses in the GeSe2-As2Se3-CdSe system," J Am Ceram Soc 88(11), 3143-6 (2005).
[11] Cheng Ji-jian, "Microstructure and properties of selenide glasses after controlled crystallization," Proceedings of the International and VIIth University Conference on Glass Science, 303-8 (1983).

[12] Soon-Mo Song, Se-Young Choi and Yong-Keun Lee , "Crystallization property effects in Ge30Se60Te10 glass," J.Non Cryst.Solids 217(1), 79-82 (1997).
[13] Massera, J., Remond, J., Musgraves, J., Davis, M. J., Misture, S., Petit, L. and Richardson, K. , "Nucleation and growth behavior of glasses in the TeO2–Bi2O3–ZnO glass system," J.Non Cryst.Solids 356(52–54), 2947-2955 (2010).
[14] SCHOTT , "Infrared Chalcogenide Glasses," 17 February 2016 <http://www.us.schott.com/advanced_optics/english/products/optical-materials/ir-materials/infrared-chalcogenide-glasses/> (17 February 2016).

APPENDIX B:
MACH-ZEHNDER INTERFEROMETER FOR 2-D GRIN PROFILE MEASUREMENT

UNIVERSITY of ROCHESTER

Mach-Zehnder Interferometer for 2-D GRIN Profile Measurement

Instrument Overview
Sample Preparation
Measurement Uncertainty

University of Rochester
Gradient-Index Research Group

2D GRIN Measurement: Mach-Zehnder Interferometer

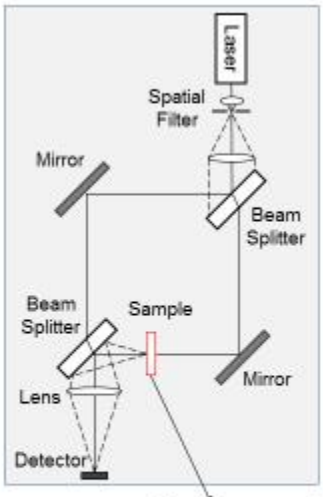

- Wavelength range covered
  - 0.355 – 1.064μm, 1.55 – 4.6μm, 8 – 12μm
- Measurement accuracy
  - δ(Δn) ~ 1E-5
- Beam size: 65mm x 40mm ellipse
- Sample prep requirements
  - Thin (~1mm), plane, parallel sample with GRIN "exposed" (index is constant through sample thickness)

$$\phi(x,y) = \frac{2\pi}{\lambda}\left(\Delta n(x,y)\right)t$$

Measure: ϕ, t
Calculate: Δn

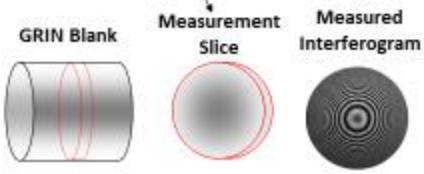

Mach-Zehnder Sample Prep

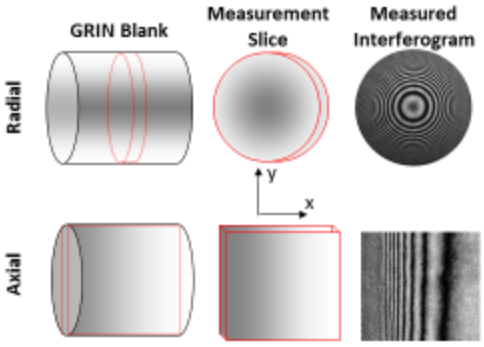

$$\#\text{ of Fringes} = N = \frac{t}{\lambda}\Delta n$$

- Sample thickness chosen so that # of fringes can be resolved by imaging optics and detector
- Surface figure error and wedge lead to measurement error

- Thin slice cross-section that "exposes" the gradient for measurement
- Index should be constant through the thickness of the sample (z-axis)

3

Mach-Zehnder Measurement Uncertainty

$$\Delta n = \frac{m\lambda}{t}$$

m = # of fringes
λ = wavelength
t = thickness

Best-case uncertainty is determined by a root-sum-square of the terms in the Δn calculation

$$\delta(\Delta n) = \sqrt{\left(\frac{\lambda}{t}\delta n\right)^2 + \left(\frac{m\lambda}{t^2}\delta t\right)^2 + \left(\frac{m}{t}\delta\lambda\right)^2}$$

Uncertainty is increased further by surface figure error and wedge, but it can be minimized by measuring in an index matching fluid

Uncertainty due to:	Expression
- Figure error measured in air - Wedge error if no known homogeneous region	$\delta(\Delta n) = \frac{\delta t}{t}(n_{samp} - 1)$
- Figure error measured in fluid	$\delta(\Delta n) = \frac{\delta t}{t}(n_{samp} - n_{fluid})$
- Figure error measured in matched fluid ($n_{fluid} = n_{samp}$ at some location in sample) - Wedge error if there is a known homogeneous region	$\delta(\Delta n) = \frac{\delta t}{t}\Delta n$

Use the calculator on the next slide to determine the measurement error for your sample

4

Calculation of Measurement Uncertainty

RSS uncertainty			Sample Prep Errors		
Best-case measurement uncertainty					
m	35		n_{samp}	1.78	
δm	0.02		sample Δn	0.03	
t (μm)	1500		n_{fluid}	1.7	
δt	1		δt (μm)	1	= 1.58 waves (λ = 0.632 μm)
λ (μm)	0.6328				
δλ	0.00005				
			Figure Error in Fluid		
δ(Δn)	1.302E-05		**δ(Δn)**	5.33E-05	
			Figure Error in Matched Fluid		
	User Input		(or wedge if known homog. Region)		
	Calculated Value		**δ(Δn)**	2.00E-05	
			Figure Error in Air		
			(or wedge if no known homog. Region)		
			δ(Δn)	5.20E-04	

- Notes:
  - Interferometer accuracy is on the order of λ/50 (δm = 0.02)
  - Wavelength uncertainty is typically small and does not contribute much error
  - Best uncertainty is achieved by making the sample as thick as possible while maintaining the ability to resolve fringes (see next slide)

5

Calculation of Fringe Density

$$\Delta n = \frac{m\lambda}{t}$$

m = # of fringes
λ = wavelength
t = thickness

$$\#\text{ of Fringes} = N = \frac{t}{\lambda}\Delta n$$

- The fringe density limits the thickness of the sample
- Thicker samples will eventually reach a fringe density that cannot be resolved
- Use calculator below to estimate fringe density in your samples

thickness (μm)	1500	
wavelength (μm)	0.6328	
sample Δn	0.03	
spatial extent of gradient (mm)	1.2	
index slope (mm^{-1})	0.02500	
# of fringes	71.1	
fringe density (mm^{-1})	59.3	
	User Input	
	Calculated Value	

- Notes:
  - For wavelengths in the visible and NIR, the maximum fringe density that can be resolved by the interferometer is ≈**100 mm^{-1}**
  - Samples with large fringe density will require a smaller field of view
    - Stitching may be required to measure the full sample

6

APPENDIX C:
SAGNAC RING INTERFEROMETER FOR ABSOLUTE INDEX OF REFRACTION MEASUREMENTS

Sagnac Ring Interferometer for Absolute Index of Refraction Measurements

Instrument Overview
Sample Preparation
Measurement Uncertainty

University of Rochester
Gradient-Index Research Group

Absolute Index: Sagnac Interferometer

- Wavelength range covered
  - 0.355 – 1.064µm, 1.55 – 4.6µm, 8 – 12µm
- Measurement accuracy
  - δn = 1E-4 (for a well-finished sample)
- Sample prep requirements
  - Thick (> 5mm), plane, parallel window
  - Diameter > 15mm
  - Surface curvature less than one wave over a 10 mm aperture
  - Wedge less than 2 arc min for most accurate results

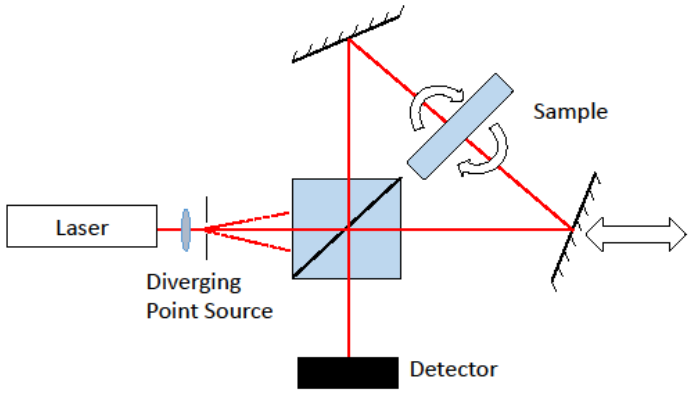

2

Shear in Sagnac Ring Interferometer

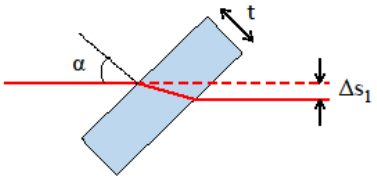

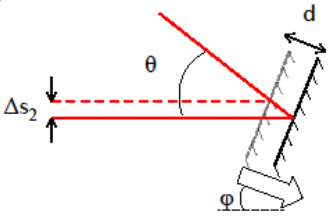

$$\Delta s_1 = t\cos\alpha\left\{\tan\alpha - \tan\left[\sin^{-1}\left(\frac{n_a}{n_s}\sin\alpha\right)\right]\right\}$$

$$\Delta s_2 = d\left(\frac{\sin\theta\cos\left(\theta/2 - \phi\right)}{\cos\left(\theta/2\right)}\right)$$

$$n_s = \frac{n_a\sin\alpha}{\sin\left\{\tan^{-1}\left[\tan\alpha - \frac{d\sin\theta\cos\left(\theta/2-\phi\right)}{t\cos\alpha\cos\left(\theta/2\right)}\right]\right\}}$$ Index

$$\delta n_s = \left(\frac{n_s^2}{n_{air}} - n_s\right)\frac{\delta t}{t}$$ Index Uncertainty

When Shear is Present:

- Shear can be seen in interferogram and eliminated to within a fraction of λ
- Index can be calculated for many different shears and averaged
- Index uncertainty: limited by sample thickness uncertainty (δt typically 1 μm)

REFERENCES

1. J.E. Shelby, *Introduction to Glass Science and Technology;* The Royal Society of Chemistry, Cambridge, UK, 2005.

2. T.H. Courtney, *Mechanical Behavior of Materials;* Waveland Press, Inc., Long Grove, Illinois, 2000.

3. R.W. Mueller, H.W. Hoeness and S. Glaswerke. "Spin-cast ZERODUR mirror substrates of the 8 m class and lightweighted substrates for secondary mirrors," Proceedings of the SPIE - The International Society for Optical Engineering, **1271,** 288-97 (1990).

4. J. Lumeau, A. Sinitskii, L. Glebova, L.B. Glebov and E.D. Zanotto. "Method to assess the homogeneity of partially crystallized glasses: application to a photo-thermo-refractive glass," J. Non Cryst. Solids, **355,** 1760-8 (2009).

5. T. Oikawa, T. Honma and T. Komatsu. "Laser-induced crystal growth of nonlinear optical Ba3Ti 3O6 (BO3)2 on glass surface," Crystal Research and Technology, **43,** 1253-7 (2008).

6. H. Zeng, Z. Liu, Q. Jiang, et al. "Large third-order optical nonlinearity of ZnO-Bi2O3-B2O3 glass-ceramic containing Bi2ZnB2O7 nanocrystals," Journal of the European Ceramic Society, **34,** 4383-8 (2014).

7. M. Maher, "Manufacturable Gradient Index Optics (M-GRIN)," **2016,**

8. T. Mayer, D. Werner, C. Rivero-Baleine and K. Richardson. "Innovative Design and Manufacturing of Gradient-Index-Based Transformation Optics Components," **FA8650-12-C-7225,** (2012).

9. K. Richardson, J.D. Musgraves, P. Wachtel, C. Rivero-Baleine and T. Mayer. "Method of Forming an Optical Device and Optical Apparatus," U.S. Pat. 9,340,446, 2016.

10. G. Yang, X. Zhang, J. Ren, et al. "Glass formation and properties of chalcogenides in a GeSe 2-As2Se3-PbSe system," J Am Ceram Soc, **90,** 1500-3 (2007).

11. B. Jensen and A. Torabi. "The refractive index of compounds PbTe, PbSe, and PbS," IEEE J. Quant. Electron., **QE-20,** 618-21 (1984).

12. S. Sapra, J. Nanda, J.M. Pietryga, J.A. Hollingsworth and D.D. Sarma. "Unraveling internal structures of highly luminescent PbSe nanocrystallites using variable-energy synchrotron radiation photoelectron spectroscopy," J Phys Chem B, **110,** 15244-50 (2006).

13. S. Hudgens and B. Johnson. "Overview of phase-change chalcogenide nonvolatile memory technology," MRS Bull, **29,** 829-32 (2004).

14. K. Richardson, N. Carlie, J. David Musgraves, et al. "Integrated chalcogenide waveguide resonators for mid-IR sensing: Leveraging material properties to meet fabrication challenges," (2011).

15. L. Yajing, S. Baoan, D. Wei, et al. "Application of chalcogenide glass in car night-vision system," Infrared and Laser Engineering, **43,** 2815-18 (2014).

16. M. Roze, L. Calvez, Y. Ledemi, M. Allix, G. Matzen and X. Zhang. "Optical and mechanical properties of glasses and glass-ceramics based on the Ge-Ga-Se system," J Am Ceram Soc, **91,** 3566-70 (2008).

17. A.K. Varshneya, *Fundamentals of Inorganic Glasses;* Academics Press, Inc., San Diego, CA, 1994.

18. M.J. Madou, *Fundamentals of microfabrication and nanotechnology. Volume 1, Volume 1,* CRC Press, Boca Raton, FL, 2012.

19. W.H. Armistead and S.D. Stookey. "Photochromic silicate glasses sensitized by silver halides," Science, **144,** 150-4 (1964).

20. S.D. Stookey, G.H. Beall and J.E. Pierson. "Full-color photosensitive glass," J. Appl. Phys., **49,** 5114-23 (1978).

21. X. Zhang, H. Ma, J. Lucas, Y. Guimond and S. Kodjikian. "Optical fibers and molded optics in infrared transparent glass-ceramic," J. Non Cryst. Solids, **336,** 49-52 (2004).

22. G. Dong, H. Tao, X. Zhao, X. Xiao, C. Lin and H. Guo. "Second harmonic generation in transparent microcrystalline -CdGa2S4-containing chalcogenide glass ceramics," Opt. Commun., **274,** 466-70 (2007).

23. L. Calvez, H. Ma, J. Lucas and X. Zhang. "Selenium-based glasses and glass ceramics transmitting light from the visible to the far-IR," **19,** 129-32 (2007).

24. F. Xia, X. Zhang, J. Ren, G. Chen, H. Ma and J.L. Adam. "Glass formation and crystallization behavior of a novel GeS2-Sb2S3-PbS chalcogenide glass system," J Am Ceram Soc, **89,** 2154-7 (2006).

25. Z. Donghui, X. Fang, C. Guorong, Z. Xianghua, M. Hongli and L.J. Adam. "Formation and properties of chalcogenide glasses in the GeSe2-As2Se3-CdSe system," J Am Ceram Soc, **88,** 3143-6 (2005).

26. Cheng Ji-jian, "Microstructure and properties of selenide glasses after controlled crystallization," J. Non Cryst. Solids, **56,** 303-8 (1983).

27. Soon-Mo Song, Se-Young Choi and Yong-Keun Lee. "Crystallization property effects in Ge30Se60Te10 glass," J. Non Cryst. Solids, **217,** 79-82 (1997).

28. J. Massera, J. Remond, J. Musgraves, et al. "Nucleation and growth behavior of glasses in the TeO2–Bi2O3–ZnO glass system," J. Non Cryst. Solids, **356,** 2947-55 (2010).

29. K. Matusita, T. Komatsu and R. Yokota. "Kinetics of nonisothermal crystallization process and activation energy for crystal growth in amorphous materials," J. Mater. Sci., **19,** 291-6 (1984).

30. S. Kurajica, A. Bezjak and E. Tkalcec. "Resolution of overlapping peaks and the determination of kinetic parameters for the crystallization of multicomponent system from DTA or DSC curves: Part I. Non-isothermal kinetics," Thermochimica Acta, **288,** 123- (1996).

31. A. Marotta, A. Buri and F. Branda. "Nucleation in glass and differential thermal analysis," J. Mater. Sci., **16,** 341-4 (1981).

32. C.S. Ray, K.S. Ranasinghe and D.E. Day. "Determining crystal growth rate-type of curves in glasses by differential thermal analysis," Solid State Sciences, **3,** 727-32 (2001).

33. J. ShanelovA, J. Malek, M.D. Alcala and J.M. Criado. "Kinetics of crystal growth of germanium disulfide in Ge0.38S0.62 chalcogenide glass," J. Non Cryst. Solids, **351,** 557-67 (2005).

34. H.L. Ma, M. Matecki, X.H. Zhang and S. Rogard. "Determination of the nucleation and crystal growth rate curves of a chalcohalide glass from DSC experiments," J. Mater. Sci. Lett., **16,** 21-2 (1997).

35. E.R. Shaaban, "Non-isothermal crystallization kinetic studies on a ternary, Sb0.14As0.38Se0.48 chalcogenide semi-conducting glass," Physica B, **373,** 211-16 (2006).

36. Smallman, Raymond E., Ngan,A.H.W., *Physical metallurgy and advanced materials;* Butterworth-Heinemann, Amsterdam [u.a.], 2007.

37. C. Smith, K. Chamma, D. McClane, et al. "Investigation of Morphology Changes in the $GeSe_2$-As_2Se_3-PbSe System with Varying PbSe Content," GOMD, (2015).

38. V.V. Golubkov, O.S. Dymshits, V.I. Petrov, et al. "Small-angle X-ray scattering and low-frequency Raman scattering study of liquid phase separation and crystallization in titania-containing glasses of the ZnO-Al2O3-SiO2 System," J. Non Cryst. Solids, **351,** 711-21 (2005).

39. I.S. Patel, P.W. Schmidt and S.M. Ohlberg. "Small-angle X-ray scattering study of phase separation in glasses," J. Appl. Phys., **43,** 1636-41 (1972).

40. S. Bhattacharyya, T. Hoche, K. Hahn and P.A. van Aken. "Various transmission electron microscopic techniques to characterize phase separation - illustrated using a LaF3 containing aluminosilicate glass," J. Non Cryst. Solids, **355,** 393-6 (2009).

41. O. Dargaud, L. Cormier, N. Menguy and G. Patriarche. "Multi-scale structuration of glasses: Observations of phase separation and nanoscale heterogeneities in glasses by Z-contrast scanning electron transmission microscopy," J. Non Cryst. Solids, **358,** 1257-62 (2012).

42. S. Chenu, E. Veron, C. Genevois, et al. "Tuneable Nanostructuring of Highly Transparent Zinc Gallogermanate Glasses and Glass-Ceramics," Advanced Optical Materials, **2,** 364-72 (2014).
43. F. Abdel-Wahab, "Observation of phase separation in some Se-Te-Sn chalcogenide glasses," Physica B, **406,** 1053-9 (2011).

44. T. Ozawa, "Kinetic analysis of derivative curves in thermal analysis," **2,** 301-24 (1970).

45. N. Carlie, N.C. Anheier J., H.A. Qiao, et al. "Measurement of the refractive index dispersion of As2Se3 bulk glass and thin films prior to and after laser irradiation and annealing using prism coupling in the near- and mid-infrared spectral range," Rev. Sci. Instrum., **82,** 053103 (7 pp.) (2011).

46. H.A. Qiao, N.C. Anheier, J.D. Musgrave, K. Richardson and D.W. Hewak. "Measurement of chalcogenide glass optical dispersion using a mid-infrared prism coupler," Proceedings of the SPIE - The International Society for Optical Engineering, **8016,** 80160F (10 pp.) (2011).

47. B. Gleason, K. Richardson, L. Sisken and C. Smith. "Refractive Index and Thermo-Optic Coefficients of Ge-As-Se Chalcogenide Glasses," (2016).

48. Schott Glass, "Extremely high homogeneity for large precision optics," **2016,** (2013).

49. J.A. Augis and J.E. Bennett. "Calculation of the Avrami parameters for heterogeneous solid state reactions using a modification of the Kissinger method," J Therm Anal, **13,** 283-92 (1978).

50. Schott Glass. "Infrared Chalcogenide Glasses," **2016.**

51. K. Richardson, A. Buff, C. Smith, et al. “Engineering Novel Infrared Glass Ceramics for Advanced Optical Solutions,” Proc. SPIE Vol. **9822** paper # 9822-4, Baltimore MD (2016).